Nonreciprocal Nanophotonic Structures

Vom Promotionsausschuss der
Technischen Universität Hamburg

zur Erlangung des akademischen Grades

Doktor-Ingenieur (Dr.-Ing.)

genehmigte Dissertation

von
Dirk Jalas

aus
Brunsbüttel

2019

Erster Gutachter: Prof. Dr. Manfred Eich
Zweiter Gutachter: Prof. Dr.-Ing. Arne Jacob
Prüfungsvorsitzender: Prof. Dr.-Ing. Gerhard Bauch
Tag der mündlichen Prüfung: 15. November 2019

ABSTRACT

This work proposes new concepts for integrated nonreciprocal optical components. An isolator, a circulator, a magneto-optical switch as well as a Faraday rotator are presented.

ZUSAMMENFASSUNG

Diese Arbeit präsentiert neue Konzepte für die Integration von nichtreziproken optischen Komponenten. Es werden ein Isolator, ein Zirkulator, ein magneto-optischer Schalter sowie ein Faraday Rotator vorgestellt.

CONTENTS

Reciprocity in daily life I: Proust

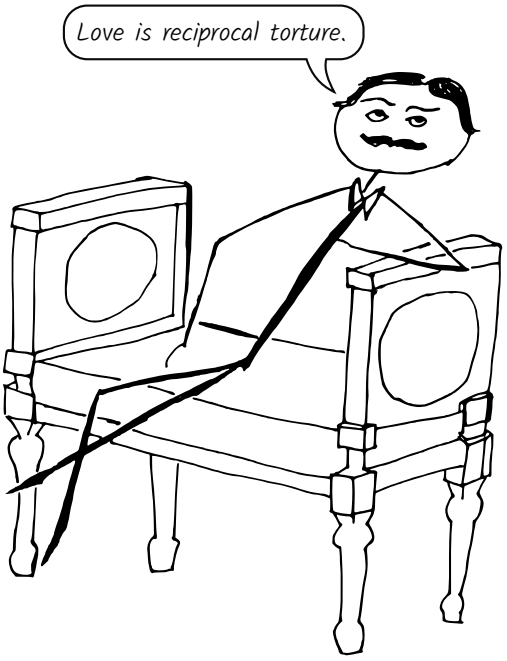

*Marcel Proust - In Search of Lost Time (1913-1927)

1 INTRODUCTION

The internet is arguably the most disruptive invention of the 20th century. It has made a lasting impression on almost all fields of business and – for better or worse – even transformed our society as a whole. The Arab spring and the growing importance of social media in democratic elections are only two examples for this [1–3]. As the internet penetrates almost all aspects of our daily life, the amount of data that is transferred grows by each day (see Fig. 1a) [4–6]. With this comes an ever increasing demand in bandwidth and a need for energy as well as cost efficiency. A key technology to keep this growth sustainable is silicon photonics [7]. The use of optical signals allows for high bandwidth and low-loss communication. The use of silicon as material system is advantageous because of its high refractive index which allows for nanometer feature sizes and its already mature low-cost production process as it is the backbone of the semiconductor industry. Fig. 1b shows the predicted growth of the silicon photonic market [8]. The bulk of this growth is expected to stem from data center applications and the remainder will be due to other applications like sensing [8]. Also for the latter the potential for low cost and small footprint are the key advantages.

Despite all the advantages of silicon, it has some shortcomings. Its low optical losses in the near infrared make it ideal to be used as a waveguide material, but make it not usable as a detector or a source. Further, it has no electro-optical effect and is thus not viable for electro-optic modulation which is needed to transform electrical signals into optical signals. These shortcomings are dealt with by introducing new materials into the silicon photonic platform like for example III-V compounds for light emission, germanium for detection and organic compounds for modulation [7]. While many examples for such solutions exist in scientific literature, one key challenge and part of ongoing research is not to spoil the cost effectiveness of the production process with the added complexity of new materials.

In this work we deal with another functionality that is lacking in the silicon photonic platform: isolation and circulation. We give an accurate definition of what these two terms mean in chapter 2; but roughly isolation can be described as a process in which light can pass a device in one direction and is blocked for the reverse direction (see section 2.3). Circulation is related to isolation though in this case the light in reverse direction is not blocked but rerouted to another place (see section 2.4). Such devices have the potential for greatly reducing the production costs [7, 9]. Small levels of backreflection into a laser will increase its linewidth and noise [10–12] and larger levels may

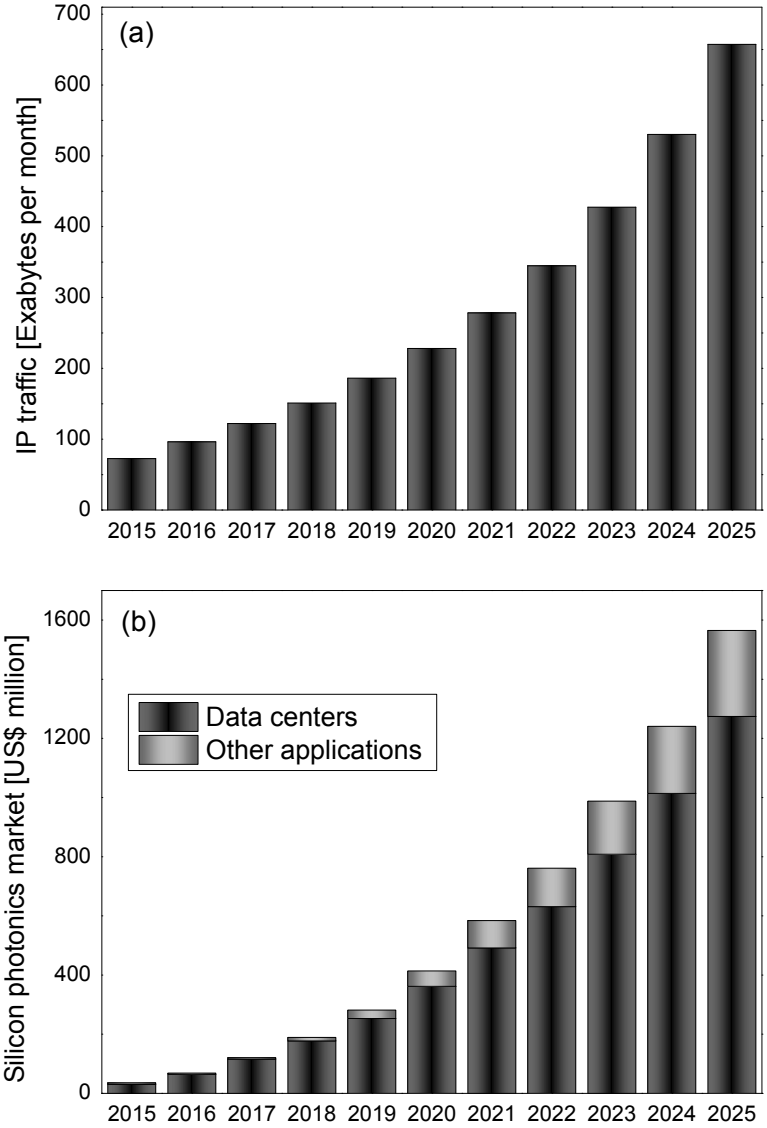

Figure 1: (a) Worldwide internet traffic per month. The data points from 2015 and 2016 are from [4] and [5]. The years 2017 to 2022 are a prediction from [6], assuming 24% annual growth. The remaining years are extrapolated from that prediction assuming the growth rate to remain the same. (b) The silicon photonic market size in the year 2015 and its predicted growth [8].

even impair its function. Great care has therefore to be taken in the system design and production. An isolator could block unwanted reflection and thus reduce the requirements on the production and design which offers the potential for cost reduction. A circulator can do the same as a isolator, with the added functionality that incoming signals can be redirected. This can be used to measure the reflections if the system serves as a sensor or to reroute an incoming signal away from the laser to a detector, such that a single waveguide can serve as the transmit and receive channel.

This thesis is organized as follows: Chapter 2 serves as an introduction to the employed physical phenomena and the utilized modeling techniques. The prerequisites for building an isolator or circulator are presented, namely the breaking of the Lorentz reciprocity relation. The content of this section was previously published in a review:

- D. Jalas, A. Petrov, M. Eich, W. Freude, S. Fan, Z. Yu, R. Baets, M. Popović, A. Melloni, J. D. Joannopoulos, M. Vanwolleghem, C. R. Doerr, and H. Renner, "What is – and what is not – an optical isolator," *Nature Photonics* **7**, pp. 579–582, 2013.

Further, the chapter focuses on magneto-optical effects which are employed in this thesis to achieve the breaking of reciprocity. In particular, nonreciprocal ring resonators are discussed. An isolator made from a magneto-optically active ring resonator was the topic of the authors Master's thesis [13] and was also subject of publication in Optics Letters:

- D. Jalas, A. Petrov, M. Krause, J. Hampe, and M. Eich, "Resonance splitting in gyrotropic ring resonators," *Optics Letters* **35**, pp. 3438–3440, 2010.

The main findings of that article are summarized as well. Finally, the chapter introduces the temporal coupled-mode theory which is the basis for the analysis done in chapter 3 and 4.

Chapter 3 discusses backscattering in ring resonators. The first part discusses how magneto-optical effects can suppress unwanted backscattering. The second part presents a device that relies on engineering the backscattering in combination with the magneto-optical effect such that it can be used as a switch. This idea was published as:

- D. Jalas, A. Petrov, and M. Eich, "Theory of gyrotropic ring resonators with counterpropagating modes coupling," *Photonics and Nanostructures – Fundamentals and Applications* **9**(4), pp. 351–357, 2011.

In chapter 4 a concept for a circulator based on a ring resonator is presented. This chapter is subject of another publication:

- D. Jalas, A. Petrov, and M. Eich, "Optical three-port circulators made with ring resonators," *Optics Letters* **39**, pp. 1425–1428, 2014.

In chapter 5 a method to measure the magneto-optical phase shift of silicon waveguides is presented. The measurement is so sensitive that it is capable to measure the quite weak magneto-optical effect of silicon. The method was presented at the Group IV conference and is part of the following proceeding:

- D. Jalas, A. Stepan, A. Petrov, and M. Eich, "Experimental demonstration of magneto-optical phase shift in silicon on insulator waveguides," *8th IEEE International Conference on Group IV Photonics*, pp. 160–162, 2011.

Furthermore, the chapter discusses the measurement method applied to silicon waveguides with various magneto-optically active cladding materials.

Finally, in chapter 6 we discuss the possibility of using the weak magneto-optical effect of silicon for a highly compact integrated optical isolator. The concept was presented as well at the Group IV conference and can be found in the following proceeding:

- D. Jalas, N. Hakemi, M. Cherchi, M. Harjanne, A. Petrov, and M. Eich, "Faraday rotation in silicon waveguides," *14th International Conference on Group IV Photonics*, pp. 141–142, 2017.

The subsequent chapters contain text and images from all the above mentioned publications without explicitly referring to these sources.

Reciprocity in daily life II: Nonreciprocal information flow

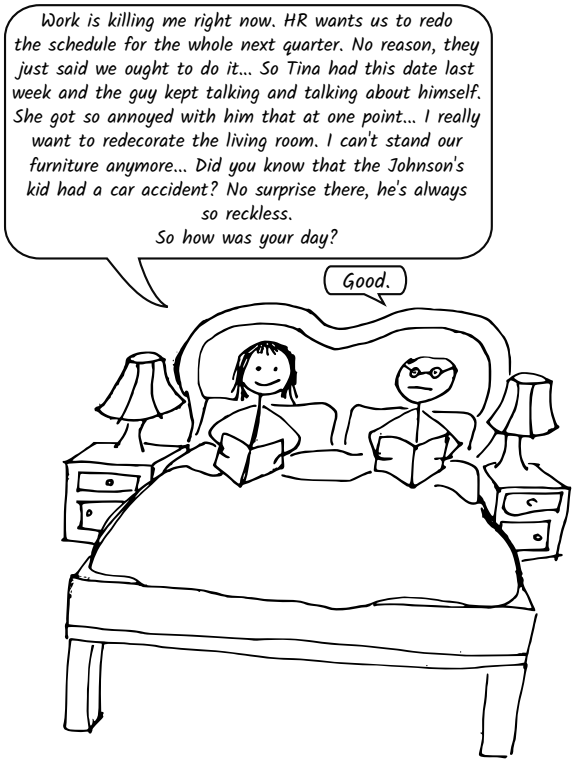

2

THE BREAKING OF RECIPROCITY AND MAGNETO-OPTICAL EFFECTS

This chapters summarizes nonreciprocal systems with a focus on magneto-optical systems. It closes with a description of temporal coupled-mode theory.

Contents

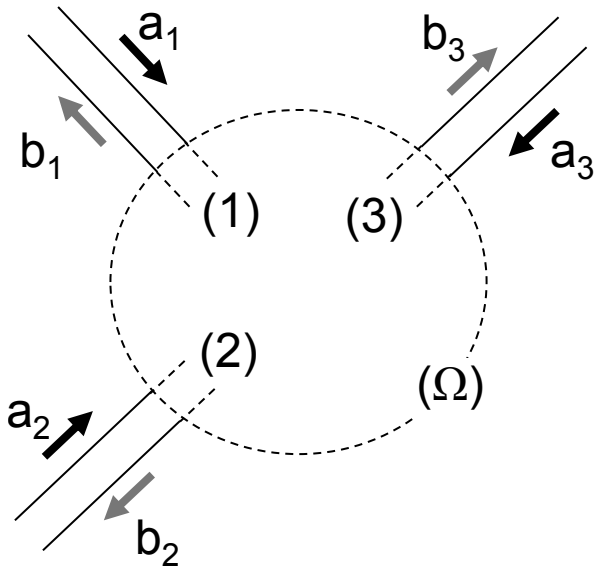

Figure 2: General optical circuit

2.1 WHAT IS – AND WHAT IS NOT – AN OPITCAL ISOLATOR?

Optical isolators are devices that block light for one direction and let light pass for the opposite direction. This is important, for example, when one wants to protect a laser from back reflections which can disturb the laser operation or to mitigate multi-path interference in an optical communication system. Moreover, the use of an isolator relaxes the requirements on the design of the optical system, avoiding spurious interferences, interactions between different devices and undesired light routing. From a system designer perspective, since the reflected light is typically generated from random structural imperfections, the modal and polarization content of the reflection is unknown. In such a case, the task of preventing the light retracing the forward path can only be performed by systems that break Lorentz reciprocity. Simply demonstrating asymmetrical power transmission is not a sufficient indicator for breaking Lorentz reciprocity. The reasons for this requirement are a bit subtle and recently there has been some confusion about the need for nonreciprocity and how to implement nonreciprocity itself. Therefore, in the following we will show why the breaking of Lorentz reciprocity is pivotal for isolators and how to prove unambiguously what is – and what is not – an optical isolator. Similar problems arise also for other types of waves like for example acoustic waves [14].

2.2 DEFINITION OF THE PORTS, MODES AND THE SCATTERING MATRIX

The first step to understand an isolator is to appropriately describe the light that goes in and out. For that we draw around our device a fictitious closed boundary surface Ω as shown in Fig. 2. The device inside Ω is assumed to be linear, time-independent and can be lossy or with gain. The only way for light to enter the inside of Ω is through the lossless reciprocal waveguides which we call ports in the following. The light travelling in these waveguides can be described by modes. Modes are the eigensolutions of Maxwell's equations for a waveguide (or free-space propagation channel) that is extended to infinity. In principle, there are modes that are guided by the waveguide as well as radiation modes. However, we can always make Ω so big that the field comprised by the latter has sufficiently decayed and we can assume the field energy is exclusively carried by guided modes when focusing our interest on the cross-sectional area in and around any of the feeder waveguides. Thus, we may consider exclusively the fields that can be guided by a waveguide. The radiative fields in the large space between the waveguides can be thought to be blocked in the inner of the surface Ω by absorbers without affecting the guided modes. These guided modes have plane wavefronts given the assumption of lossless entry waveguides. The surface Ω is chosen such that the directions of all the waveguides are normal to Ω and the waveguides and their guided modes are assumed to be essentially non-overlapping. For the guided modes there will always be one solution that propagates in forward direction into the device and another one that propagates in backward direction. The components of each guided mode tangential to Ω have the form of [15]

$$\mathbf{E}_{T,\mu}(x,y,z) = \left(a_\mu e^{-\beta_\mu z} + b_\mu e^{\beta_\mu z}\right) \mathbf{e}_{T,\mu}(x,y), \tag{1}$$

$$\mathbf{H}_{T,\mu}(x,y,z) = \left(a_\mu e^{-\beta_\mu z} + b_\mu e^{\beta_\mu z}\right) \mathbf{h}_{T,\mu}(x,y). \tag{2}$$

Here z points into the forward direction of each waveguide into the structure, a_μ is the complex amplitude of the wave travelling into the structure, b_μ is the amplitude of the wave going in the reverse direction, μ is the mode index and β_μ is the propagation constant of the mode. Two generic modes μ and ν are orthogonal to each other and normalized such that

$$\frac{1}{2}\iint_{(\Omega)} \mathbf{e}_\mu \times \mathbf{h}_\nu^* d\mathbf{s} = \delta_{\mu\nu} \tag{3}$$

where $\delta_{\mu\nu}$ is the Kronecker delta. It follows that if we have a wave that is guided in the waveguide, its fields can be split into modes as in equations 1 and 2. The tangential fields on the surface of Ω (assuming z = 0 for each feeder waveguide) can be written as

$$\mathbf{E}_{T,\mu} = \sum_{\mu} \left(a_\mu + b_\mu\right) \mathbf{e}_{T,\mu}, \tag{4}$$

$$\mathbf{H}_{T,\mu} = \sum_{\mu} \left(a_\mu + b_\mu\right) \mathbf{h}_{T,\mu}, \tag{5}$$

To summarize, we can describe the light that enters and leaves the device through the waveguides by the amplitudes of the eigensolutions of Maxwell's equations for these waveguides. This is quite convenient if one wants to calculate the power entering or leaving the device. From equations 1, 2 and 3, we find the total power balance at the surface Ω as

$$P = \sum_{\mu} \left(|a_\mu|^2 + |b_\mu|^2\right) = \mathbf{A}^{*T}\mathbf{A} - \mathbf{B}^{*T}\mathbf{B}. \tag{6}$$

Here, $\mathbf{A}$ and $\mathbf{B}$ are column vectors containing the a_μ and b_μ as elements. Since we assumed that the system is linear and time-independent, the outgoing waves are completely determined by the incoming waves and by the device properties. This means there is a linear relation between $\mathbf{A}$ and $\mathbf{B}$ which can be written in matrix form as

$$\mathbf{B} = \mathbf{S}\mathbf{A}. \tag{7}$$

The matrix $\mathbf{S}$ is called the scattering matrix. On-diagonal elements of $\mathbf{S}$ are the reflection coefficients back into the respective mode, off-diagonal components are transmission coefficients from one mode to another. The scattering matrix is a very handy tool for describing photonic circuits, and for an isolator it must have certain characteristics that we discuss in the next paragraph.

2.3 DEFINITION OF AN ISOLATOR

As already mentioned, an isolator protects a device from back reflections. This means that isolation poses a particular requirement on the scattering matrix elements connecting its two ports. There needs to be a pair of two modes – one belonging to each port – such that the transmission from mode μ in port 1 to mode ν in port 2 is essentially non-zero while the transmission from mode ν in port 2 to mode μ in port 1 is close to zero. It is not important where the energy for the latter case goes. It can be dissipated in the device or can be transmitted to a third port or radiated away. The corresponding scattering matrix for a two-port isolator is shown in Fig. 3. In the general case, where at least at one port a plurality of modes is present, in order to achieve isolation the asymmetrical transmission properties discussed above must hold between each of the port modes. From this definition, we can derive a property of the scattering matrix of an isolator: The scattering matrix must be asymmetric, because the

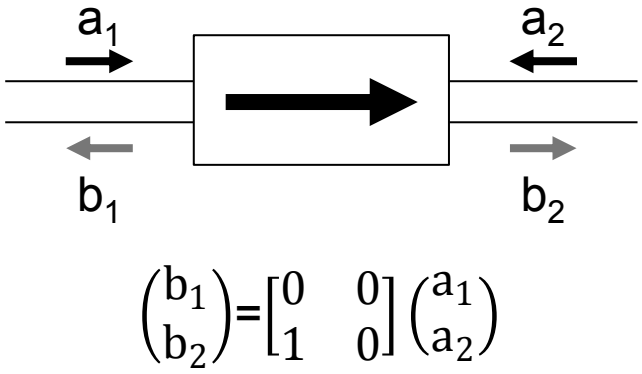

Figure 3: The simplest isolator with two single-mode waveguide ports. The scattering matrix indicates that the isolator allows transmission in only one direction.

mode-to-mode transmission is different for opposite propagation directions. Although this may be trivial, it is worth stressing that an isolator has to block or divert all the modes that can be excited for the backward transmission. It is not sufficient to find an ensemble of modes that has a good transmission in forward direction and another ensemble of modes that has bad transmission in backward direction. Backward transmission for all ensembles needs to be blocked. Only in this case, the device can be called an isolator. This arises from the basic system argument that a parasitic reflection may excite an arbitrary ensemble of modes in practical systems. In particular, a very common class of systems is a standard single-mode fibre that can sustain two orthogonal guided polarization modes. A parasitic reflection may excite an arbitrary amount of power in either polarization. Hence an isolator would need to block/divert both polarizations irrespective of the amplitude and phase relationship between them.

2.4 DEFINTION OF A CIRCULATOR

Related to the isolator is the circulator. It is a device with three or more ports. The port mapping of such a device is shown in Fig. 4. For two adjacent ports the circulator functions as an isolator in the sense that it lets light pass in one direction and blocks it for the reverse. In contrast to an isolator, which can scatter or absorb the blocked light, the circulator redirects it to another port. This is for example important if one wants to seperate an outgoing signal from an incoming one. The requirements on the scattering matrix are the same as for the isolator discussed in the previous section.

2.5 INTRODUCTION TO LORENTZ RECIPROCITY THEOREM

Consider two states of excitation with mode amplitude column vectors $\mathbf{A}'$, $\mathbf{B}'$ and $\mathbf{A}''$, $\mathbf{B}''$, as well as the corresponding fields $\mathbf{E}'(x, y, z)$,

An example for two possible excitation states, $\mathbf{A}'$, $\mathbf{B}'$ and $\mathbf{A}''$, $\mathbf{B}''$, is given in Fig. 5.

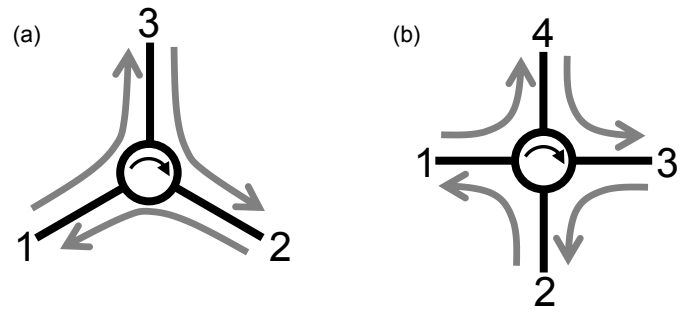

Figure 4: Principal layout for a three-port circulator (a) and a four-port circulator (b). Both devices allow transmission to only one of the two adjacent ports and allow reception from the port that is blocked in transmission.

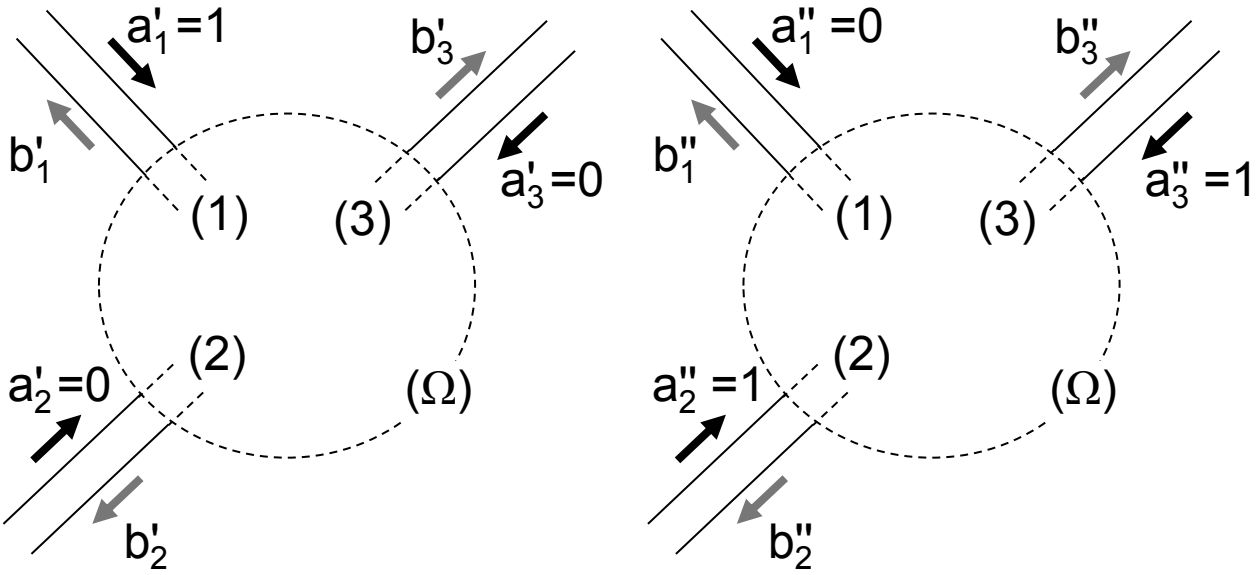

Figure 5: Examples for different states of excitation that can be related by Lorentz reciprocity. On the left side the device is excited with $\mathbf{A}' = [\ 1 \quad 0 \quad 0\ ]^t$ and on the right side it is excited with $\mathbf{A}'' = [\ 0 \quad 1 \quad 1\ ]^t$. $\mathbf{B}'$ and $\mathbf{B}''$ are obtained through equation 7. All other possible input states can be related by Lorentz reciprocity as well, given the device is reciprocal.

$\mathbf{H}'(x,y,z)$, $\mathbf{E}''(x,y,z)$, and $\mathbf{H}''(x,y,z)$ [16]. The time-harmonic sourceless Maxwell's equations for the first excitation are

$$\nabla \times \mathbf{E}' = -j\omega\boldsymbol{\mu}\mathbf{H}', \tag{8}$$

$$\nabla \times \mathbf{H}' = j\omega\boldsymbol{\varepsilon}\mathbf{E}'. \tag{9}$$

Dot multiplying equation 8 with $\mathbf{H}''$ and the equation 9 with $\mathbf{E}''$ and and then summing up gives

The scalar product is here defined as $\mathbf{A}\cdot\mathbf{B} = \sum_i a_i b_i$ and not $\mathbf{A}\cdot\mathbf{B} = \sum_i a_i b_i^\dagger$ like often done for complex vectors.

$$\mathbf{H}''\nabla \times \mathbf{E}' + \mathbf{E}''\nabla \times \mathbf{H}' = j\omega(\mathbf{E}''\boldsymbol{\varepsilon}\mathbf{E}' - \mathbf{H}''\boldsymbol{\mu}\mathbf{H}'). \tag{10}$$

Applying the same process with interchanged primes yields

$$\mathbf{H}'\nabla \times \mathbf{E}'' + \mathbf{E}'\nabla \times \mathbf{H}'' = j\omega(\mathbf{E}'\boldsymbol{\varepsilon}\mathbf{E}'' - \mathbf{H}'\boldsymbol{\mu}\mathbf{H}''). \tag{11}$$

Subtracting these two equations we obtain

$$\nabla \cdot (\mathbf{E}' \times \mathbf{H}'' - \mathbf{E}'' \times \mathbf{H}') = j\omega(\mathbf{E}''\boldsymbol{\varepsilon}\mathbf{E}' - \mathbf{E}'\boldsymbol{\varepsilon}\mathbf{E}'' - \mathbf{H}''\boldsymbol{\mu}\mathbf{H}' + \mathbf{H}'\boldsymbol{\mu}\mathbf{H}''). \tag{12}$$

If $\boldsymbol{\varepsilon}$ and $\boldsymbol{\mu}$ are scalars or symmetric tensors, the right-hand side of the above equation adds up to zero and formulates the Lorentz reciprocity theorem

$$\nabla \cdot (\mathbf{E}' \times \mathbf{H}'' - \mathbf{E}'' \times \mathbf{H}') = 0. \tag{13}$$

Equation 13 also holds for materials with gain or loss as long as $\boldsymbol{\varepsilon}$ and $\boldsymbol{\mu}$ are symmetric. Let us discuss some cases where the Lorentz reciprocity does not hold. One example is a magneto-optical material. Here, the permittivity is an asymmetric tensor and the order in which $\mathbf{E}'$, $\mathbf{E}''$ and $\boldsymbol{\varepsilon}$ are multiplied becomes important. In this case, the right-hand side of equation 12 is in general non-zero. Reciprocity is also broken in nonlinear materials. $\boldsymbol{\varepsilon}$ is a function of the E-field and the right-hand side of equation 12 becomes $\mathbf{E}''\boldsymbol{\varepsilon}(\mathbf{E}')\mathbf{E}' - \mathbf{E}'\boldsymbol{\varepsilon}(\mathbf{E}'')\mathbf{E}''$. This is non-zero for arbitrary $\mathbf{E}'$ and $\mathbf{E}''$. Another class of systems for which the reciprocity does not hold is a structure where $\boldsymbol{\varepsilon}$ and $\boldsymbol{\mu}$ depend on time. In such a case the above presented derivation is not applicable as it assumes time-harmonic fields and time-independent materials.

2.6 CONSEQUENCES OF THE LORENTZ RECIPROCITY THEOREM FOR TRANSMISSION COEFFICIENTS BETWEEN PORTS

If the Lorentz theorem holds for the device under investigation, isolation cannot be realized. Whatever the combination of materials and devices, if they are linear, time-independent and reciprocal, the scattering matrix is symmetric and not suitable for isolation. This is proven in the following [15]: as in the previous paragraph we consider two states of excitation $\mathbf{A}'$, $\mathbf{B}'$ and $\mathbf{A}''$, $\mathbf{B}''$ belonging to the fields $\mathbf{E}'$, $\mathbf{H}'$, $\mathbf{E}''$ and $\mathbf{H}''$. The fields are related by the Lorentz reciprocity

theorem. If we integrate equation 13 over the volume enclosed by surface Ω and insert the modal field expansion from equation 4 and 5, we obtain

$$2\sum_{\mu}\sum_{\nu}(b'_{\nu}a''_{\mu} - a'_{\mu}b''_{\nu}) \iint_{(\mathbf{\Omega})} \mathbf{e}_{\mu} \times \mathbf{h}^{*}_{\nu} \mathrm{d}\mathbf{s} = 0. \tag{14}$$

We assumed previously in our definition of waveguide ports that all the waveguides leading into the device are lossless. From this it follows that the transverse modal fields can be chosen to be purely real functions [15]. The integral in equation 14 can then be identified with the orthogonality condition of equation 3 and the expression can be simplified to

$$\begin{aligned}\sum_{\mu}(b'_{\mu}a''_{\mu} - a'_{\mu}b''_{\mu}) = \mathbf{B'}^{T}\mathbf{A''} - \mathbf{A'}^{T}\mathbf{B''} = \mathbf{A'}^{T}\mathbf{S}^{T}\mathbf{A''} - \mathbf{A'}^{T}\mathbf{S}\mathbf{A''} \\ = \mathbf{A'}^{T}(\mathbf{S}^{T} - \mathbf{S})\mathbf{A''} = 0.\end{aligned} \tag{15}$$

As $\mathbf{A}'$ and $\mathbf{A}''$ can be chosen arbitrarily it follows that

$$\mathbf{S}^{T} = \mathbf{S}. \tag{16}$$

Therefore, for a Lorentz-reciprocal device the scattering matrix must be symmetric, thus it has no isolation property.

2.7 EXAMPLES OF RECIPROCAL AND NONRECIPROCAL STRUCTURES

At first glance, spatial symmetry breaking and nonreciprocity can yield similar effects of which only the latter can be used for isolation. Fig. 6 shows an example for each case. In Fig. 6a–c an inclined junction between a silica and a silicon slab waveguide is presented similar to the example for phonon waves in the paper by Maznev et al. [14]. The refractive indices are $n_{Si} = 3.5$, $n_{SiO2} = 1.45$ and $n_{Air} = 1$. The interface angle is chosen in such a way that an excitation with the fundamental TM mode from the right (Fig. 6c) is totally internally reflected at the interface and there is little transmission to the left. For the excitation from the left side (Fig. 6b) the light is diffracted into the higher order modes of the silicon waveguide and there is strong transmission to the right. Although this device can transmit the fundamental mode of the silica waveguide from the left and block the fundamental mode of the silicon waveguide from the right it is not an isolator. If we take the higher order modes excited in case b and send them back with identical phase and amplitude relations between the modes, the transmission into the first order mode of the silica waveguide will be 1.

Fig. 6d–f shows a silicon single-mode slab waveguide with an SiO2 substrate and a magneto-optical cladding. If the cladding is magnetized, as shown in Fig. 6d, its permittivity becomes an asymmetric

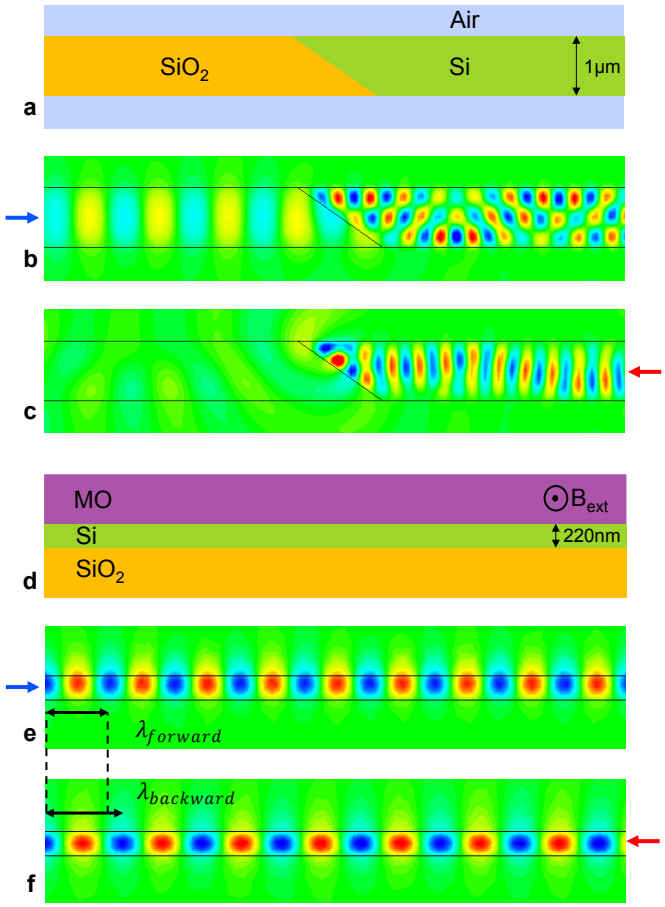

Figure 6: **a**, Junction in a silica and silicon slab waveguide: **b**, excitation with the fundamental TM mode from the left; **c**, excitation with the fundamental TM mode from the right. **d**, Silicon slab waveguide with a silica substrate and magneto-optical cladding; **e**, excitation with the fundamental TM mode from the left; **f**, excitation with the fundamental TM mode from the right. All field plots show the out-of-plane component of the H-field, and light with a free-space wavelength of 1.55 µm was used. We performed simulations with CST Microwave Studio to demonstrate reciprocal and nonreciprocal effects. The undulation of the field in **c** is caused by a simultaneous excitation of the first and second order mode upon reflection. The two modes have different propagation constants and thus the pattern changes along the waveguide.

tensor. We set the main-diagonal components to $\varepsilon_{xx/yy} = 4.84$ and the off-diagonal component to $\varepsilon_{yx/xy} = \pm i \cdot 2.5$. The off-diagonal component is chosen unrealistically high for illustrative purposes. The asymmetric nature of the permittivity tensor leads to a different effective wavelength for the forward (Fig. 6e) and backward (Fig. 6f) propagating wave. Thus, if we send the transmitted wave of the case 6e back, it will accumulate a different phase in the waveguide. This difference can be used to build an isolator with the help of a Mach-Zehnder interferometer [17]. The origin of this difference in phase accumulation is discussed in section 2.12.2.

2.8 DEVICES THAT ARE ISOLATORS

Now that we know that for an isolator we need an asymmetric scattering matrix, which breaks the Lorentz reciprocity theorem, we will give some examples how to achieve this. We will not discuss in detail how these isolators work but only briefly explain the underlying physical effects. A more detailed discussion can be found in the given references. Probably the most common optical isolator relies on the Faraday effect and 45°-crossed polarizers [18]. Here, a magneto-optically active material gives rise to polarization rotation which has opposite signs for backward and forward propagation. Other concepts relying on magneto-optical materials are waveguides with different propagation constants for forward and backward direction [17, 19–22]. Similarly, a nonreciprocal propagation loss can be utilized [23]. Magneto-optical materials can also induce frequency splitting in resonators [24–27]. There are also magneto-optical waveguides where the back-propagating mode is suppressed [28–32]. Another class of materials that breaks reciprocity and therefore can be used for isolators is that of nonlinear materials. Examples are isolators using Raman amplification [33], stimulated Brillouin scattering [34] or chirped nonlinear optical photonic crystals based on the Kerr effect [35, 36]. The first two concepts [33, 34] behave linearly for the signal as long as the signal power stays well below the pump level. The last two concepts [35, 36] work only for a certain signal power range and simultaneously propagating forward and backward waves can influence each other. Fan and coworkers even showed that for Kerr effect-based devices with strong optical pump that introduces the nonlinearity, the much weaker signal will essentially see a reciprocal system [37]. The last class of devices we would like to mention are isolators with time- and spatially-dependent refractive index distribution [38, 39]. Here, a propagating index perturbation is used to couple two specific forward-propagating modes but not any pair of backward-propagating modes. This travelling perturbation can be created by electro-optical effects [40] or by sound waves [41].

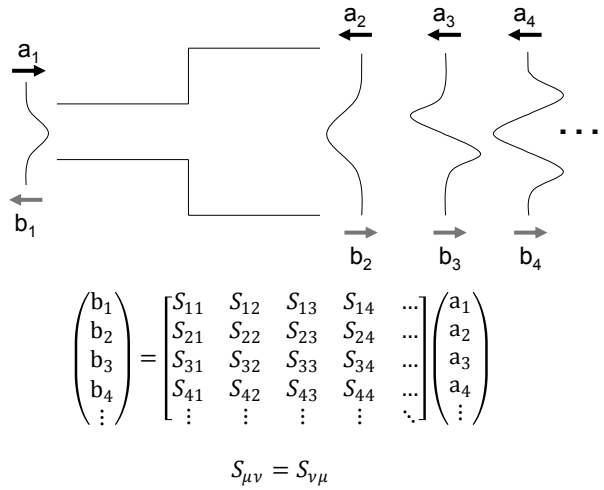

Figure 7: A junction between single-mode and multi-mode waveguides and the corresponding scattering matrix.

2.9 DEVICES THAT ARE NOT ISOLATORS

Some devices appear to be an isolator if one does not carefully distinguish between power flow and modal transmission properties. An example for this is the junction between a single-mode fibre and a multi-mode fiber. The scattering matrix with corresponding mode envelopes is shown in Fig. 7. When excited from the single-mode side, the power is distributed in all the different modes on the multi-mode side and over all there is almost 100% power transmission. If the structure is excited from the multi-mode side with a particular mode the transmission will be very small. This becomes clear if one looks at the scattering matrix in Fig. 7 – the power for the first case calculates as $P_{fw} = |b_2|^2 + |b_3|^2 + |b_4|^2 + \cdots = (|S_{21}|^2 + |S_{31}|^2 + |S_{41}|^2 + \cdots)|a_1|^2$. For the second case with an excitation with mode 2, the transmitted power is $P_{bw} = |b_1|^2 = |S_{12}|^2|a_2|^2$. As $S_{12} = S_{21}$, P_{bw} is clearly smaller than P_{fw} if the modal amplitudes a_1 and a_2 are the same. Still this device is not an isolator: There is a combination of modes in the second waveguide with close to 100% transmission into the first mode. The same argument can be made for the waveguide junction in Fig. 6a-c. There are more examples which caused similar confusions [42–45], some of them we commented on in refs. [46] and [47]. Other structures that cause confusion are complex diffraction gratings [48–51]. The formalism derived here for waveguides can be applied to plane waves as well. The modes into which light can be scattered by the grating are plane waves in different diffraction orders. To avoid confusion with nonreciprocity, diffraction orders should be defined and transmission between diffraction orders should be calculated. Structures based on linear materials with symmetric permittivity tensor are always reciprocal. It should be noted that the terms “unidirectionality” and “one-way diffraction” are used

ambiguously in some publications on gratings. Some authors use it to imply that the total transmission for a normal excitation with a plane wave from one side is different from the total transmission for a normal excitation from the opposite side. This is again not sufficient for nonreciprocity and one cannot build an isolator from such a structure in the sense of equation 13. None of the above-mentioned devices would be useful in protecting a laser from reflections. Backward energy from the system can find its way into the laser. Only a true isolator can prevent any backward energy from entering the laser.

2.10 MAGNETO-OPTICAL EFFECTS

This work utilizes magneto-optical materials to break reciprocity. In the following, magneto-optical phenomena and their effect on optical systems are therefore discussed in detail.

2.10.1 *Zeeman effect*

If a material that consists of an ensemble of isotropic, harmonic oscillators is magnetized, its resonant absorption will split in frequency. To illustrate this in a classical approach, we examine the forces on an electron in a harmonic potential in the presence of a static magnetic field $\mathbf{B}$ and an optical field $\mathbf{E}e^{j\omega t}$ [52]:

We neglect the force exerted by the optical magnetic field, $-e\mathbf{v} \times \mathbf{B}_{opt}$. For a plane wave this term is equal to $-e\frac{\mathbf{v}}{c} \times \mathbf{E}_{opt}$. Except for relativistic speeds or very high electric field strengths this term is much smaller than the electric field force and the static magnetic field force [53, 54].

$$\mathbf{F} = -e\left(\mathbf{E}e^{j\omega t} + \mathbf{v} \times \mathbf{B}\right) - m\omega_0^2\mathbf{r} - m\gamma\mathbf{v}, \tag{17}$$

where $\mathbf{F}$ is the total force on the particle, e is the elementary charge, $\mathbf{r} = x(t)\,\mathbf{e}_x + y(t)\,\mathbf{e}_y + z(t)\,\mathbf{e}_z$ is the displacement of the electron, $\mathbf{v} = \dot{\mathbf{r}}$, and $m\omega_0^2$ is the spring constant of the resonator with m being the electron's mass and ω_0 being the resonance frequency, γ is a friction coefficient modelling the finite decay time of the resonator. If we assume the magnetic field to be $\mathbf{B} = B\mathbf{e}_z$, the equations of motion for the electron become:

$$m\ddot{x} + m\gamma\dot{x} + m\omega_0^2 x = -eE_x e^{j\omega t} - eB\dot{y}, \tag{18}$$

$$m\ddot{y} + m\gamma\dot{y} + m\omega_0^2 y = -eE_y e^{j\omega t} + eB\dot{x} \tag{19}$$

and

$$m\ddot{z} + m\gamma\dot{z} + m\omega_0^2 z = -eE_z e^{j\omega t}. \tag{20}$$

For the motion in z-direction, the magnetic field and velocity are aligned and the magnetic force is zero. Thus, equation 20 is that of the standard Lorentz oscillator [55] and will not be discussed further here.

The polarization of the total ensemble of harmonic oscillators is related to the displacement of a single element by $\mathbf{P} = -eN\mathbf{r}$, where N

is the oscillator density. If we insert the polarization into equations 18 and 19 and assume harmonic time-dependence, $\mathbf{P}(t) = \left(P_x\mathbf{e}_x + P_y\mathbf{e}_y + P_z\mathbf{e}_z\right) e^{j\omega t}$, it yields the following equation system:

$$\frac{Ne^2}{m}\begin{pmatrix} E_x \\ E_y \end{pmatrix} = \begin{pmatrix} \omega_0^2 - \omega^2 + j\omega\gamma & +j\omega\frac{eB}{m} \\ -j\omega\frac{eB}{m} & \omega_0^2 - \omega^2 + j\omega\gamma \end{pmatrix}\begin{pmatrix} P_x \\ P_y \end{pmatrix}. \quad (21)$$

Equation 21 is a coupled equation system. One can find P_x and P_y by inverting the matrix or by finding a vector basis that diagonalizes the matrix. In this case the basis that diagonalizes the matrix is that of circularly polarized waves, $\mathbf{e}_{RHC} = \frac{1}{\sqrt{2}}\left(\mathbf{e}_x + j\mathbf{e}_y\right)$ for a right-hand polarized wave travelling in positive z-direction and $\mathbf{e}_{LHC} = \frac{1}{\sqrt{2}}\left(\mathbf{e}_x - j\mathbf{e}_y\right)$ for a left-handed polarized wave. Writing equation 21 in the circular polarization basis yields:

$$\begin{aligned} &\frac{Ne^2}{m}\begin{pmatrix} E_{\mathrm{RHC}} \\ E_{\mathrm{LHC}} \end{pmatrix} \\ &= \begin{pmatrix} \omega_0^2 - \omega^2 + j\omega\gamma - \omega\frac{eB}{m} & 0 \\ 0 & \omega_0^2 - \omega^2 + j\omega\gamma + \omega\frac{eB}{m} \end{pmatrix}\begin{pmatrix} P_{\mathrm{RHC}} \\ P_{\mathrm{LHC}} \end{pmatrix}. \end{aligned} \quad (22)$$

With the definition of the relative permittivity ε_r as $\varepsilon_0\mathbf{E} + \mathbf{P} = \varepsilon_0\varepsilon_r\mathbf{E}$ one can derive the relative permittivity of a magnetized harmonic oscillator ensemble from equation 22:

$$\varepsilon_{r,RHC} = 1 + \frac{Ne^2}{\varepsilon_0 m}\frac{1}{\left(\omega_0^2 - \omega^2\right) + j\omega\gamma - \omega\frac{eB}{m}}, \quad (23)$$

$$\varepsilon_{r,LHC} = 1 + \frac{Ne^2}{\varepsilon_0 m}\frac{1}{\left(\omega_0^2 - \omega^2\right) + j\omega\gamma + \omega\frac{eB}{m}}. \quad (24)$$

For a vanishing static magnetic field the equations 23 and 24 are those of the standard Lorentz oscillator [54]. For the case that $\left(\frac{eB}{2m}\right)^2 \ll \omega_0^2$, the static magnetic field shifts the resonance by $-\frac{eB}{2m}$ for the right-handed circularly polarized case and by $+\frac{eB}{2m}$ for the left-handed circularly polarized case as illustrated in Fig. 8. This splitting of the dielectric resonance is referred to as Zeeman effect. The permittivity for a linear polarized basis can either be obtained by inverting the matrix in equation 21 or by transforming equations 23 and 24 back to this basis. For the assumption that $\left(\omega\frac{eB}{m}\right)^2 \ll |\omega_0^2 - \omega^2 + j\omega\gamma|^2$, which is fulfilled far away from the resonance ω_0, both methods yield

$$\begin{aligned} \varepsilon_r &= \begin{pmatrix} 1 + \frac{Ne^2}{\varepsilon_0 m}\frac{1}{\left(\omega_0^2-\omega^2\right)+j\omega\gamma} & \frac{Ne^2}{\varepsilon_0 m}\frac{-j\omega\frac{eB}{m}}{\left(\left(\omega_0^2-\omega^2\right)+j\omega\gamma\right)^2} \\ \frac{Ne^2}{\varepsilon_0 m}\frac{+j\omega\frac{eB}{m}}{\left(\left(\omega_0^2-\omega^2\right)+j\omega\gamma\right)^2} & 1 + \frac{Ne^2}{\varepsilon_0 m}\frac{1}{\left(\omega_0^2-\omega^2\right)+j\omega\gamma} \end{pmatrix} \\ &= \begin{pmatrix} \varepsilon_{xx} & -jg \\ jg & \varepsilon_{yy} \end{pmatrix}. \end{aligned} \quad (25)$$

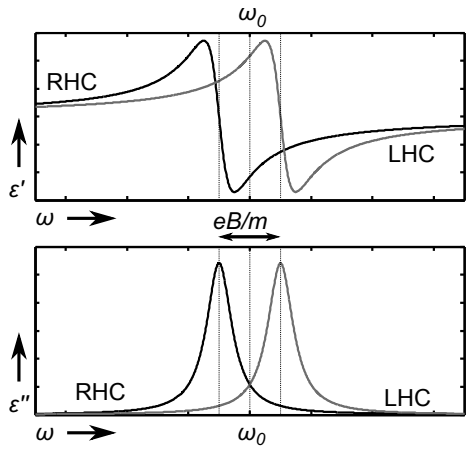

Figure 8: Real part and imaginary part of the permittivity over radial frequency. The permittivity is defined as $\varepsilon_r = \varepsilon' - j\varepsilon''$. Through the Zeeman effect the permittivity for a right-handed circularly polarized wave is shifted by $-\frac{eB}{2m}$ from the resonance frequency ω_0. A left-handed circularly polarized wave will experience a shift by $+\frac{eB}{2m}$.

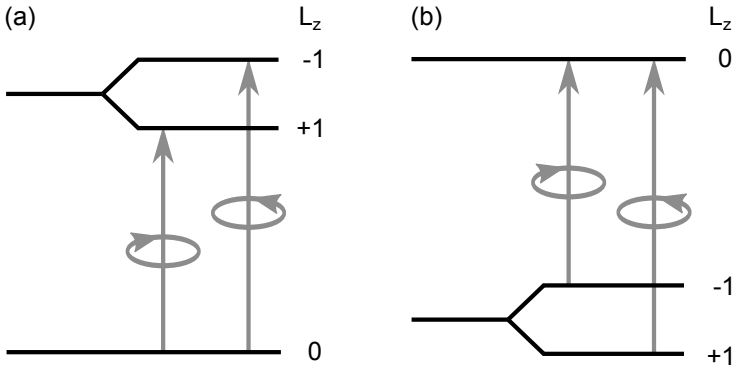

Figure 9: Possible transitions for the Zeeman splitting. (a) The degeneracy of the excited state is lifted (diamagnetic type). (b) That of the ground state is lifted (paramagnetic type).

The aforementioned assumption holds true for most practical cases because near to the resonance the imaginary part and with that the losses are too high for optical devices. For the general case all dielectric tensor elements would be affected by the static magnetic field, but for the simplified case of equation 25 the main diagonal elements are identical to the case with zero magnetic field. Only the off-diagonal elements are affected by the magnetic bias. Unlike for the circularly polarized basis, the tensor in the Cartesian basis is fully set which means that an electric field polarized in x-direction will cause an electric displacement field in y-direction and vice versa.

For a quantum mechanical description of the Zeeman splitting the picture has to be slightly altered. The oscillator, in other words the atom, features now discrete electronic energy levels and a photon can be absorbed by lifting one electron to a higher energy level. For that to happen the energy difference between the excited state and the

ground state has to match the photon energy and the atom has to absorb the photon's angular momentum. In the previously discussed case of a photon travelling in z-direction, this means that the difference in angular momentum around the z-axis has to be $\Delta L_z = \pm 1$, as a photon carries a spin of ± 1. This would be for example the case for a transition between a singlet state with $L_z = 0$ and a triplet state with $L_z = \pm 1$. For a spherically symmetric potential the triplet states are degenerate, but a biasing magnetic field lifts this degeneracy and splits the energy levels as shown in Fig. 9. A splitting of the excited level is referred to as diamagnetic splitting, whereas the splitting of the ground state is referred to as paramagnetic [56]. The diamagnetic splitting in Fig. 9a is analogous to the previously discussed classical Zeeman splitting. The magnetic field splits the resonance for photons with spin ± 1, i.e. right-handed and left-handed polarized photons, which in turn creates different permittivities for the two handednesses of circularly polarized light. Although looking very, similar the paramagnetic case in Fig. 9b is a bit more difficult. The electrons in the two split ground states are Fermi distributed and thus the lower state may feature a higher population. Because the absorption strength of a transition depends on the population of the ground state, the absorption of the lower level will be stronger than that of the higher level. As the Fermi distribution is temperature-dependent, so will also be the magneto-optical properties.

These naming conventions are somewhat unfortunate, because they are not synonymous with diamagnetic and paramagnetic magnetic material properties. The naming convention originates from the fact that materials with diamagnetic magnetism often show diamagnetic type magneto-optical effects.

2.10.2 *Faraday rotation*

Dielectric properties as shown in Fig. 8 have the consequence that the two possible handednesses of circularly polarized light will have different wavelengths in the material and will be differently damped. For low losses ($\varepsilon' \gg \varepsilon''$) the wavelength is $\lambda_0/\sqrt{\varepsilon'}$, where λ_0 is the wavelength and the damping of the intensity will be proportional to $e^{-\alpha z}$, where $\alpha = \frac{2\pi}{\lambda_0}\frac{\varepsilon''}{\sqrt{\varepsilon'}}$. This has also an important implication for linearly polarized light, which is illustrated in Fig. 10. A linearly polarized wave can be described as the superposition of a right-handed and a left-handed circularly polarized wave with equal amplitudes. The opposite senses of rotation of both partial waves cancel each other yielding a linear oscillation of the electric field. The axis of this oscillation depends on the relative phase between both waves. Through the Zeeman splitting the optical wavelength and with that the phase propagation constantly differ, which lets the axis of oscillation rotate as the linear polarized wave travels through the medium. This effect is referred to as Faraday rotation. If the phase propagation constant of the two circularly polarized waves is $k_{\mathrm{RHC/LHC}} = k_0 \pm \Delta k/2$, k_0 being the propagation constant of the unmagnetized medium, then the Faraday rotation per unit length amounts to $FR = \Delta k = k_0\left(\sqrt{\varepsilon'_{\mathrm{RHC}}} - \sqrt{\varepsilon'_{\mathrm{LHC}}}\right)$. The Faraday rotation per length and per

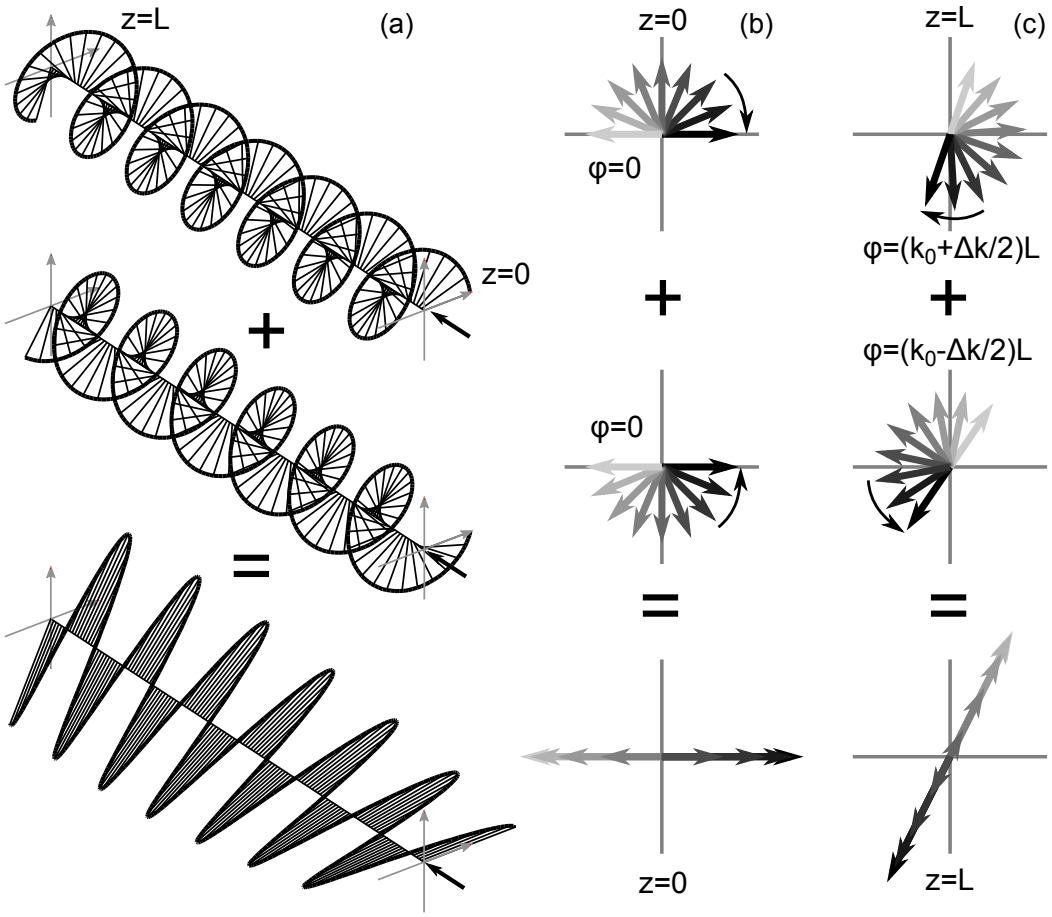

Figure 10: (a) Snapshot of a right-handed circularly polarized plane wave (top), a left-handed circularly polarized plane wave (middle) and the sum of both (bottom). The wavelength of the right-handed circularly polarized wave is by a factor 0.95 smaller than that of the left-handed circularly polarized wave. (b) Evolution of the electric field vector over time at $z = 0$. The instant drawn in (a) is black. The previous instants are drawn in increasingly brighter shades of grey. The opposite sense of rotation of the two partial wave cancels each other and yields a linearly polarized wave. (c) Same as in (b) at $z = L$. The only difference is that the relative phase of the partial waves has changed which changes the axis of the electric field oscillation for the sum.

applied magnetic field B is referred to as the Verdet constant. It is related to the off-diagonal component g in equation 25 by

$$V = \frac{180° g}{\lambda n B}, \tag{26}$$

where n is the refractive index and λ the wavelength.

2.10.3 *Faraday rotation vs optical activity*

Another important effect that leads to different refractive indices for right- and left-hand polarized light and with that to the rotation of linearly polarized light is optical activity. Although, this effect seems very alike to Faraday rotation, it has one important distinction. It is a reciprocal effect. To illustrate the difference of both effects we begin with slightly rewriting [18] the dielectric tensor for magneto-optical activity from equation 25:

$$\mathbf{D}_{\mathrm{MO}} = (\varepsilon + j\varepsilon_0 \gamma \mathbf{B}_{\mathrm{ext}} \times)\, \mathbf{E}. \tag{27}$$

The tensor is now split into its main diagonal parts ε and its off-diagonal parts $j\varepsilon_0\gamma\mathbf{B}_{\mathrm{ext}}\times$, with $\gamma = g/B$ and $\mathbf{B}_{\mathrm{ext}} = (0, 0, B)$ as in the previously discussed case but in general $\mathbf{B}_{\mathrm{ext}}$ can have any direction. Optically active media like some liquid crystals or sugars posses a chiral structure which produces coupled dipole oscillations or chiral electron movements, through which the optical magnetic field is coupled to the optical electric field and vice versa. This coupling causes the rotation of polarization. In this case the dielectric tensor takes the form of [57, 58]:

This coupling between E- and H-field is not to be confused with the relativistic coupling in equ. 17.

$$\mathbf{D}_{\mathrm{OA}} = \varepsilon \mathbf{E} - j\omega\xi \mathbf{H}, \tag{28}$$

and to account for the coupling of the electric field to the magnetic field, the permeability tensor takes the form:

$$\mathbf{B}_{\mathrm{OA}} = \mu \mathbf{H} + j\omega\xi \mathbf{E}, \tag{29}$$

where ξ is a constant determining the strength of the coupling between electric and magnetic field. Including some well-known textbooks [18, 59, 60], the coupling from the electric field to the magnetic field in equation 29 is often omitted. While such a tensor still causes a rotation of polarization, it is nonreciprocal and therefore does not describe the phenomenon of optical activity physically correctly.

If we now compare both effects, we see that in case of a magneto-optically active material, two orthogonal electric field components are coupled by an external magnetic biasing field, whereas in case of an optically active medium the electric and magnetic field strength are coupled. This is the reason why the former is a nonreciprocal effect and the latter a reciprocal effect. A linearly polarized wave will in a

magneto-optically active medium rotate its axis of polarization as described in the previous section. If this wave is reversed the magnetic biasing field still points in the same direction and thus the axis of polarization will be further rotated in the same direction. A linearly polarized wave in an optically active medium will also change its axis of polarization but upon reversal the phase difference between the electric and the magnetic field strength changes by 180°. Thus also the rotation of the polarization axis is reversed and the wave will arrive in its original state.

To show formally how a magneto-optically active material breaks reciprocity and that an optically active material does not, we insert both types of tensors into equation 12 and check whether the Lorentz reciprocity holds. For the magneto-optically active tensor this gives:

$$\nabla \cdot (\mathbf{E}' \times \mathbf{H}'' - \mathbf{E}'' \times \mathbf{H}') = \\ - \varepsilon_0 \gamma \omega (\mathbf{E}'' \cdot (\mathbf{B}_{\text{ext}} \times \mathbf{E}') - \mathbf{E}' \cdot (\mathbf{B}_{\text{ext}} \times \mathbf{E}'')). \quad (30)$$

The terms $\mathbf{E}''\varepsilon\mathbf{E}'$, $\mathbf{E}'\varepsilon\mathbf{E}''$, $\mathbf{H}''\mu\mathbf{H}'$and $\mathbf{H}'\mu\mathbf{H}''$ are omitted in the equation as they cancel each other. Because $\mathbf{E}' \cdot (\mathbf{B}_{\text{ext}} \times \mathbf{E}'')$ is equal to $-\mathbf{E}'' \cdot (\mathbf{B}_{\text{ext}} \times \mathbf{E}')$, the right-hand side can be simplified to $2\varepsilon_0 \gamma \omega \, \mathbf{E}' \cdot (\mathbf{B}_{\text{ext}} \times \mathbf{E}'')$, which is unequal zero for general fields and reciprocity is broken. As explained in section 2.6, for such materials the scattering matrix is potentially asymmetric which allows for the construction of isolators. On the other hand, if one inserts the optically active tensor from equations 28 and 29 into equation 12, one yields:

$$\nabla \cdot (\mathbf{E}' \times \mathbf{H}'' - \mathbf{E}'' \times \mathbf{H}') = \\ - \omega^2 \xi \left(-\mathbf{E}'' \cdot \mathbf{H}' + \mathbf{E}' \cdot \mathbf{H}'' - \mathbf{H}'' \cdot \mathbf{E}' + \mathbf{H}' \cdot \mathbf{E}'' \right) = 0. \quad (31)$$

Like in equation 30 the terms containing only electric or only magnetic fields were omitted. One can see here the importance of the coupling term in equation 29. Would it have been omitted, the right side of equation 31 would not have been zero and in this case an optically active material would appear nonreciprocal, which it is not.

2.11 MAGNETO-OPTICALLY ACTIVE MATERIALS

If one wants to compare the performance of materials for magneto-optical devices such as a Faraday rotator, the two most important parameters are the Verdet constant and the propagation loss. A high Verdet constant ensures that, for a given magnetic biasing field, the necessary Faraday rotation is achieved over a short distance and a low propagation loss ensures a low device loss. To take both into account, a figure of merit is defined that states how far the polarization can be rotated per 1 dB propagation loss, i.e. the ratio of Faraday rotation and propagation loss,

$$FoM = \frac{|FR|}{\alpha}, \quad (32)$$

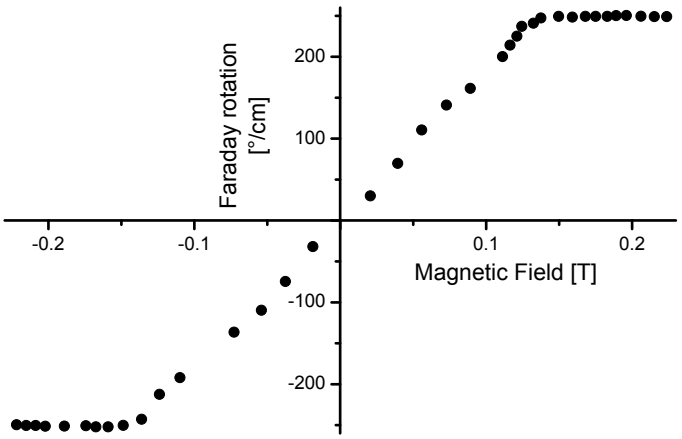

Figure 11: Faraday rotation of YIG as a function of the magnetic biasing field for a wavelength of 1.153 µm. Data was taken from [61].

where FR is measured in degree per cm and α in dB per cm.

2.11.1 *Rare earth iron garnets*

Due to their low absorption combined with large Faraday rotation at telecom wavelengths, rare earth iron garnets are the most used material for integrated magneto-optical devices. For the near infrared the choice of yttrium as a rare earth iron leads to magneto-optical material with high figure of merit. Yttrium iron garnet (YIG) has a chemical formula of $Y_3Fe_5O_{12}$. YIG is a soft ferrimagnetic material which means its magnetization will saturate but it will feature little remanent magnetization. As the Faraday rotation is proportional to the magnetization, it will also saturate (see Fig. 11). The magnetic field for that the Faraday rotation saturates is roughly 0.15 T. A monocrystalline YIG film has a saturation Faraday rotation between 200 and 270 °/cm [61–64], a propagation loss of 1 dB/cm [62] and refractive index of 2.17 [65] at a wavelength of 1.55 µm. Faraday rotation and losses yield together a figure of merit of 200 and 270 °/dB. The magneto-optical effect of YIG in the near-infrared is caused by a paramagnetic transition for photon energies close to 2.5 eV [66].

If the yttrium in YIG is partially exchanged with cerium, an even larger Faraday rotation is possible. Depending on the cerium content, the Faraday rotation of Ce:YIG can vary from -740 to -4500 °/cm [67–69]. In the same way the propagation loss varies from 0.52 dB/cm [67] to 5.8 dB/cm [68]. Accordingly, Ce:YIG features a figure of merit between 865 and 1420 °/dB. Its refractive index is 2.21 [68]. The much larger Faraday rotation of Ce:YIG compared to YIG is linked to the occurrence of a paramagnetic transition at 1.4 eV [56], which is much closer to the wavelength of interest compared to 2.5 eV in YIG and therefore creates a stronger effect. The transition is believed to be between the 4f level of cerium and the 3d level of the iron [70, 71].

Note that 5.8 dB/cm is the propagation loss of a TM slab waveguide and thereby only an upper estimate for the material losses.

Despite the excellent figure of merit, it is difficult to combine rare earth iron garnets with silicon waveguides. The main reason for this is the lattice and thermal mismatch of the garnet crystal with the silicon [72, 73]. In the past, this issue was addressed by bonding a single crystalline garnet crystal on top of the silicon [74]. The wave is in this case guided inside a silicon waveguide and its evanescent field interacts with the on top bonded garnet creating the nonreciprocal effect. More recently, groups managed to sputter garnets on top of silicon. Polycrystalline YIG films were sputtered directly onto silicon while Ce:YIG films need a few nanometre thick interlayer of YIG to grow on top of silicon [25, 72]. From the device standpoint, sputtering is the preferable method as it allows for a local application of the magneto-optical material and will allow for a monolithic system design. While the sputtered thin film was shown to have a Faraday rotation comparable to single-crystalline films (between -2700 and $-3000\,°/\mathrm{cm}$), roughly an order of magnitude higher losses were measured (48 dB/cm) [75], leading to a much reduced figure of merit of $56\,°/\mathrm{dB}$. The higher losses are believed to be due to scattering at grain boundaries and surface roughness [76, 77]. Both methods allow only for an interaction with the magnetic material on top of the waveguide. In case of bonding the reason is trivial as the garnet crystal can only be placed on top of the silicon chip. But also for sputtering this is true because so far it has only been possible to crystallize the film on top of the waveguide. It has not yet been achieved to cover the sidewalls of a waveguide with a crystallized garnet film. As will be explained in section 2.12.2, this limits the use of garnet films for magneto-optical phase shifts to TM modes.

2.11.2 *Magneto-optically active polymers*

Polythiophenes have been reported to be a surprising candidate for future magneto-optical applications. Fig. 12 summarizes the found Verdet constants of poly(3-alkylthiophene)s and poly(3-alkoxythiophene)s. [78–81]. Both materials are polymer chains of thiophene rings with either an alkyl or alkoxy group attached to each monomer. Especially the poly(3-alkoxythiophene) shows very promising magneto-optical properties for 1550 nm optical wavelength, which is commonly used in optical communication. With a Verdet constant of $10^4\,°/(\mathrm{Tcm})$ it has a roughly 3 times higher Faraday rotation than Ce:YIG for a biasing field of 1 T. Poly(3-alkylthiophene)s feature a one to two orders of magnitude lower Verdet constant which is comparable to YIG in the near infrared. Unfortunately, the authors of the mentioned studies only give the optical material losses in arbitrary units, but studies on polythiophene slab waveguides found propagation losses between 2 and 4 dB/cm [82, 83]. This yields an estimated figure of merit between 2500 and $5000\,°/\mathrm{dB}$ for poly(3-

Because polymers are diamagnetic their magnetisation doesn't saturate. Therefore, we use here the Verdet constant and not the saturation Faraday rotation, as we did for the garnets.

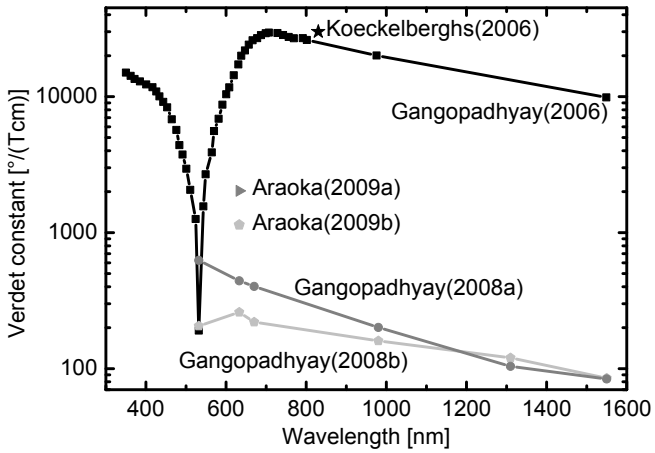

Figure 12: Comparison of studies of Verdet constants of different polythiophenes. Koeckelberghs(2006) and Gangopadhyay(2006) are poly(3-octyloxythiophene) [78, 79], Gangopadhyay(2008a) and Araoka(2009a) are poly(3-hexylthiophene) [80, 81], and Gangopadhyay(2008b) and Araoka(2009b) are poly(3-dodecylthiophene) [80, 81].

alkoxythiophene)s and between 22 and 43 °/dB for poly(3-alkylthiophene)s.

It has been found that the regioregularity of the thiophene has a strong influence on the magneto-optical properties [78, 84]. The term regioregularity is explained in Fig. 13a and b. The alkyl or alkoxy group can attach in two positions on the thiophene ring. For a regioregular polythiophene they do this in such way that they always point in the same direction of the chain. For a regiorandom polythiophene, as the term indicates, they orient randomly. In [84] an exponential relationship between regioregularity and Verdet constant was found (Fig. 13c). The regioregularity is in this case defined as the ratio of regularly oriented monomers to the total number of monomers.

Despite this promising magneto-optical performance, the effect in these materials seems to be elusive. There is only one study that shows the strong Faraday rotation in the near infrared [79] and the origin of the effect is not understood nor is understood what leads to the big difference between poly(3-alkylthiophene)s and poly(3-alkoxythiophene)s.

2.11.3 *Nanoparticles in a dielectric matrix*

Iron oxide in form of magnetite (Fe_3O_4) and maghemite (γ-Fe_2O_3) has a very large Faraday rotation, 7.3×10^8 °/cm [97] for magnetite and 2.5×10^4 °/cm [98] for maghemite at a wavelength of 1550 nm. This strong rotation is unfortunately paired with impractically high propagation losses. For magnetite the damping constant is 4.7×10^8 dB/cm [99] and for maghemite it is 3.5×10^5 dB/cm [100] yielding a FOM of 1.55 °/dB and 0.07 °/dB respectively. The high losses

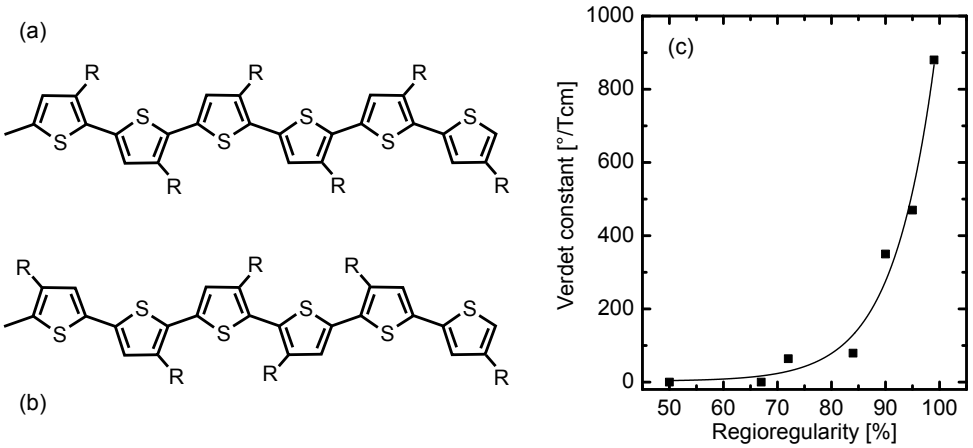

Figure 13: (a) A regioregular thiophene chain. The alkyl or alkoxy group is denoted as R. (b) A regiorandom thiophene chain. (c) The relationship between regioregularity and Verdet constant [84].

can be mitigated by producing nanoparticles with diameters ranging from few to few tens of nanometre. These particles are then brought into a silica or polymer host matrix. With this dilution of the iron oxide content the losses are as well reduced. Fig. 14 summarizes the achieved Faraday rotation and FOM in such material systems. Table 1 lists host as well as nanoparticle materials, particle diameter and nanoparticle filling fraction. The Faraday rotation ranges from a few to a few hundreds degree per centimeter and thereby can reach that of YIG. However, the maximal possible figure of merit is with around 3 °/dB almost two orders lower than that of YIG.

The Faraday rotation in these systems was found to be proportional to the volume fraction of nanoparticles [101]. This means that with higher concentration than those listed in table 1, significantly higher Faraday rotation can be achieved. For instance, Ref. [102] shows that cobalt ferrite particles ($CoFe_2O_4$) in a silica matrix feature a Faraday rotation of 6.6×10^3 °/cm for a particle concentration of 39 vol% at 820 nm. But this large value comes again at a cost of intolerable high propagation losses of 1.4×10^4 dB/cm.

Besides particle concentration the Faraday rotation is affected by the particle size. Ref. [92] shows for magnetite particles that the spectral maximum of the Faraday rotation redshifts from 435 nm to 640 nm if the particle diameter changes from 8 nm to 200 nm. Ref. [90] shows that the Faraday rotation of maghemite particles at 633 nm wavelength reduces by almost a factor of two if the particle size is increased from 6 nm to 10 nm. Contrary to this, Ref. [89] showed a more than threefold increase at 810 nm for the Faraday rotation of maghemite particles if their diameter increases from 6 nm to 22 nm. The mechanism of this size dependence is not well understood. Ref. [92] hypothesize size dependent lattice distortions or changes of the Fe occupation at specific lattice cites; Ref. [90] sees the particle's internal

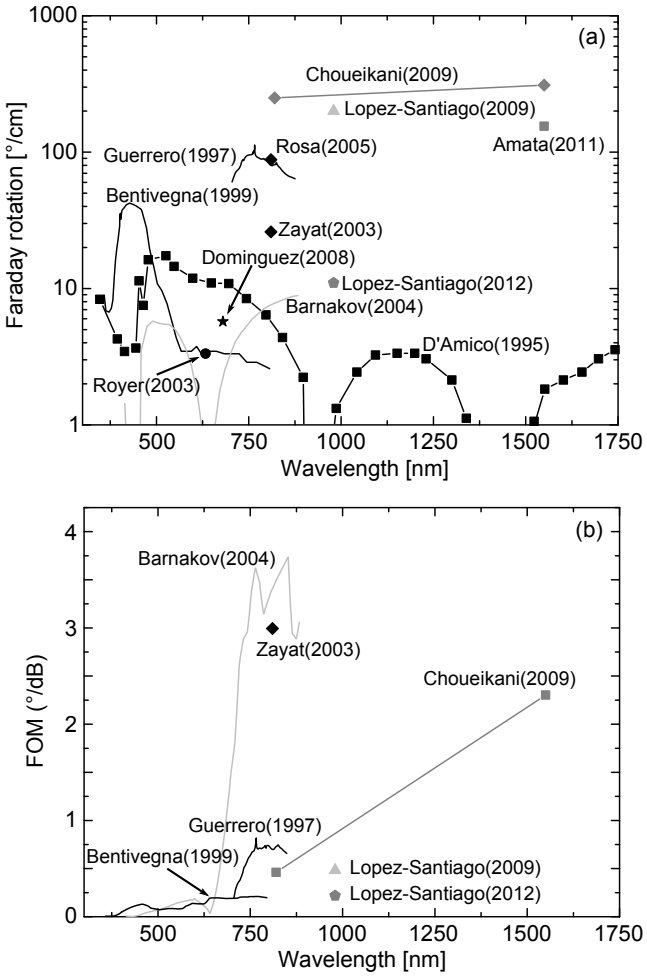

Figure 14: (a) Comparison of the Faraday rotation in various nanoparticle composites. (b) FOM. Details can be found in Table 1.

	particle material	matrix material	particle size	filling fraction
D'Amico(1995) [85]	$\gamma - Fe_2O_3$	PVA	7 nm	4.5 wt%
Bentivegna(1999) [86]	$\gamma - Fe_2O_3$	SiO_2	10.5 nm	0.28 vol%
Dominguez(2008) [87]	$\gamma - Fe_2O_3$	SiO_2	12 nm	5.9 wt%
Guerrero(1997) [88]	$\gamma - Fe_2O_3$	SiO_2	20 nm	12 vol%
Rosa(2005) [89]	$\gamma - Fe_2O_3$	SiO_2	21.8 nm	11 vol%
Royer(2003) [90]	$\gamma - Fe_2O_3$	Water	6.1 nm	0.2 vol%
Zayat(2003) [91]	$\gamma - Fe_2O_3$	Vycor glass	11 nm	10.4 wt%
Barnakov(2004) [92]	Fe_3O_4	PMMA	15 nm	<10 vol%
Lopez-Santiago(2009) [93]	Fe_3O_4	PMMA	40 nm	1 wt%
Amata(2011) [94]	$CoFe_2O_4$	SiO_2	9 nm	0.7 vol%
Choueikani(2009) [95]	$CoFe_2O_4$	SiO_2/TiO_2	9 nm	1.5 vol%
Lopez-Santiago(2012) [96]	$CoFe_2O_4$	PBMA	20 nm	4 wt%

Table 1: Various nanoparticle composites.

magnetic field responsible whereas Ref. [89] suspects a reduced magnetization on the particle's surface.

In conclusion, iron oxide nanoparticles can achieve Faraday rotation similar to YIG but feature roughly two orders of magnitude higher losses. They are still interesting for applications because of their broad compatibility with host materials. For instance, a polymer host material would allow various processing methods like dropcasting or spin coating and would not pose a problem like lattice mismatch as encountered in silicon garnet systems.

2.12 MAGNETO-OPTICAL EFFECTS IN WAVEGUIDES

2.12.1 *Faraday rotation*

An analogue to the description of Faraday rotation in a waveguide is an evanescent waveguide coupler (Fig. 15). The power is coupled from one mode to the other via the overlapping evanescent waves of the two modes in the respective waveguides. The amount of optical power that can be coupled from one waveguide to the other depends on the mismatch of propagation constants of the two waveguide modes. For identical propagation constants 100% of the power can be coupled from one waveguide to the other. For differing propagation constants at first some part of the power will be coupled from one waveguide to the other. But after some distance the phase relation between the two modes will have changed to be exactly out of phase with the initial excitation and that part of the power that has been transferred from one waveguide to the other will be transferred back. The bigger the propagation constant mismatch, the shorter the distance in which this process occurs and the less amount of power can be coupled from one waveguide to the other. The fraction of the total power that can be coupled from one waveguide to the other can be calculated by [103]

$$\eta = \frac{|\kappa|^2}{|\kappa|^2 + |\frac{\Delta\beta}{2}|^2}, \tag{33}$$

where $\Delta\beta$ is the mismatch in propagation constant between the two modes and κ is the coupling constant. Faraday rotation can be understood in the same way, only that in this case the coupling is not between two modes in two separate waveguides but between the TM and TE mode in the same waveguide. The coupling constant can in this case be calculated by $\kappa = \frac{\omega\varepsilon_0}{4} \iint \mathbf{E}_{\mathrm{TE}}^{\dagger} \left(j\gamma \mathbf{B}_{\mathrm{ext}} \times \mathbf{E}_{\mathrm{TM}}\right) dA$ [19], which is an integral over the waveguide cross section. A high coupling constant can therefore be achieved if both modes strongly overlap with the magneto-optical material as well as with each other, if both modes have strong fields orthogonal to the magnetic biasing field and finally if the material features a high Verdet constant. For plane waves in a homogeneous medium travelling along the magnetic bias field,

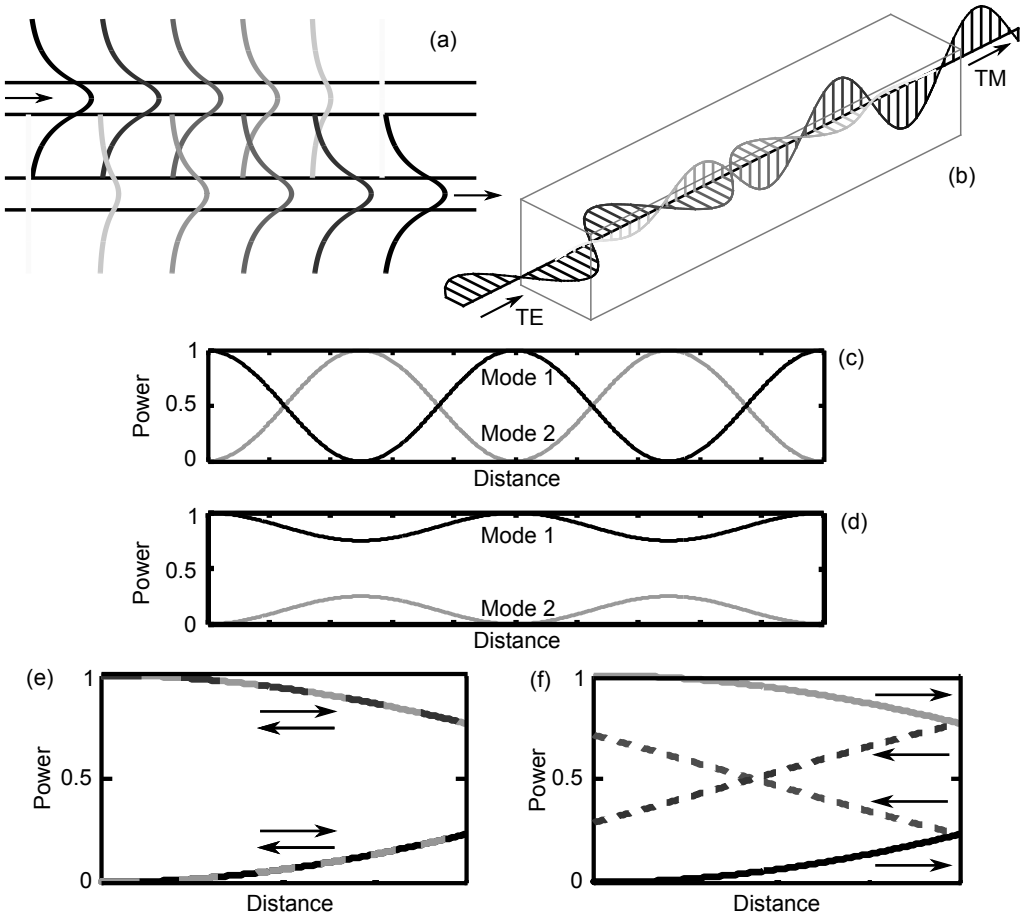

Figure 15: Comparison of the coupling between two adjacent waveguides and the magneto-optical coupling between the TE and TM mode. (a) A mode is launched in the upper waveguide and excites a mode in the lower waveguide. (b) A TE mode is launched into a magneto-optically active waveguide and excites a TM mode. (c), (d) Comparison of coupling between two modes with matching phase propagation (c) and unmatched phase propagation (d). (e) For reciprocal coupling like in (a) upon reversal of propagation direction, the system is converted back to its initial state. (f) For nonreciprocal coupling like in (b), the system is not converted back to its original state upon reversal.

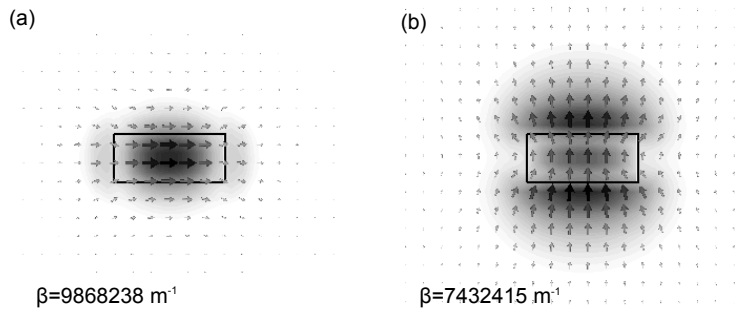

Figure 16: Birefringence and electric fields for a single-mode waveguide with silicon core and silica substrate for $\lambda = 1.55\,\mu m$ with a cross-section of $500\,nm \times 220\,nm$: (a) TE mode and (b) TM mode.

the coupling is maximized and κ becomes the Faraday rotation measured in rad/m. An important difference between the two examples is that the coupling between two waveguides is usually reciprocal whereas Faraday rotation is not. This means that upon reversing the propagation direction the waveguide coupler reverses to its original state whereas the Faraday rotation couples further from the initial mode to the second mode.

Because of equation 33 it is very difficult to implement integrated waveguides that exhibit a strong Faraday rotation. Due to shape anisotropy and differing substrate and cladding materials, the field distribution and with that the propagation constant of TE and TM mode are strongly different. Fig. 16 shows a typical single-mode waveguide for a wavelength of 1.55 µm. Due to the shape anisotropy the field patterns of the two modes look very different yielding a $\Delta\beta$ of $2.4 \times 10^6\, m^{-1}$. Assuming a Faraday rotation of $10^6\,°/m$, which is among the highest reported for this wavelength region, and assuming 100 % overlap between the mode and the magneto-optical active material, the coupling constant becomes $1.75 \times 10^4\, m^{-1}$. Thus, the maximum fraction of power that can be coupled from one mode to the other is only $\eta = 2.1 \times 10^{-4}$.

2.12.2 *Magneto-optical phase shift*

Owing to this severe limitation of Faraday rotation in form-birefringent waveguides, usually another magneto-optical effect is used in integrated waveguides that does not rely on coupling between modes. Under the right conditions the phase propagation constant of a single mode can be made direction-dependent. To illustrate how this can be achieved we have shown a slab waveguide in Fig. 17. The electric fields of a TM mode travelling in a slab waveguide are shown. For a symmetric waveguide as in this example the transverse fields are symmetric and the longitudinal fields are antisymmetric. From this follows that fields described in right-handed polarized and left-

handed polarized light have no symmetry. The centre of gravity for the right-handed polarized field tends towards the upper half of the waveguide and that of the left-handed polarized field tends towards the lower half. The reason for this behaviour can be intuitively understood in the ray optics description as done in Fig. 17c. The ray will bounce up and down in the waveguide. Upon reflection it will penetrate into the waveguide cladding and re-enter into the waveguide core after some distance. This is referred to as the Goos-Hänchen shift [104] and the distance of the shift depends on the bounce angle of the ray and the refractive index profile. Since the electric field is always orthogonal to the ray propagation, the electric field needs to rotate upon reflection. Exactly this rotation implies the concentration of right-handed polarized fields at the upper half and left-handed polarized fields at the lower half if the wave travels from left to right. If the ray in Fig. 17c was instead travelling from right to left, the handedness would be reversed with left-handed polarized fields at the top and right-hand fields at the bottom.

The change of handedness upon reversal of direction can be exploited to break reciprocity. In section 2.10.1 it is shown that a magnetic field can cause differing permittivities for the left- and right-hand polarization. As a consequence a wave travelling from left to right will see a different permittivity in the cladding compared to a wave travelling right to left. As shown in Fig. 17d, the Goos-Hänchen shift will be different for the forward and the backward travelling case.

If this difference in shift adds up constructively upon many reflections, it leads to difference in propagation constant and wavelength, which means that the wave accumulates a differing phase for the opposite propagation direction. In section 2.14 and in chapter 4 it will be shown how this magneto-optical phase shift can be exploited for isolators and circulators. For the phase shift to appear the material needs to be magnetized orthogonal to the plane in which the circular polarization appears. For the example in Fig. 17d this is normal to the image plane.

A necessary prerequisite for this shift to cause a nonreciprocal phase-shift is asymmetry, because the field has opposite handedness underneath and above the waveguide. For a symmetric waveguide as in Fig. 17 the Goos-Hänchen shift would be slightly reduced on the top side and slightly increased on the bottom side, culminating in zero change from the unmagnetized case. The necessary asymmetry can be introduced in form of the refractive index profile, by having a magneto-optically active material only on one side of the waveguide or as shown in the next section by curvature (Fig. 21). There is no phase shift for a TE slab mode as the electric field has only a x-component and thereby is purely linearly polarized. Linearly polarized light can be described as equal parts left-handed and right-handed polarized

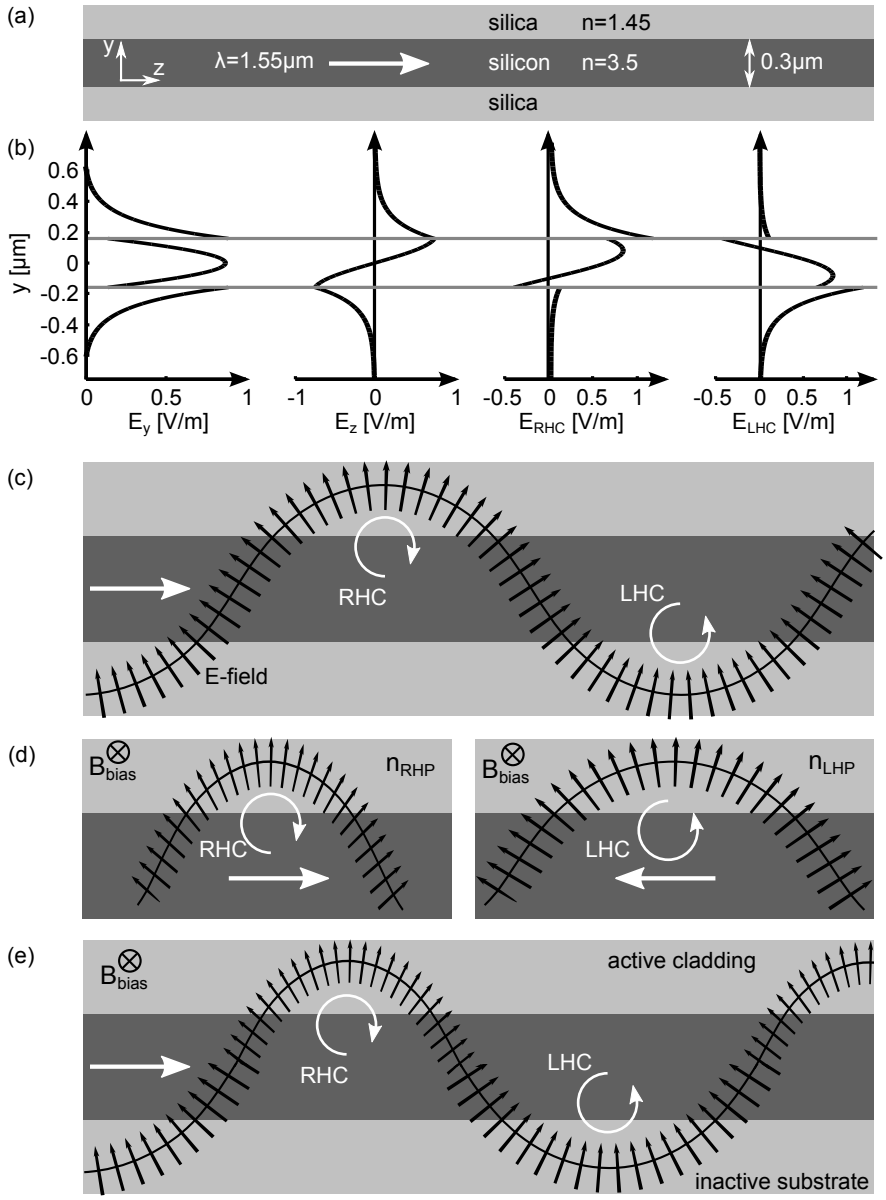

Figure 17: TM mode in a slab waveguide. (a) Geometry. (b) Electric field distribution split in x- and z-polarization as well as right-hand and left-hand polarization. (c) Ray optics depiction of the travelling wave. For the reversed direction the handedness of the polarization changes with left-handed polarized light on top and right-handed polarized light on the bottom (d). (e) Ray optics depiction for a waveguide with magneto-optically active cladding and inactive substrate. The shift in the substrate is the same as in (c), the shift in the cladding is reduced.

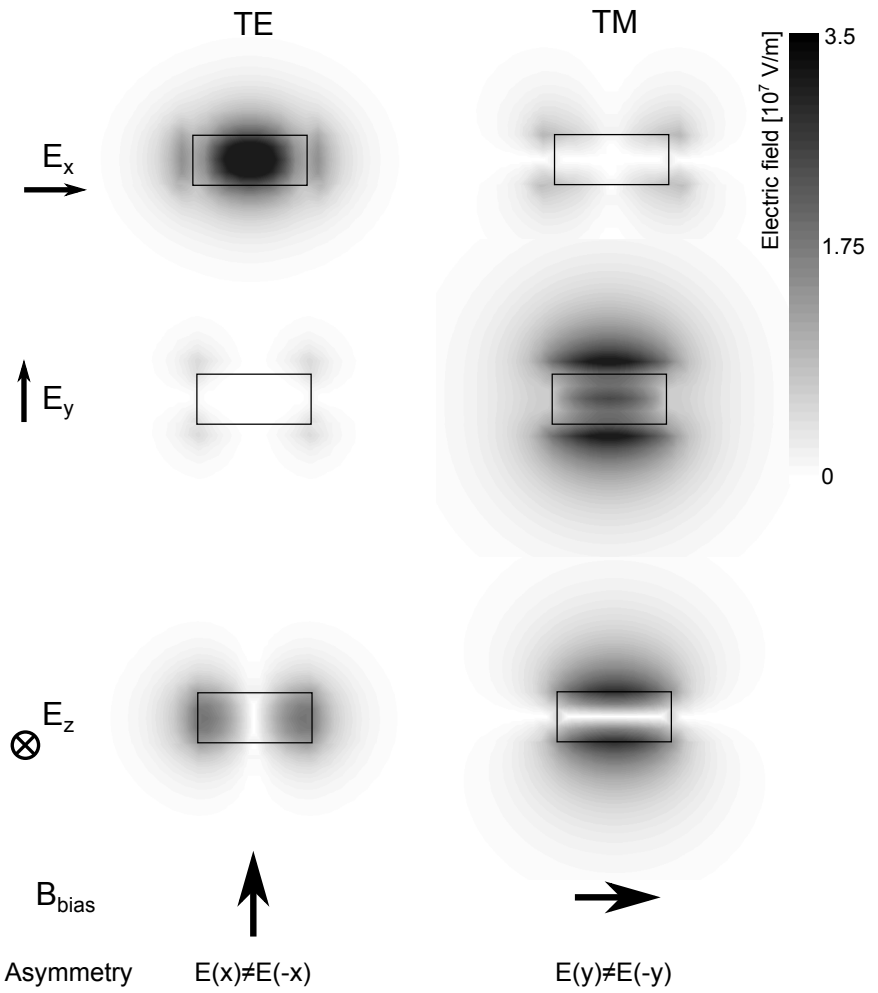

Figure 18: Electric field of the TE and TM mode of a silicon channel waveguide embedded in silica. The waveguide has a cross-section of 500 nm × 220 nm and the wavelength is 1.55 µm. Further, the required magnetic biasing field and asymmetry are shown to enable a magneto-optical phase shift in the two cases. The asymmetry condition is always with respect to the waveguide centre.

light and therefore any effect distinguishing between the two polarizations averages to zero.

For a channel waveguide the situation becomes a bit more complicated. Fig. 18 shows the electric fields of the first two modes of a silicon waveguide. Through the introduction of a second pair of interfaces both modes have now fields in all three coordinate directions. For the TM mode the situation is not much changed compared to the slab waveguide. Although there is a small x-component, the field is mainly polarized in y- and z-direction and the magneto-optical phase shift occurs in the same way as in the slab. For the TE mode magneto-optical behaviour is strongly changed in comparison to the slab waveguide. The introduction of the two interfaces leads to an electric field component in z-direction and with that to the possibility

More precisely one should refer to the mode as a quasi-TM mode because its magnetic field has a weak longitudinal component. We omit such a distinction here.

of a magneto-optical phase shift. Since the light is circularly polarized in the xz-plane, the magnetic biasing field must be applied along y-direction and the asymmetry is needed with respect to the yz-plane.

Usually the relative magneto-optical change in refractive index is very weak and the change in propagation constant can be calculated from the mode pattern in the unmagnetized case with the help of perturbation theory [19]

$$\Delta\beta_{MO} = 2\omega\varepsilon_0 \frac{\iint \mathbf{E}^* \Delta\varepsilon \mathbf{E} \mathrm{d}x\mathrm{d}y}{\iint (\mathbf{E} \times \mathbf{H}^* + \mathbf{E}^* \times \mathbf{H})_z \, \mathrm{d}x\mathrm{d}y} \,, \tag{34}$$

where $\mathbf{E}$ and $\mathbf{H}$ are the electric and magnetic field of the unpertubed mode and $\Delta\varepsilon$ is a tensor representing the magneto-optical perturbation of the permittivity and is thus composed of the off-diagonal components of equation 25. We use the convention that the difference in propagation constant between the forward and the backward running mode is referred to as $\Delta\beta_{MO}$ and the difference between the unperturbed and the perturbed mode is $\delta\beta_{MO}$. This implies that $\Delta\beta_{MO} = 2\delta\beta_{MO}$.

2.13 MAGNETO-OPTICAL EFFECTS IN RING RESONATORS

If we bend the waveguide in Fig. 17 to a ring we can create an effect that is the analogue to the Zeeman splitting in section 2.10.1. In the case of the Zeeman effect the degeneracy of the absorption of left- and right-handed circularly polarized light is lifted. In the case of a ring resonator the degeneracy of the resonance of a clockwise and counter-clockwise travelling wave is lifted by a magnetic biasing field. How this happens is schematically shown in Fig. 19. Provided there is some asymmetry that enables a magneto-optical phase shift, only for one of the two possible directions of the ray path the path can be continued self-consistently. Only the path that can be continued selfconsistently will be in resonance and so the resonance spectrum is split as shown in Fig. 19c. Just like the magneto-optical phase shift, the magneto-optical frequency shift can be calculated with the help of perturbation theory [13, 105]:

$$\Delta\omega = \omega_0 \frac{\iint \mathbf{E}^* \Delta\varepsilon \mathbf{E} \, \mathrm{d}x\mathrm{d}y}{\iint \varepsilon \mathbf{E}^* \cdot \mathbf{E} \, \mathrm{d}x\mathrm{d}y} \,, \tag{35}$$

where ω_0 is the unpertubed resonance frequency, $\mathbf{E}$ is the perturbed electric field, $\Delta\varepsilon$ are the off-diagonal components of the tensor in equation 25 and ε are the diagonal components of that tensor.

For a TE mode to show resonance splitting, the biasing field needs to be in vertical direction (Fig. 18) and, accordingly, a homogeneous out-of-plane field is needed (Fig. 20a). In case of a TM mode, the question of the shape of the biasing field is more complex. Because of the need for an in-plane biasing field, the field needs either to be

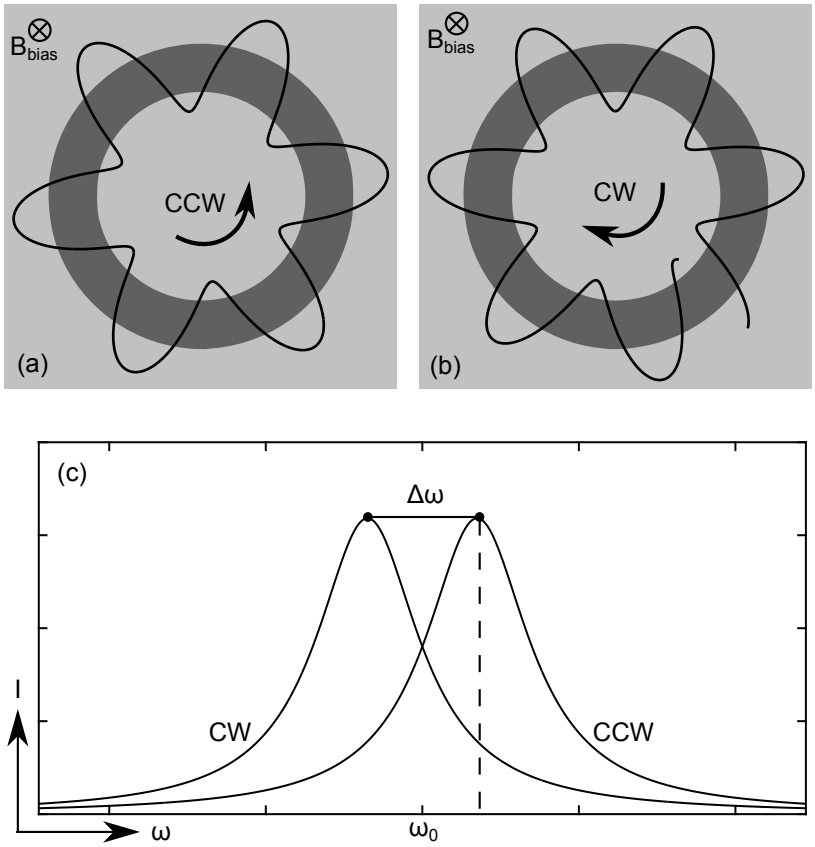

Figure 19: Ray path in a ring resonator: (a) Counter-clockwise travelling ray at the resonance frequency indicated in (c). (b) Clockwise travelling ray at the same frequency is indicated in (c), which is off resonance for this direction. (c) Frequency spectrum of a ring resonator which features magneto-optical frequency splitting.

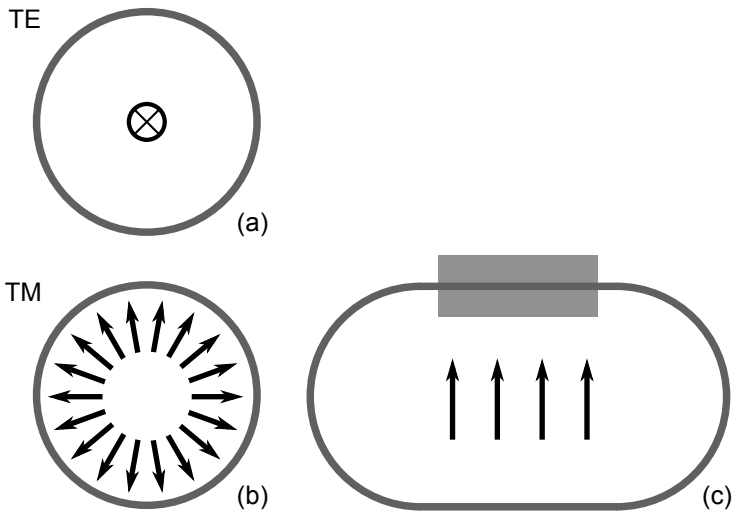

Figure 20: Possible ways to apply the magnetic field: For the TE mode an out-of-plane bias is needed (a). For TM mode the biasing field needs to lie in plane. It can either be divergent (b) or homogeneous with only part of the ring resonator waveguide magneto-optically active (c).

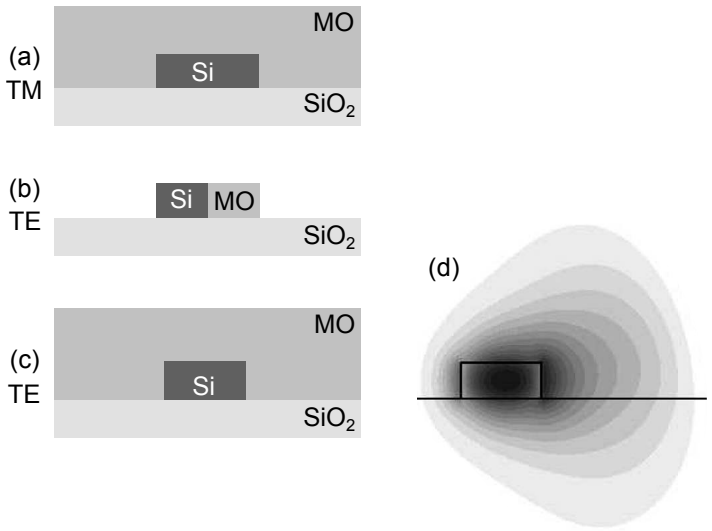

Figure 21: Possible ways to introduce asymmetry into the system. For the TM mode a strongly magneto-optically active cladding can be used in combination with a weakly magneto-optically active substrate like silica (a). The asymmetry for the TE mode can either be created by an asymmetric waveguide core profile (b) or by the curvature of the ring resonator with a symmetric material profile (c). In (d) an electric field plot in logarithmic scaling is shown. The cladding refractive index is 1.6, the ring radius is 1.5 µm and a wavelength of 1.55 µm was used [106].

divergent (Fig. 20b) [26] or homogeneous with only part of the waveguide magneto-optically active (Fig. 20c) [25]. In case of the diverging biasing field, the device size needs to be in the millimetre range in order to achieve a strong enough biasing field. Albeit a homogeneous biasing field offers the possibility for a much more compact device, only part of the ring waveguide can be magneto-optically active since the sign of the phase shift is opposite in opposing sections of the ring and a fully active ring resonator would have in sum no phase shift.

The necessary asymmetry can be introduced in the TM case by simply using a magneto-optically active material as cladding and an inactive material as substrate (Fig. 21a). This geometry was experimentally realized by either bonding a garnet on top of the silicon waveguide [26] or by depositing a garnet with pulsed laser deposition [25].

In the TE case the asymmetry can either be produced by an asymmetric waveguide core as shown in Fig. 21b [107] or by using the curvature of the ring resonator as shown in Fig. 21c and d. The curvature is beneficial in two ways: It distorts the electrical field in such way that it is focused towards the outer interface of the waveguide. Further, the volume that the electric field interacts with grows linearly with the radius and thus we have a bigger volume of magneto-optically active material on the outer side of the waveguide

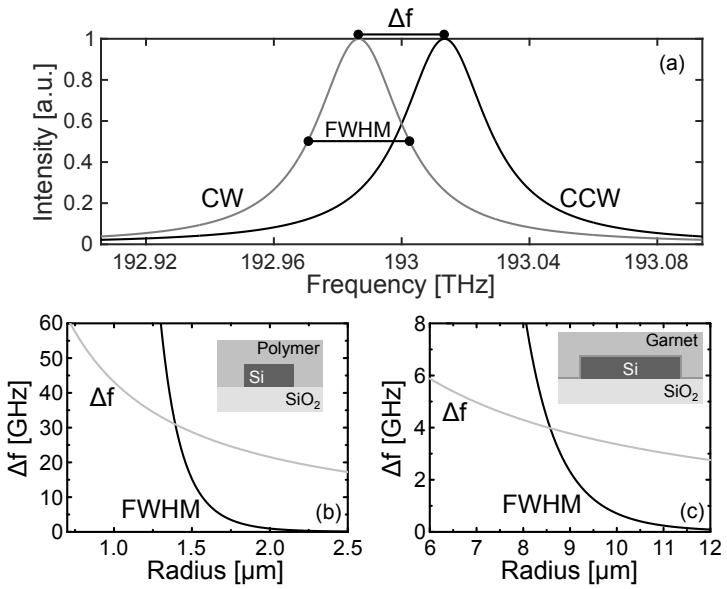

Figure 22: Comparison of the frequency splitting due to the curvature between a magneto-optically active polymer and a garnet cladding. (a) General spectral dependence of the optical field intensity inside a ring resonator with frequency splitting between the clockwise (CW) and the counter-clockwise (CCW) travelling mode. (b) and (c) frequency splitting and FWHM for the shown geometry.

compared to the inner side of the waveguide, which is an additional asymmetry [106].

The utilization of the waveguide's curvature is only a feasible concept for a system with a strong index contrast between waveguide core and cladding. The reason for this is illustrated in Fig. 22. To make use of the magneto-optical frequency splitting, the width of the resonance needs to be smaller than frequency splitting between the clockwise and the counter-clockwise mode (see next section). The resonance width is measured by the full width at half maximum (FWHM), which is the width of the curve at half the maximal intensity. Assuming the dominant loss mechanism is bending loss, the FWHM decreases exponentially with the ring radius [108]. Further, the frequency splitting decreases proportional to the inverse radius [106]. As the former falls faster than the latter, there is a radius for which the two curves cross. Hence, for larger radii the FWHM will be below the frequency splitting and such radii are thus applicable for magneto-optical devices. Fig. 22b and c show the behaviour of both curves for the two cases: Firstly, a 500 nm $\times$ 220 nm silicon waveguide with a magneto-optically active polymer cladding and a silica substrate. The refractive indices of silicon, polymer and silica are $n_{Si} = 3.5$, $n_{poly} = 1.6$ and $n_{SiO2} = 1.45$. Secondly, a 1000 nm $\times$ 220 nm silicon waveguide with garnet cladding, a YIG adhesive layer (see section 2.11.1) and as well a silica substrate. The refractive indices of garnet and YIG are $n_{garnet} = 2.57$ and $n_{YIG} = 2.2$. Both, the polymer and

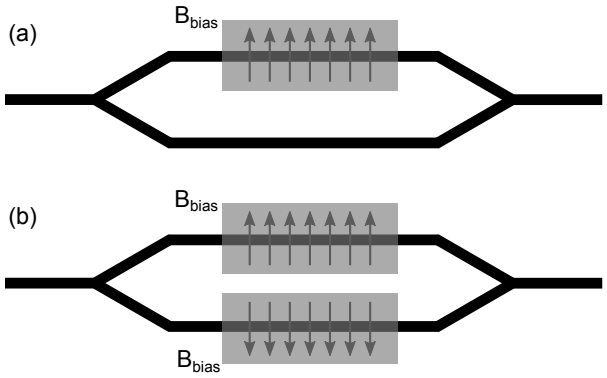

Figure 23: An isolator utilizing the magneto-optical phase shift of a TM mode in an Mach-Zehnder interfermeter. In (a) only one arm is covered with a magneto-optical active material. To achieve full isolation, a phase shift of $\delta\varphi = 45°$ is needed in this case. In (b) both arms are active and a opposing bias needs to be applied. This reduces the required phase shift to $\delta\varphi = 22.5°$.

the garnet cover the top and the side wall of the respective waveguide. For comparability, the off-diagonal component of the magneto-optical permittivity tensor is in both cases $\Delta\varepsilon = 0.01$. The depicted frequency splitting was calculated with equation 35. The required electric fields were obtained with eigenmode solver that can account for curved geometries [109]. The FWHM was calculated from the bending induced radiation losses from the obtained mode [13]. The two curves cross at a six times larger radius for the garnet cladding compared to the polymer cladding and the achievable frequency splitting is roughly an order of magnitude smaller. The reason for both is that due to the reduced index contrast the waveguide with the garnet cladding is much more weakly guiding and the modal energy is lost due to radiation before a sizeable asymmetry can be achieved that creates a strong frequency splitting.

For these reasons the only feasible concept of utilizing garnets with TE modes is that in Fig. 21b, where the waveguide core is part weakly magneto-optically active silicon and part garnet. The problem with this concept is that it was so far not possible to attach a garnet to the vertical silicon edge. Accordingly, no TE concept with garnets was thus far realized. On the other hand, the strong magneto-optical effect of polymers like those presented in section 2.11.2 has so far only been experimentally shown in thin films and not in integrated optical systems. In conclusion, there is no experimental implementation that uses the magneto-optical phase shift of a TE mode.

2.14 MAGNETO-OPTICAL ISOLATORS AND CIRCULATORS

2.14.1 *Mach-Zehnder interferometer*

A way to implement an isolator in an integrated fashion is to use a Mach-Zehnder interferometer. For this purpose a waveguide section with a magneto-optically active top layer is utilized. The device can be implemented with a homogeneous magnetic biasing field mainly acting on one arm or with an opposing biasing fields on both arms acting on both arms (see Fig. 23a and b). In case of the homogeneous biasing field, a magneto-optical phase shift of 45° is needed to achieve optical isolation as follows from the transmission in forward and backward direction. The transmitted power is:

$$P_T = |\left(Ae^{j(\varphi_1 \pm \delta\varphi)} + Ae^{j\varphi_2}\right)|^2 = 2A^2 + 2A^2\cos\left(\varphi_1 \pm \delta\varphi - \varphi_2\right), \quad (36)$$

where A^2 is the power carried by the wave in each arm, $\varphi_1 \pm \delta\varphi$ is the phase gain in forward and backward direction in the magneto-optically active arm and φ_2 is the phase gain in the inactive arm. For maximal transmission in forward direction the following condition must be fulfilled:

$$\varphi_1 + \delta\varphi - \varphi_2 = m\pi \quad (37)$$

with m being a natural number. The condition for minimal transmission in backward direction is:

$$\varphi_1 - \delta\varphi - \varphi_2 = (2l-1)\,\frac{\pi}{2} \quad (38)$$

with l as well being a natural number. Subtracting both equations yields $\delta\varphi = \left(m - l + \frac{1}{2}\right)\frac{\pi}{2}$, which amounts $\delta\varphi = \frac{\pi}{4} = 45°$ for $m = l = 1$. With both waveguides magneto-optically active and an opposing magnetic bias, the phase relation in equation 36 becomes $\varphi_1 \pm \delta\varphi - (\varphi_2 \mp \delta\varphi)$. In an analogous fashion, the required magneto-optical phase shift can be derived yielding $\delta\varphi = \left(m - l + \frac{1}{2}\right)\frac{\pi}{4}$. Hence, the needed phase shift is in this case $\delta\varphi = \frac{\pi}{8} = 22.5°$. A recent experimental implementation of such a scheme can be found in Ref. [110].

2.14.2 *Ring resonators*

2.14.2.1 *Temporal coupled-mode theory*

The other option to utilize the magneto-optical phase shift for isolation is a ring resonator. For that one couples the resonator to a waveguide as depicted in Fig. 24. The behaviour of such an arrangement can be described with the help of temporal coupled-mode theory [16, 111–113]. As we will use this approach in chapter 3 and

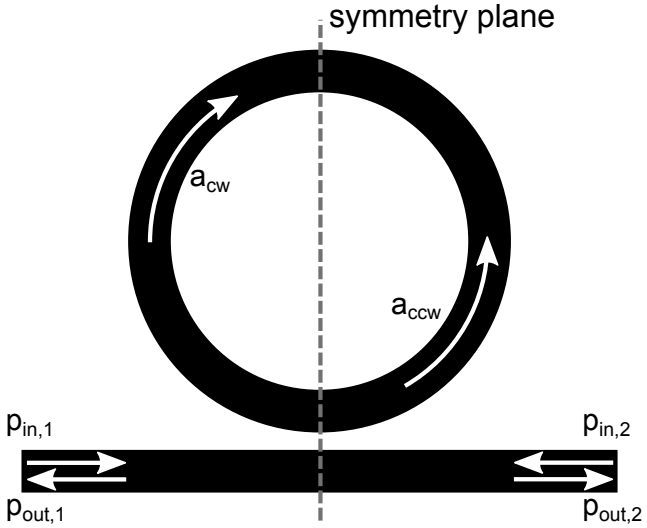

Figure 24: A ring resonator coupled to a waveguide.

4, we will now look in detail at this theory. The temporal coupled-mode theory models the interaction between unbound states, i. e. waves travelling in a waveguide or free space, and bound states like the modes in a resonator. We define the amplitudes of the travelling waves as $p_{in,i}$ and $p_{out,i}$. The former is the amplitude of the wave going into the system and the latter is that of the wave leaving the system. The amplitudes are defined such that $p^*p = P$ gives the time averaged power carried in that particular wave. For a ring resonator there are two modes with the amplitudes a_{cw} and a_{ccw} corresponding to the clockwise and counter-clockwise travelling wave, respectively. In case of the bound modes, the amplitudes are defined such that $a^*a = E_a$ gives the energy of the mode. We will now start by describing the system in Fig. 24 for the assumption of a lossless and reciprocal resonator and later drop these two simplifications, to see which system parameters are affected by nonreciprocity and resonator losses. For the mentioned simplifications, the evolution in time of the bound modes can be described by the following two equations [112]:

$$\frac{\mathrm{d}\mathbf{a}}{\mathrm{d}t} = \left(j\mathbf{\Omega} - \mathbf{\Gamma}_{cpl}\right)\mathbf{a} + \mathbf{K}^T\mathbf{p}_{in}, \tag{39}$$

$$\mathbf{p}_{out} = \mathbf{C}\mathbf{p}_{in} + \mathbf{D}\mathbf{a}, \tag{40}$$

where $\mathbf{a} = e^{j\omega t}\begin{pmatrix} a_{cw} & a_{ccw} \end{pmatrix}^T$,$\mathbf{p}_{in} = e^{j\omega t}\begin{pmatrix} p_{in,1} & p_{in,2} \end{pmatrix}^T$ and $\mathbf{p}_{out} = e^{j\omega t}\begin{pmatrix} p_{out,1} & p_{out,2} \end{pmatrix}^T$ are column vectors containing the time-dependent complex modal amplitudes, $\left(j\mathbf{\Omega} - \mathbf{\Gamma}_{cpl}\right)$ is a 2×2 diagonal matrix containing the complex resonance frequencies and $\mathbf{K}^T$,$\mathbf{C}$ and $\mathbf{D}$ are matrices describing the coupling between the modes. A derivation of equations 39 and 40 from first principles can be found in [114]. For equation 39 and 40 to be valid, the coupling between waveguide and resonator must be weak to ensure that the mode patterns are not

significantly affected by the coupling and that the change in resonance frequency from the uncoupled to the coupled resonator can be neglected [16, 113]. This means the coupling rates, $\mathbf{K}^T$ and $\mathbf{D}$, must be small compared to the resonance frequency such that the damping of the energy in the resonator within one period of oscillation is small. We use this formalism to describe the system's behaviour close to resonance. Thus, we assume the coupling parameters to be constant in this narrow frequency range.

The number of necessary parameters of the equation system can be greatly reduced by considering symmetries and energy conservation. We start by observing that the system in Fig. 24 has a mirror symmetry. Because the system does not change under the mirror operation, the mirrored fields are as well a solution. The original amplitudes are related to their mirrored counterparts by a matrix $\mathbf{M}$ of the form:

$$\begin{pmatrix} \tilde{a}_{cw} \\ \tilde{a}_{ccw} \end{pmatrix} = \begin{pmatrix} 0 & 1 \\ 1 & 0 \end{pmatrix} \begin{pmatrix} a_{cw} \\ a_{ccw} \end{pmatrix} = \mathbf{M} \begin{pmatrix} a_{cw} \\ a_{ccw} \end{pmatrix}, \tag{41}$$

$$\begin{pmatrix} \tilde{p}_{in,1} \\ \tilde{p}_{in,2} \end{pmatrix} = \mathbf{M} \begin{pmatrix} p_{in,1} \\ p_{in,2} \end{pmatrix}, \tag{42}$$

$$\begin{pmatrix} \tilde{p}_{out,1} \\ \tilde{p}_{out,2} \end{pmatrix} = \mathbf{M} \begin{pmatrix} p_{out,1} \\ p_{out,2} \end{pmatrix}. \tag{43}$$

Accordingly, a clockwise travelling mode becomes a counter-clockwise travelling one and vice versa and the waveguide modes switch labels. If we insert the mirrored amplitudes into equation 40, we get

$$\mathbf{M}\mathbf{p}_{out} = \mathbf{C}\mathbf{M}\mathbf{p}_{in} + \mathbf{D}\mathbf{M}\mathbf{a}. \tag{44}$$

Since the mirror operation does not change the geometry of our system, it must also leave the equations describing the optical behaviour unchanged. Thus, equation 40 and 44 are equivalent. Multiplying equation 44 from the left by $\mathbf{M}^{-1}$and comparing to equation 40 we obtain

$$\mathbf{D} = \mathbf{M}\mathbf{D}\mathbf{M}. \tag{45}$$

The same relation can be obtained for $\mathbf{C}$. We used here that $\mathbf{M}^{-1} = \mathbf{M}$. Further, we assume smooth coupling such that a_{cw} couples only to $p_{out,1}$ and a_{ccw} couples only to $p_{out,2}$. In consequence, we can conclude that

$$\mathbf{D} = \begin{pmatrix} d & 0 \\ 0 & d \end{pmatrix}. \tag{46}$$

This relation could have been obtained intuitively by just investigating Fig. 24 but the strict formalism will help us in chapter 4, where we have an additional rotational symmetry.

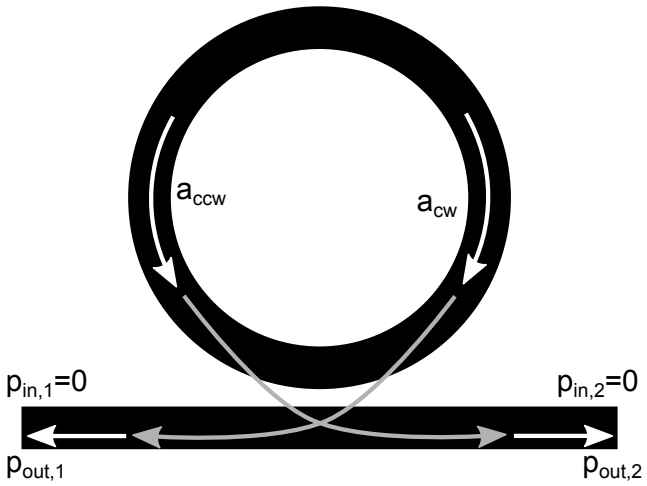

Figure 25: The resonator modes are loaded with energy and decay into the waveguide modes. There are no incoming waves.

To obtain a relation between $\mathbf{\Gamma}_{cpl}$ and $\mathbf{D}$, we look at a case where the resonator modes are loaded with energy but amplitudes of the incoming waveguide modes are zero, $p_{in,1} = p_{in,2} = 0$ [111, 112]. Therefore, the energy in the resonator will decay into the two outgoing waves. The change in total resonator energy is in this case

$$\begin{aligned}\frac{\mathrm{d}\mathbf{a}^\dagger\mathbf{a}}{\mathrm{d}t} &= \mathbf{a}^\dagger\frac{\mathrm{d}\mathbf{a}}{\mathrm{d}t} + \frac{\mathrm{d}\mathbf{a}^\dagger}{\mathrm{d}t}\mathbf{a} \\ &= \mathbf{a}^\dagger\left(j\mathbf{\Omega} - \mathbf{\Gamma}_{cpl}\right)\mathbf{a} + \mathbf{a}^\dagger\left(-j\mathbf{\Omega} - \mathbf{\Gamma}_{cpl}\right)\mathbf{a} \\ &= -2\mathbf{a}^\dagger\mathbf{\Gamma}_{cpl}\mathbf{a}, \quad (47)\end{aligned}$$

where we used equation 39 and the fact that $\mathbf{\Omega}$ and $\mathbf{\Gamma}_{cpl}$ are real diagonal matrices. Further, † denotes transposing the matrix and taking its complex conjugate. We know that the energy is carried away by $p_{out,1}$ and $p_{out,2}$ such that

$$\frac{\mathrm{d}\mathbf{a}^\dagger\mathbf{a}}{\mathrm{d}t} = -\mathbf{p}_{out}^\dagger\mathbf{p}_{out} = -\mathbf{a}^\dagger\mathbf{D}^\dagger\mathbf{D}\mathbf{a}, \quad (48)$$

where we used equation 40. Comparing equation 47 and 48, we obtain

$$2\mathbf{\Gamma}_{cpl} = \mathbf{D}^\dagger\mathbf{D}. \quad (49)$$

Using equation 46 we obtain $2\gamma_{cpl} = |d|^2$, where γ_{cpl} is one entry in $\mathbf{\Gamma}_{cpl}$. We can choose the reference plane of the modal amplitudes and with that the phase of d arbitrarily. We choose a reference plane such that d is real and we get

$$\sqrt{2\gamma_{cpl}} = d. \quad (50)$$

For the next parameter relation we utilize time-reversal symmetry. To that we first will investigate how the waves change under time-

reversal. The space- and time-dependent amplitudes of the counter-clockwise wave and the wave entering the system from the left are

$$a\left(t,\phi\right) = a_{ccw}e^{j\left(\omega t-\beta_\phi\phi\right)} \tag{51}$$

and

$$p\left(t,x\right) = p_{in,1}e^{j(\omega t-\beta_x x)}, \tag{52}$$

where ϕ is an azimuthal coordinate around the ring resonator and x is a coordinate along the waveguide. Time-reversion means $t \to -t$. If we apply this operation on the two modal amplitudes we get

$$\tilde{a}\left(t,\phi\right) = a_{ccw}e^{j\left(-\omega t-\beta_\phi\phi\right)} \equiv a^*_{ccw}e^{j\left(\omega t+\beta_\phi\phi\right)}, \tag{53}$$

$$\tilde{p}\left(t,x\right) = p_{in,1}e^{j(-\omega t-\beta_x x)} \equiv p^*_{in,1}e^{j(\omega t+\beta_x x)}, \tag{54}$$

where we used the fact that the real fields are described by

$$\mathrm{Re}\left(p_{in,1}e^{j(-\omega t-\beta_x x)}\right) = \mathrm{Re}\left(p^*_{in,1}e^{j(\omega t+\beta_x x)}\right). \tag{55}$$

Equations 53 and 54 mean that under time-reversal a counter-clockwise travelling wave becomes a clockwise travelling wave with complex conjugate amplitude and the wave entering the system becomes a wave leaving the system with complex conjugate amplitude as well. For all the other modes in the system analogous conclusions can be drawn and the relations for the amplitudes become

$$\tilde{\mathbf{a}} = \begin{pmatrix} 0 & 1 \\ 1 & 0 \end{pmatrix}\mathbf{a}^* = \mathbf{M}\mathbf{a}^*, \tag{56}$$

$$\tilde{\mathbf{p}}_{in} = \mathbf{p}^*_{out} \tag{57}$$

and

$$\tilde{\mathbf{p}}_{out} = \mathbf{p}^*_{in}. \tag{58}$$

To derive a relation between $\mathbf{K}$ and $\mathbf{D}$, we now look at the time-reversed case of Fig. 25 as depicted in Fig. 26. No power is leaving the system, $\tilde{\mathbf{p}}_{out} = 0$, and the system is fed with exponentially growing waves with the amplitudes $\tilde{\mathbf{p}}_{in} = \mathbf{p}^*_{out}$. Equation 39 then takes the form

$$\frac{\mathrm{d}\tilde{\mathbf{a}}}{\mathrm{d}t} = \mathbf{M}\frac{\mathrm{d}\mathbf{a}^*}{\mathrm{d}t} = j\omega\mathbf{M}\mathbf{a}^* = \left(j\boldsymbol{\Omega} - \boldsymbol{\Gamma}_{cpl}\right)\mathbf{M}\mathbf{a}^* + \mathbf{K}^T\mathbf{p}^*_{out}. \tag{59}$$

The complex frequency ω at that the resonator modes oscillate is forced by $\tilde{\mathbf{p}}_{in} = \mathbf{p}^*_{out}$ and is therefore $\boldsymbol{\Omega} - j\boldsymbol{\Gamma}_{cpl}$. (The frequency matrix $\boldsymbol{\Omega} + j\boldsymbol{\Gamma}_{cpl}$ would be that of waves decaying in time.) Inserting ω into the equation yields

$$2\boldsymbol{\Gamma}_{cpl}\mathbf{M}\mathbf{a}^* = \mathbf{K}^T\mathbf{p}^*_{out} = \mathbf{K}^T\mathbf{D}^*\mathbf{a}^*, \tag{60}$$

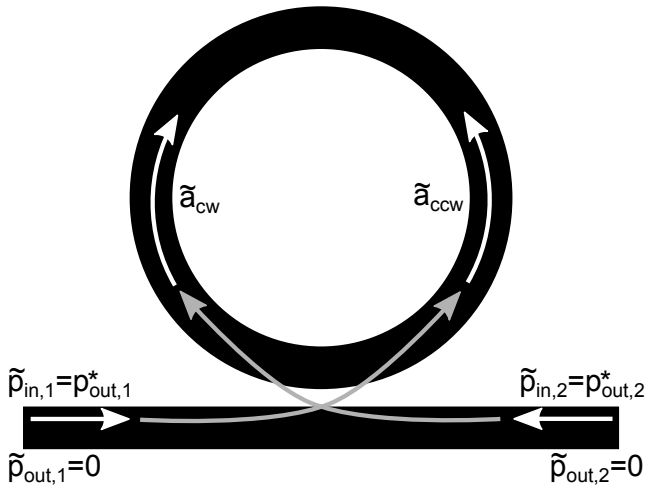

Figure 26: The time-reversed case of Fig. 25. The system is now fed with the exponentially growing waves with the amplitudes $\tilde{\mathbf{p}}_{in} = \mathbf{p}^*_{out}$ and there is no power leaving the resonator $\tilde{\mathbf{p}}_{out} = 0$.

where we used equation 40 in the not time-reversed case with $\mathbf{p}_{in} = 0$. We can conclude that

$$2\mathbf{\Gamma}_{cpl}\mathbf{M} = \mathbf{K}^T\mathbf{D}^*. \tag{61}$$

Since $\mathbf{\Gamma}_{cpl}$ is a diagonal matrix with identical main diagonal entries, the two relations hold true

$$\mathbf{\Gamma}_{cpl}\mathbf{M} = \mathbf{M}\mathbf{\Gamma}_{cpl} \tag{62}$$

and

$$2\mathbf{\Gamma}_{cpl} = 2\mathbf{\Gamma}^T_{cpl} = \mathbf{D}^\dagger\mathbf{D} = \mathbf{D}^T\mathbf{D}^*. \tag{63}$$

We can use the three above equations to derive

$$\left(\mathbf{M}\mathbf{D}^T - \mathbf{K}^T\right)\mathbf{D}^* = 0. \tag{64}$$

We know from equation 46 that $\mathbf{D}$ is a 2×2 matrix of rank 2. Equation 64 is only fulfilled if

$$\mathbf{K} = \mathbf{D}\mathbf{M}. \tag{65}$$

The reasoning that leads this equation is that a matrix product is a projection from the column vectors of one matrix onto the row vectors of the other matrix. If the rank of one matrix is full, meaning its column/row vectors span the full vector space, this projection can simultaneously be zero for all column/row vectors, only if the other matrix vector is the null matrix. An example for such a case would be the projection of a vector in three-dimensional space onto the axis vectors of a Cartesian basis. This projection can only be zero for all three axis vectors if that vector is the null vector.

Equation 65 is unique to travelling ring resonator modes because they undergo an exchange upon time-reversal. It is also possible to describe the two ring resonator modes as standing wave patterns. In

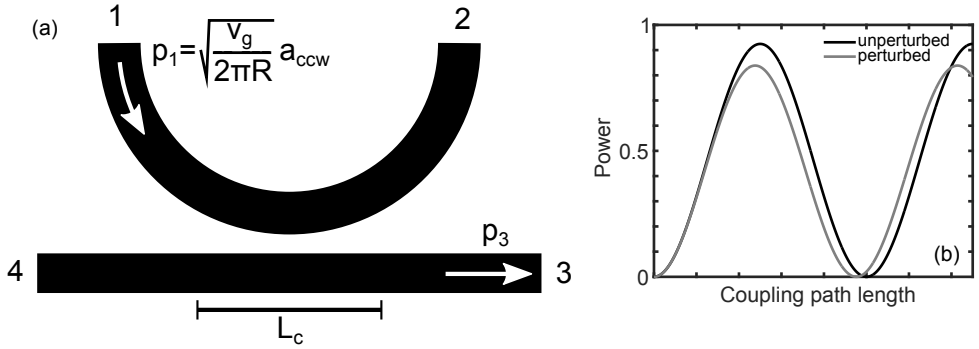

Figure 27: (a) Coupling between ring resonator and waveguide. (b) Fraction of the power transmitted from ring resonator to wavegeuide as a function of the coupling length. The cases for an unperturbed and a perturbed $\Delta\beta$ are shown. For a small coupling length their difference is negligible.

this basis the relation would just be $\mathbf{K} = \mathbf{D}$. But the coupling is more complex because each standing wave couples to waveguide modes travelling in both directions.

The final relation can be obtained from investigation of equation 40 for the time-reversed case. We get

$$0 = \mathbf{C}\mathbf{p}^*_{out} + \mathbf{D}\mathbf{M}\mathbf{a}^* = \mathbf{C}\mathbf{D}^*\mathbf{a}^* + \mathbf{D}\mathbf{M}\mathbf{a}^*, \tag{66}$$

from which follows that

$$\mathbf{C}\mathbf{D}^* = -\mathbf{D}\mathbf{M}. \tag{67}$$

With our choice of real coupling parameters we can conclude

$$\mathbf{C} = \begin{pmatrix} 0 & -1 \\ -1 & 0 \end{pmatrix}. \tag{68}$$

With this we have greatly simplified the equations 39 and 40. We can describe the system's behaviour with only two parameters, the resonance frequency and the damping rate.

To have a usable model we now need to include two more effects: intrinsic resonator losses like radiation or absorption and the magneto-optical frequency splitting. If the intrinsic losses are small ($\omega_0 \gg \gamma_i$), we can neglect the effect it has on the coupling loss and the coupling parameters and just extend the decay matrix to $\mathbf{\Gamma} = \mathbf{\Gamma}_{cpl} + \mathbf{\Gamma}_i$ [16, 113]. This is the same argument that we used when we assumed the resonance frequency to be independent of the loss rate. Both, the effect of $\mathbf{\Gamma}_i$ on the coupling parameters as well as the effect of the total losses, $\mathbf{\Gamma}$, on the resonance frequency are second-order corrections which we neglect here [16].

In the general case, the frequency splitting will as well cause only higher-order corrections of the coupling parameters. However, in certain arrangements these corrections cannot be neglected. Fig. 27a shows the coupling section of a ring resonator. We want to know

whether the magneto-optical phase shift strongly alters the fraction of the power that is coupled from the ring resonator to the waveguide. The power in the ring is related to the resonator energy by

$$|p_1|^2 = \frac{v_g}{2\pi R}|a_{ccw}|^2, \tag{69}$$

where v_g is the group velocity of the mode and R is the ring radius [16]. We simplify the problem by assuming that the coupling strength is constant over the length of the coupling section. This is obviously not true for the case in Fig. 27a but the conclusion we will draw from this simplified case will also be valid for the general case. If we further assume that the two waveguides are only weakly coupled, the transmission becomes [16, 103]

$$T_{31} = \frac{|p_3|}{|p_1|} = \frac{\kappa}{\sqrt{\kappa^2 + \Delta\beta_{WG}^2 + \delta\beta^2}} \sin\left(\sqrt{\kappa^2 + \Delta\beta_{WG}^2 + \delta\beta^2}L_c\right), \tag{70}$$

where κ is the coupling constant between the two waveguides, $\Delta\beta_{WG}$ is the difference in propagation constants due to geometry, $\delta\beta$ is the difference due to the magneto-optical phase shift and L_c is the length of the coupling section. Using equation 69, the transmission coefficient, T_{31}, can be related to the coupling rate between waveguide and resonator, d, by

$$d = \sqrt{\frac{v_g}{2\pi R}}T_{31}. \tag{71}$$

We want to argue now that the change in T_{31} induced by the magneto-optical phase shift is negligible. As a first step we argue that T_{31} is a small number. As an example we take the ring resonator described in [106]. It is a ring of 1.465 µm radius that is resonant at a wavelength of 1.55 µm with an intrinsic quality factor of 10^4, and features two modes with a group velocity of $v_g = c_0/4$ and a magneto-optical frequency splitting of 30 GHz. From equations 49 and 71, we know that $T_{31} = \sqrt{\frac{4\pi R\gamma_{cpl}}{v_g}}$ and with $\gamma_{cpl} = \frac{\pi c_0}{\lambda_0 Q_{cpl}}$ [113] we get

$$T_{31} = \sqrt{\frac{4\pi^2 R c_0}{v_g \lambda_0 Q_{cpl}}}, \tag{72}$$

where c_0 is the speed of light, λ_0 is the vacuum wavelength, Q_{cpl} is the coupling quality factor. Using the parameters of the example we get $T_{31} \approx 1.22 \times 10^{-1}$. As a next step we estimate κ. For small T_{31}, equation 70 can be simplified to $T_{31} \approx \kappa L_c$. If we assume a coupling length of 2 µm, we get $\kappa = 6.1 \times 10^4\,\mathrm{m}^{-1}$. As a final step we want to estimate the magnitude of the magneto-optical phase shift from the magneto-optical frequency splitting. The magneto-optical perturbation alters the dispersion and thus shifts the resonance frequency as shown in Fig. 28. If the ring resonator is at resonance its

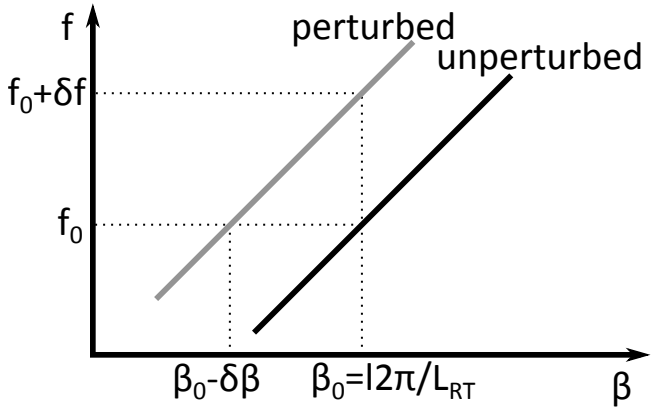

Figure 28: Change in dispersion due to a magneto-optical perturbation.

phase gain for one round trip is an integer multiple of 2π, from which follows that $\beta_0 = l2\pi/L_{RT}$ with β_0 being the propagation constant, L_{RT} is the ring's circumference, and l is the mode order of the resonance. Since this condition must also be fulfilled for the perturbed state, the resonance frequency in order to compensate for the change in β, must change as indicated by the vertical line in Fig. 28. From this frequency shift we want to derive how much the magneto-optical perturbation changes the propagation constant for a given frequency (horizontal line in Fig. 28). We make use of the fact that the resonance frequency is orders of magnitude larger than the change in resonance frequency, i.e. $f_0 = 193.4\,\mathrm{THz}$ compared to $\delta f = 15\,\mathrm{GHz}$. For this minute change the slope of the dispersion curve changes negligibly and we can model the change close to the resonance frequency as a translation of a linear curve. Thus we can relate $\delta\beta$ and δf by

$$2\pi\delta f = \frac{\partial\omega}{\partial\beta}\delta\beta. \tag{73}$$

With $\frac{\partial\omega}{\partial\beta}$ being the group velocity which we established to be $v_g = c_0/4$ for the given example and $\Delta f = 2\delta f = 30\,\mathrm{GHz}$, we obtain $\delta\beta = 2\pi\frac{\delta f}{v_g} = 314\,\mathrm{m}^{-1}$. Accordingly, $\delta\beta$ is more than an order of magnitude smaller than κ. We neglected here the term $\Delta\beta_{WG}^2$ but this will only increase the discrepancy between the unperturbed argument in the sine function of equation 70 and the small perturbation of $\delta\beta$. Since we have established now that $\delta\beta$ is a small correction to equation 70,

we will now expand it into a Taylor series using $\delta\beta$ as the argument. This yields

$$T_{31} = \frac{\kappa \sin\left(\sqrt{\kappa^2 + \Delta\beta_{WG}^2} L_c\right)}{\sqrt{\kappa^2 + \Delta\beta_{WG}^2}} + \frac{1}{2}\left(\frac{\kappa L \cos\left(\sqrt{\kappa^2 + \Delta\beta_{WG}^2} L\right)}{\kappa^2 + \Delta\beta_{WG}^2} - \frac{\sin\left(\sqrt{\kappa^2 + \Delta\beta_{WG}^2} L_c\right)}{\left(\kappa^2 + \Delta\beta_{WG}^2\right)^{\frac{3}{2}}}\right)\delta\beta^2 + \ldots \quad (74)$$

From the Taylor series expansion follows that $\delta\beta$ is indeed a second-order correction which can be neglected. This can be seen in Fig. 27b as well. For short lengths the transmitted power is identical for the unperturbed and the perturbed case. In this derivation we implied that the coupling length is as short as possible to achieve the needed transmission coefficient, T_{31}. However, due to the sinusoidal nature of the coupling term it is also possible to achieve the same coupling coefficient with longer lengths. In such a case, the higher-order terms in equation 74 are not negligible anymore and likewise the influence of $\delta\beta$ on the coupling parameters. Hence, the perturbed and unperturbed curves diverge in Fig. 27b for longer coupling lengths. This means the coupling becomes nonreciprocal and equations 49 and 65 lose their validity. Due to the compactness of ring resonators, the coupling length is minimal in most cases. Nonetheless, for resonators with long coupling sections such as race track resonators care should be taken that this condition is really fulfilled.

We can now extend equation 39 with resonator losses and magneto-optical frequency splitting and get for a harmonic time-dependence, $e^{j\omega t}$, the following equations:

$$j\omega \begin{pmatrix} a_{cw} \\ a_{ccw} \end{pmatrix} = \begin{pmatrix} j(\omega_0+\delta\omega) - (\gamma_{cpl}+\gamma_i) & 0 \\ 0 & j(\omega_0-\delta\omega) - (\gamma_{cpl}+\gamma_i) \end{pmatrix} \begin{pmatrix} a_{cw} \\ a_{ccw} \end{pmatrix} + \begin{pmatrix} 0 & \sqrt{2\gamma_{cpl}} \\ \sqrt{2\gamma_{cpl}} & 0 \end{pmatrix} \begin{pmatrix} p_{in,1} \\ p_{in,2} \end{pmatrix} \quad (75)$$

and

$$\begin{pmatrix} p_{out,1} \\ p_{out,2} \end{pmatrix} = \begin{pmatrix} 0 & -1 \\ -1 & 0 \end{pmatrix} \begin{pmatrix} p_{in,1} \\ p_{in,2} \end{pmatrix} + \begin{pmatrix} \sqrt{2\gamma_{cpl}} & 0 \\ 0 & \sqrt{2\gamma_{cpl}} \end{pmatrix} \begin{pmatrix} a_{cw} \\ a_{ccw} \end{pmatrix}. \quad (76)$$

2.14.2.2 *Ring resonator as an isolator*

We can solve equations 75 and 76 for $p_{in,2} = 0$ and obtain the following transmission coefficient:

$$T_{21}(\omega) = \frac{p_{out,2}}{p_{in,1}} = \frac{2\gamma_{cpl}}{j(\omega - \omega_0 + \delta\omega) + \gamma_{cpl} + \gamma_i} - 1. \quad (77)$$

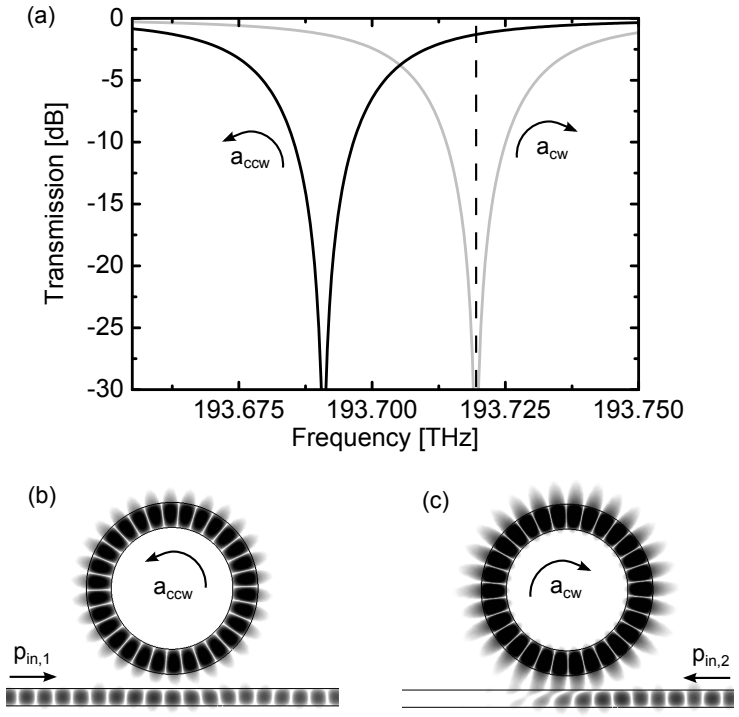

Figure 29: (a) Transmission spectrum of a magneto-optically active ring resonator. For an excitation from the left the counter-clockwise travelling mode is excited; an excitation from the right gives rise to the clockwise travelling mode. (b) H-field for excitation from the left with 193.72 THz. (c) H-field for excitaion from the right with 193.72 THz. Details on the ring resonator can be found in [106].

Likewise, for the case when $p_{in,1} = 0$ we get

$$T_{12}(\omega) = \frac{p_{out,1}}{p_{in,2}} = \frac{2\gamma_{cpl}}{j(\omega - \omega_0 - \delta\omega) + \gamma_{cpl} + \gamma_i} - 1. \tag{78}$$

Both transmission coefficients are nearly identical except for the sign of $\delta\omega$. Accordingly, their resonances are divided by $\Delta\omega = 2\delta\omega$. If we investigate the two equations at resonance, $\omega = \omega_0 \mp \delta\omega$, we see that for

$$\gamma_{cpl} = \gamma_i \tag{79}$$

the transmission is zero. This condition is referred to as critical coupling [115]. If this condition is fulfilled the part of the light that is coupled back from the ring resonator to the waveguide and the part of the light that passes directly through the waveguide interfere destructively and thus the resonator radiates all the light guided in the adjacent waveguide. The fact that the resonance frequency is distinct for both resonator modes can be exploited for isolation as shown in Fig. 29. At the resonance of the clockwise travelling mode a wave coming from the left will be transmitted whereas a wave coming from the right will be radiated in the ring resonator. From this it also becomes clear that resonance width, the FWHM, must be smaller than

the frequency splitting Δf as discussed in Fig. 22. If in the example in Fig. 29 the counter-clockwise resonance width would be much larger than Δf, the device would still function as an isolator but with intolerably high insertion loss for the pass direction from left to right.

2.15 CHAPTER SUMMARY

- Isolators and circulators can be built only from devices that break Lorentz reciprocity and thus must have an asymmetric scattering matrix.
- It is not sufficient to find a state where power can be transmitted from one side to the other one and another state where the power is not transmitted in the reverse direction. For a device to be an isolator it must block or divert all the possible states for backward propagation.
- Faraday rotation can be described as the superposition of a left-handed and a right-handed circularly polarized wave with differing propagation constants.
- Integrated waveguides show very weak Faraday rotation due to their form birefringence.
- To see a magneto-optical phase shift the waveguide profile must be asymmetric with respect to the plane spun by the bias magnetic field vector and wave propagation vector.
- A magneto-optical phase shift inside a ring resonator causes frequency splitting of the clockwise and the counter-clockwise travelling mode.
- To achieve TE mode frequency splitting through the ring's curvature, a large index contrast between waveguide core and magneto-optical cladding is needed.
- Temporal coupled-mode theory is a handy tool to derive the transmission parameters of resonators weakly coupled to waveguides.
- The magneto-optical frequency splitting makes ring resonators usable as isolators because energy will be resonantly scattered in the ring only for one direction of propagation.
- A functioning magneto-optically active cladding for TE mode frequency splitting in ring resonators has not yet been demonstrated.

Reciprocity in daily life III:
Nonreciprocal attraction

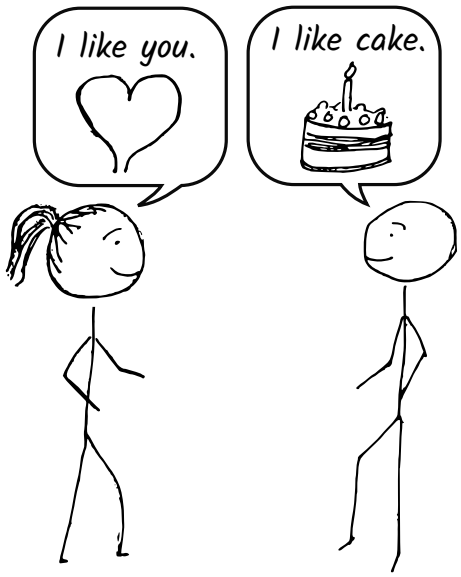

3

MAGNETO-OPTICAL RING RESONATORS WITH COUPLED MODES

Ring resonators with simultaneous coupling of the counterpropagating modes and magneto-optical frequency splitting are investigated. It is shown that in these systems the magnetic biasing field can suppress the ring's resonance and reduce backscattering.

Contents

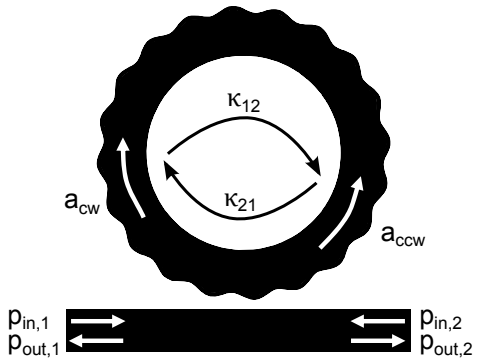

Figure 30: Schematic of a ring resonator with sinusoidal corrugation. The corrugation couples the clockwise and the counter-clockwise travelling wave. The resonator is coupled to an access waveguide.

3.1 INTRODUCTION

In the previous chapter we have shown that the magneto-optical phase shift can cause resonance splitting between the clockwise and counter-clockwise running mode. In this chapter we will investigate systems which feature a competing mechanism that couples the modes. This coupling is usually an undesired effect due to sidewall roughness of the waveguide and is especially prevalent for high quality factor ring resonators [116]. Such devices feature strong backscattering. We show that the magneto-optical frequency splitting can suppress this backscattering. Further, we demonstrate that the coupling of the two resonator modes and the magneto-optical frequency splitting can be engineered in such a way that a magnetic biasing field can suppress the device resonance.

3.2 THEORY

3.2.1 *Corrugated magneto-optical ring resonator*

We start by considering a ring resonator with currugated sidewalls with no magnetic biasing field applied. The configuration is shown in Fig. 30. An incoming wave $p_{in,1}$ will excite a counter-clockwise travelling wave with the amplitude a_{ccw} in the ring resonator. Due to a sidewall corrugation of the resonator, this counter-clockwise travelling wave will be backscattered to give rise to a clockwise travelling wave with amplitude a_{cw}. In this case the coupled-mode equations 75 and 76 need to be extended to account for the additional coupling

between the two resonator modes [117]. For harmonic dependence the coupled-mode equations become

$$\frac{\mathrm{d}}{\mathrm{d}t}\begin{pmatrix} a_{cw} \\ a_{ccw} \end{pmatrix} = \begin{pmatrix} j(\omega_{cw}) - (\gamma_{cpl}+\gamma_i) & \kappa_{12} \\ \kappa_{21} & j(\omega_{ccw}) - (\gamma_{cpl}+\gamma_i) \end{pmatrix} \begin{pmatrix} a_{cw} \\ a_{ccw} \end{pmatrix} + \begin{pmatrix} 0 & \sqrt{2\gamma_{cpl}} \\ \sqrt{2\gamma_{cpl}} & 0 \end{pmatrix} \begin{pmatrix} p_{in,1} \\ p_{in,2} \end{pmatrix} \quad (80)$$

and

$$\begin{pmatrix} p_{out,1} \\ p_{out,2} \end{pmatrix} = \begin{pmatrix} 0 & -1 \\ -1 & 0 \end{pmatrix} \begin{pmatrix} p_{in,1} \\ p_{in,2} \end{pmatrix} + \begin{pmatrix} \sqrt{2\gamma_{cpl}} & 0 \\ 0 & \sqrt{2\gamma_{cpl}} \end{pmatrix} \begin{pmatrix} a_{cw} \\ a_{ccw} \end{pmatrix}. \quad (81)$$

We can derive the relationship between κ_{12} and κ_{21} in the same way we derived equation 49. We inspect equation 80 for the case of a lossless and uncoupled resonator. The equation system becomes in this case

$$\frac{\mathrm{d}}{\mathrm{d}t}\begin{pmatrix} a_{cw} \\ a_{ccw} \end{pmatrix} = \begin{pmatrix} j\omega_{cw} & \kappa_{12} \\ \kappa_{21} & j\omega_{ccw} \end{pmatrix} \begin{pmatrix} a_{cw} \\ a_{ccw} \end{pmatrix}. \quad (82)$$

Because there is no channel for the energy to decay, its change over time must vanish [16]. With the help of equation 82 one can rewrite the energy decay

$$\begin{aligned} \frac{\mathrm{d}}{\mathrm{d}t}\left(|a_{cw}|^2 + |a_{ccw}|^2\right) &= a_{cw}^* \frac{\mathrm{d}a_{cw}}{\mathrm{d}t} + \frac{\mathrm{d}a_{cw}^*}{\mathrm{d}t} a_{cw} + a_{ccw}^* \frac{\mathrm{d}a_{ccw}}{\mathrm{d}t} + \frac{\mathrm{d}a_{ccw}^*}{\mathrm{d}t} a_{ccw} \\ &= a_{cw}^* \kappa_{12} a_{ccw} + a_{cw} \kappa_{12}^* a_{ccw}^* + a_{ccw}^* \kappa_{21} a_{cw} + a_{ccw} \kappa_{21}^* a_{cw}^* \\ &= a_{cw}^* \left(\kappa_{12} + \kappa_{21}^*\right) a_{ccw} + a_{cw} \left(\kappa_{12}^* + \kappa_{21}\right) a_{ccw}^* \\ &= 0. \end{aligned} \quad (83)$$

As the modal amplitudes can be arbitrary, the only way to fulfil equation 83 is if

$$\kappa_{12} + \kappa_{21}^* = 0. \quad (84)$$

From this follows that both coupling coefficients must have the same amplitude. Their phases are connected but not uniquely defined because the phase relation between the counter-clockwise and the clockwise travelling mode can be chosen arbitrarily. Here, we chose the relation such that $\kappa_{12} = \kappa_{21} = -ju$, where u is a real number.

To illustrate the interplay between the coupling of the two modes and the magneto-optical frequency splitting, we examine the solution of equation 82. The equation system is identical to that of two coupled resonators with different resonance frequencies [16]. Further, it is the time equivalent to the spatial coupling of two modes as discussed in Fig. 15. If we assume that $a_{cw}(t=0) = a_0$ and $a_{ccw}(t=0) = 0$, the solution becomes [16]

$$a_{cw}(t) = a_0 \left(\cos(\Omega_0 t) - j\frac{\omega_{ccw} - \omega_{cw}}{2\Omega_0} \sin(\Omega_0 t)\right) e^{j\frac{\omega_{ccw}+\omega_{cw}}{2}t} \quad (85)$$

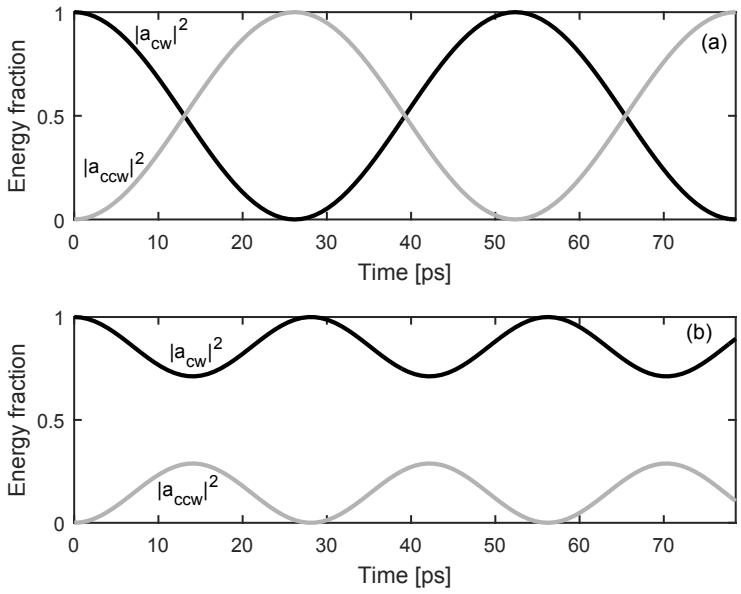

Figure 31: Coupling between two modes. In (a) $\omega_{cw} = \omega_{ccw}$ and $u = 6 \times 10^{10}\,1/\mathrm{s}$. In (b) the same u was used but the frequency splitting is now $\omega_{cw} - \omega_{ccw} = 2\pi \times 30\,\mathrm{GHz}$.

and

$$a_{ccw}(t) = a_0 \frac{-ju}{\Omega_0} \sin(\Omega_0 t)\, e^{j\frac{\omega_{ccw}+\omega_{cw}}{2}t}, \tag{86}$$

where $\Omega_0 = \sqrt{\left(\frac{\omega_{cw}-\omega_{ccw}}{2}\right)^2 + u^2}$. In complete analogy to equation 33, which is the maximum power fraction that could be coupled from one mode to the other, we are able to define here the maximum energy fraction that can be coupled from one mode to the other:

$$\eta_a = \frac{|a_{ccw}|^2\Big|_{max}}{|a_{cw}|^2\Big|_{max}} = \frac{u}{\left(\frac{\omega_{cw}-\omega_{ccw}}{2}\right)^2 + u^2}. \tag{87}$$

This ratio is examplified in Fig. 31. The first part of the figure depicts the energy exchange over time when both modes have the same frequency. In this case the modes completely exchange their energy. In the second part there is frequency splitting and the modes can only transfer part of their energy from one to the other. Thus, in this chapter we utilize the fact that a strong frequency splitting suppresses the coupling between modes.

3.2.2 *Transmission and reflection coefficients*

Now that we have investigated the uncoupled system, we will focus on the resonator coupled to a waveguide. In contrast to the uncoupled resonator which oscillated at its eigenfrequencies, the system is now forced to oscillate at the frequency of the excitation from

the waveguide such that we can determine the frequency dependent transmission and reflection parameters. If the waveguide is only excited from the right and no wave is impinging from the left, i. e. $p_{in,2} = 0$, we obtain for the frequency-dependent transmission

The transmission coefficient in [117] differs slightly because another phase relation between waveguide and resonator mode was used (see equation 50).

$$T_{21}(\omega) = \frac{p_{out,2}}{p_{in,1}} = \frac{2\gamma_{cpl}B - AB - u^2}{AB + u^2}, \tag{88}$$

where $A = j(\omega - \omega_{ccw}) + \gamma_{cpl} + \gamma_i$ and $B = j(\omega - \omega_{cw}) + \gamma_{cpl} + \gamma_i$. For the reflection spectrum we obtain:

$$R_{11}(\omega) = \frac{p_{out,1}}{p_{in,1}} = \frac{-ju2\gamma_{cpl}}{AB + u^2}. \tag{89}$$

The squared reflection spectrum has three extrema:

$$\omega_1 = \frac{\omega_{cw} + \omega_{ccw}}{2} \tag{90}$$

and

$$\omega_{2,3} = \frac{\omega_{cw} + \omega_{ccw}}{2} \pm \sqrt{\left(\frac{\omega_{cw} - \omega_{ccw}}{2}\right)^2 + u^2 - \left(\gamma_{cpl} + \gamma_i\right)^2}. \tag{91}$$

The three frequencies show the spectral variety that can be achieved with this system. If $\left(\frac{\omega_{cw}-\omega_{ccw}}{2}\right)^2 + u^2 > \left(\gamma_{cpl} + \gamma_i\right)^2$, the reflection spectrum will have two maxima at ω_2 and ω_3 and a local minimum at ω_1. If however $\left(\frac{\omega_{cw}-\omega_{ccw}}{2}\right)^2 + u^2 < \left(\gamma_{cpl} + \gamma_i\right)^2$, ω_2 and ω_3 become complex and there is a single maximum at ω_1. This means that both the magneto-optical effect and the coupling of both resonator modes lift the degeneracy of the system. The former through frequency splitting and the latter through forming supermodes. For $u = 0$ the resonances should be equal to ω_{cw} and ω_{ccw}. The reason equation 91 does not converge to these values is that R_{11} is zero for all frequencies in this case so that equation 91 becomes meaningless.

3.2.3 *Critical coupling condition for corrugated ring resonators*

We will now first investigate the case without magneto-optical frequency splitting ($\omega_0 = \omega_{cw} = \omega_{ccw}$). In [117] it was shown that there is no transmission at resonance ($\omega = \omega_0$) if the following condition is fulfilled:

$$u^2 + \gamma_i^2 = \gamma_{cpl}^2. \tag{92}$$

If we compare the critical coupling condition of a smooth ring resonator ($\gamma_{cpl} = \gamma_i$) to that of a corrugated one, we see that the coupling for the latter case not only needs to be balanced with the resonator

losses but additionally with what is coupled over to the second mode. Thus, there is a remaining reflection at resonance of

$$R_{11}(\omega_0) = \frac{p_{out,1}}{p_{in,1}} = \frac{-ju\sqrt{u^2+\gamma_i^2}}{\gamma_i^2+u^2+\gamma_i\sqrt{u^2+\gamma_i^2}}. \tag{93}$$

For large intrinsic quality factors, i. e. low intrinsic loss rates γ_i, the reflection coefficient approaches unity. This is the reason why backscattering is more of an issue the higher the ring's quality factor.

If a magnetic field is applied, the degeneracy between the two resonator modes is lifted, i.e. $\omega_{cw} \neq \omega_{ccw}$. It follows for the transmission at ω_{ccw}:

$$T_{21}(\omega_{ccw}) = \frac{\gamma_{cpl}^2-\gamma_i^2+j(\omega_{ccw}-\omega_{cw})(\gamma_{cpl}-\gamma_i)-u^2}{(\gamma_{cpl}+\gamma_i)^2+j(\omega_{ccw}-\omega_{cw})(\gamma_{cpl}+\gamma_i)+u^2}. \tag{94}$$

The reflection in this case becomes

$$R_{11}(\omega_{ccw}) = \frac{-ju2\gamma_{cpl}}{(\gamma_{cpl}+\gamma_i)^2+j(\omega_{ccw}-\omega_{cw})(\gamma_{cpl}+\gamma_i)+u^2}. \tag{95}$$

We can see from equation 91 that $R_{11}(\omega)$ does not exactly have a maximum for ω_{ccw}. We use here ω_{ccw} because it keeps equation 94 and 95 lucid and we are mainly interested in cases for which applies $\left(\frac{\omega_{cw}-\omega_{ccw}}{2}\right)^2 > (\gamma_{cpl}+\gamma_i)^2 - u^2$ and ω_{ccw} is a good approximation for position of the maximum of $R_{11}(\omega)$.

For a perfectly circular ring resonator with no corrugation the clockwise and counter-clockwise waves are decoupled and u is zero. In that case the real and imaginary part of the numerator of equation 94 are zero for $\gamma_{cpl} = \gamma_i$. This means that the transmission at the counter-clockwise resonance would be always zero independently of the frequency splitting $\Delta\omega = \omega_{cw} - \omega_{ccw}$.

3.3 BACKSCATTERING SUPPRESSION IN RING RESONATORS

The production process of silicon photonic ring resonators will unavoidably leave the resonator's sidewall slightly corrugated. This will cause weak backscattering. By weak we mean that the coupling rate between the resonator modes is small compared to the intrinsic resonator loss rate and the coupling rate to the waveguide ($u < \gamma_i + \gamma_{cpl}$). We have already seen from equation 93 that the closer u gets to the resonator loss rate the stronger the backscattering gets. To obtain a realistic value for u, we start by investigating the power that is reflected back due to sidewall roughness. The backscattered power in a rough waveguide relates to the input power and the waveguide length according to $P_{bsc} = \left(1 - e^{-\alpha_{bsc}L}\right) P_0$. Since the ring resonator track length

($L = 2\pi R$) is much smaller than the backscattering length $1/\alpha_{bsc}$, one can simplify the relation to $P_{bsc} = \alpha_{bsc} L P_0$. The coupling rate u is half the ratio of the backscattered power, P_{bsc}, and the energy in the original mode, E_o:

The expression for u follows from the definition of the quality factor: $Q_u = \omega \frac{\text{max energy}}{\text{power coupled}} = \frac{\omega}{2u}$.

$$u = \frac{1}{2}\frac{P_{bsc}}{E_o} = \frac{1}{2}\frac{\alpha_{bsc} L P_0}{E_o} = \frac{1}{2}\alpha_{bsc} v_g, \tag{96}$$

where we used $P_0 = \frac{v_g}{L} E_0$. The factor one half is due to the fact that u is the decay rate of the amplitude which is half that of the energy. For waveguides with widths ranging from 450 nm to 500 nm and a height of 220 nm, Refs. [118] and [119] found α_{bsc} ranging from $8\,\mathrm{m}^{-1}$ down to $3.9\,\mathrm{m}^{-1}$. If we assume $\alpha_{bsc} = 6\,\mathrm{m}^{-1}$ and as for the ring in the previous chapter $v_g = c_0/4$, we obtain an $u = 4.5 \times 10^8\,\mathrm{s}^{-1}$. For comparison an intrinsic quality factor of $Q_i = 10^4$ at a frequency of $f_0 = 193.7\,\mathrm{THz}$ corresponds to a loss rate of $\gamma_i = \frac{\pi f_o}{Q_i} = 6.1 \times 10^{10}\,\mathrm{s}^{-1}$. In equation 93 we calculated the reflection at resonance of a critically coupled resonator. With the additional condition of $u \ll \gamma_i$, the power reflection coefficient can be calculated by

$$\left| R_{11}(\omega_0) \right|^2 = \left(\frac{u}{2\gamma_i} \right)^2. \tag{97}$$

If now the magneto-optical effect lifts the degeneracy of the two modes, we can conclude from equation 95 that the reflected power at resonance reduces according to

$$\left| R_{11}(\omega_{ccw}) \right|^2 = \frac{u^2}{(2\gamma_i)^2 + (\omega_{ccw} - \omega_{cw})^2}. \tag{98}$$

To achieve an appreciable reflection reduction, $\omega_{ccw} - \omega_{cw}$ should be larger than $2\gamma_i = \gamma_{cpl} + \gamma_i$. Since the total decay rate of the resonator is related to the full width at half maximum of the power spectrum by $\gamma_{cpl} + \gamma_i = \frac{1}{2}\Delta\omega_{FWHM}$, the condition can be rewritten to $\omega_{ccw} - \omega_{cw} > \frac{1}{2}\Delta\omega_{FWHM}$. This means the clockwise and the counterclockwise resonance need to have as little spectral overlap as possible.

Fig. 32 shows two examples for the suppression of backscattering. The first part shows the transmission and reflection of a resonator with an intrinsic quality factor of $Q_i = 10^4$ and the second part shows these spectra of a resonator with $Q_i = 10^6$. For this figure as well as for the following figures an unperturbed resonance frequency of $f_0 = \omega_0/(2\pi) = 193.7\,\mathrm{THz}$ is assumed. The quality factor and the resonance frequency result in an intrinsic loss rate of $\gamma_i = 6.1 \times 10^{10}\,\mathrm{s}^{-1}$ and $\gamma_i = 6.1 \times 10^8\,\mathrm{s}^{-1}$, respectively. The coupling rate between the two modes u is $4.5 \times 10^8\,\mathrm{s}^{-1}$ and we adjusted γ_{cpl} according to the modified condition for critical coupling, equation 92. For the ring with the lower Q_i, the loss rate is much larger than the coupling rate ($\gamma_i + \gamma_{cpl} \gg u$). In accordance with equation 97 the reflection starts

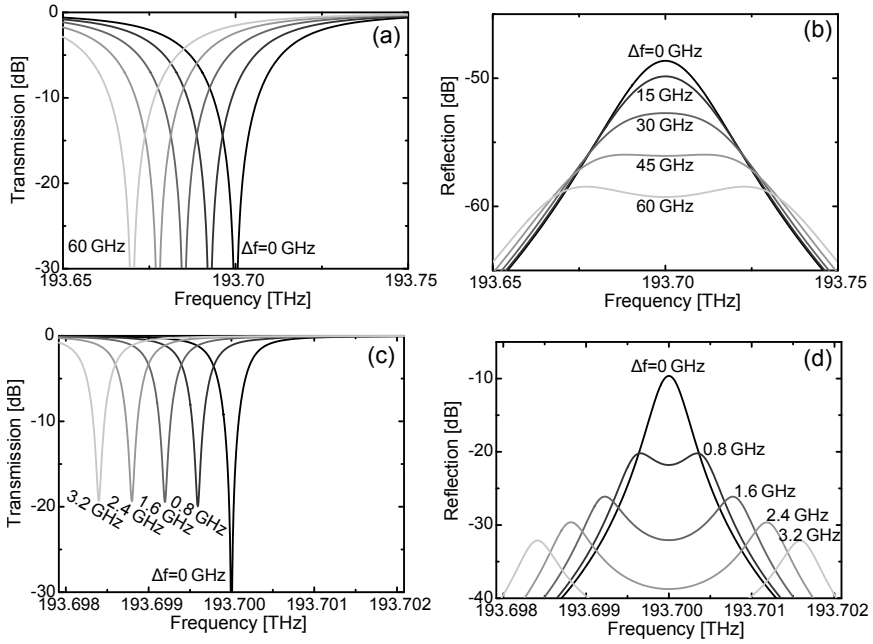

Figure 32: Backscattering suppression. (a) and (b) show the spectra for a resonator with $Q_i = 10^4$ and a magneto-optical frequency splitting varied from 0 GHz to 60 GHz. (c) and (d) show the spectra for a resonator with $Q_i = 10^6$ and a frequency splitting varied from 0 GHz to 3.2 GHz. In both cases $u = 4.5 \times 10^8\,\mathrm{s}^{-1}$ and $\gamma_{cpl}^2 = u^2 + \gamma_i^2$ holds.

already at a very low level and a significant further reduction is only possible if the frequency splitting becomes larger than the full width at half maximum of the unperturbed resonance which is in this case $\Delta f_{FWHM} = 19.4\,\mathrm{GHz}$. On the other hand, the ring with the higher Q_i features a significant back-reflection because u is of the same order as γ_i in this case. A frequency splitting of a few gigahertz can strongly reduce the backscattering. Albeit this comes at the price that the extinction of the transmission is now limited to $-20\,\mathrm{dB}$. This effect will be discussed in detail in the next section.

In this small case study we only considered backscattering due to a continuous roughness of the sidewalls. However, there can be spatially localised backscattering in the coupling section or, for non-circular resonators like racetrack resonators, significant backscattering at the transition from the curved to the bend section is possible [119]. In such cases the u can be much larger resulting in a significant resonator reflection, already for intrinsic quality factors of the order of 10^4.

Interestingly, the reflection spectrum is symmetric with respect to f_0 whereas the transmission spectrum is not. The reason for this is that for the reflection the light is coupled from the waveguide to the counter-clockwise travelling ring mode, subsequently in the resonator it is coupled over to the clockwise travelling mode and from there back to the waveguide. In contrast, for the transmission the

waveguide mode excites the counter-clockwise travelling ring mode which is then coupled back to the waveguide. Mathematically this is reflected by the fact that in the reflection spectrum in equation 89 the clockwise and counter-clockwise resonance only occur as a product but the transmission spectrum in equation 88 features a term containing solely the counter-clockwise resonance.

3.4 RESONANCE SUPPRESSION WITH THE MAGNETO-OPTICAL EFFECT

In the previous section we investigated how magneto-optical frequency splitting can suppress unwanted backreflections. In this section we will now engineer the backscattering in such a way that it creates a functionality in combination with the magnetic bias field. Namely, the magnetic field induced suppression of the ring resonator resonance.

For a ring resonator with a corrugation and thus a non-zero coupling rate u, the real part of the numerator of equation 94 is zero if equation 92 is fulfilled. The condition for a zero imaginary part is the same as for the case without corrugation, $\gamma_{cpl} = \gamma_i$. As the conditions for real and imaginary part are conflicting, the transmission cannot be zero for a ring resonator with a corrugated sidewall and magneto-optically splitted resonance modes. (This argument is formally not correct, since ω_{ccw} is only approximately the transmission minimum. The correct argument would be to show that the real and imaginary parts of the numerator in equation 88 do not have coinciding roots if $\omega_{cw} \neq \omega_{ccw}$. This is the case if equation 92 holds.)

This inability to achieve complete transmission extinction can be used for resonance suppression. If no static magnetic field is applied, there will be no magneto-optical frequency splitting. As already mentioned, in such a case the transmission will be zero if equation 92 is satisfied. Applying a magnetic field will give rise to a non-vanishing $\Delta\omega = \omega_{ccw} - \omega_{cw}$. As $\Delta\omega$ grows, the imaginary part of equation 94 increases and the transmission at resonance becomes greater than zero. Inserting equation 92 into equation 94 yields

$$\left| T_{21}\left(\omega_{ccw}\right) \right|^2 = \frac{1}{1 + \left(\frac{\omega_0}{\Delta\omega Q_{cpl}}\right)^2} \left(\frac{\frac{Q_i}{Q_{cpl}} - 1}{\frac{Q_i}{Q_{cpl}} + 1} \right)^2 . \tag{99}$$

We substituted γ_i and γ_{cpl} with $\frac{\omega_0}{2Q_i}$ and $\frac{\omega_0}{2Q_{cpl}}$ because in the following we want to compare systems with different coupling and intrinsic quality factors. From equation 92 and equation 95 the following is obtained for the reflection:

$$\left| R_{11}\left(\omega_{ccw}\right) \right|^2 = \frac{1}{1 + \left(\frac{\Delta\omega Q_{cpl}}{\omega_0}\right)^2} \frac{\frac{Q_i}{Q_{cpl}} - 1}{\frac{Q_i}{Q_{cpl}} + 1}. \tag{100}$$

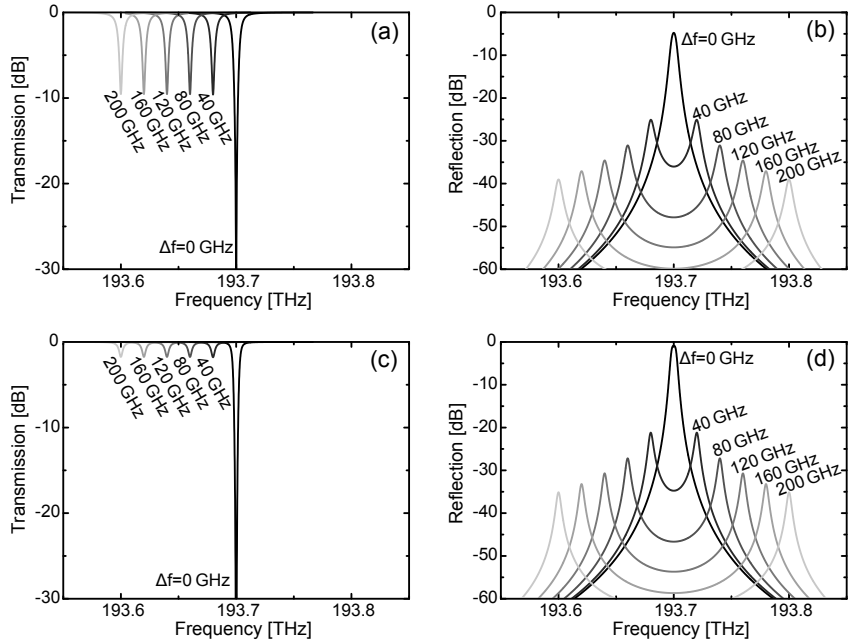

Figure 33: Ring resonators with constant $Q_{cpl} = 5 \times 10^4$. Transmission (a) and reflection (b) for $Q_i = 2\,Q_{cpl} = 10^5$ and various magneto-optical frequency splittings Δf. (c) and (d) show the transmission and reflection for $Q_i = 10\,Q_{cpl} = 5 \times 10^5$.

The transmission T reaches saturation at infinite frequency splitting, which is:

$$\left| T_{21}\left(\omega_{ccw}\right) \right|^2 = \left(\frac{\frac{Q_i}{Q_{cpl}} - 1}{\frac{Q_i}{Q_{cpl}} + 1} \right)^2 . \tag{101}$$

The transmission term can be brought close to one for two cases $Q_{cpl} \gg Q_i$ and $Q_i \gg Q_{cpl}$. The former case is in conflict with equation 92 which can be rewritten in terms of quality factors, $Q_{cpl}^{-2} = \left(\frac{2u}{\omega_0}\right)^2 + Q_i^{-2}$. Thus, only if the intrinsic quality factor is larger than that of the coupling, the resonance can be suppressed. The frequency splitting that is needed to bring the dip to the saturation depends on $(\Delta\omega Q_{cpl})/\omega_0$. The saturation can thus be achieved even for a small frequency splitting $\Delta\omega$ if Q_{cpl} is large (but smaller than Q_i).

To illustrate these dependencies we calculated several curves with reasonable parameters for ring resonators. Fig. 33 shows the change of the transmission and reflection functions with growing frequency splitting for the case of constant $Q_{cpl} = 5 \times 10^4$. Fig. 33a and b show the transmission and reflection for $Q_i = 2\,Q_{cpl}$. Here the transmission dip decreases and reaches saturation at $-10\,\mathrm{dB}$. On the other hand the reflection is continually suppressed which corresponds to the form of equation 100. Fig. 33c and d show the transmission and reflection for $Q_i = 10\,Q_{cpl}$. The transmission dip can now be suppressed to $-3\,dB$. From equation 92 it follows that the coupling rate,

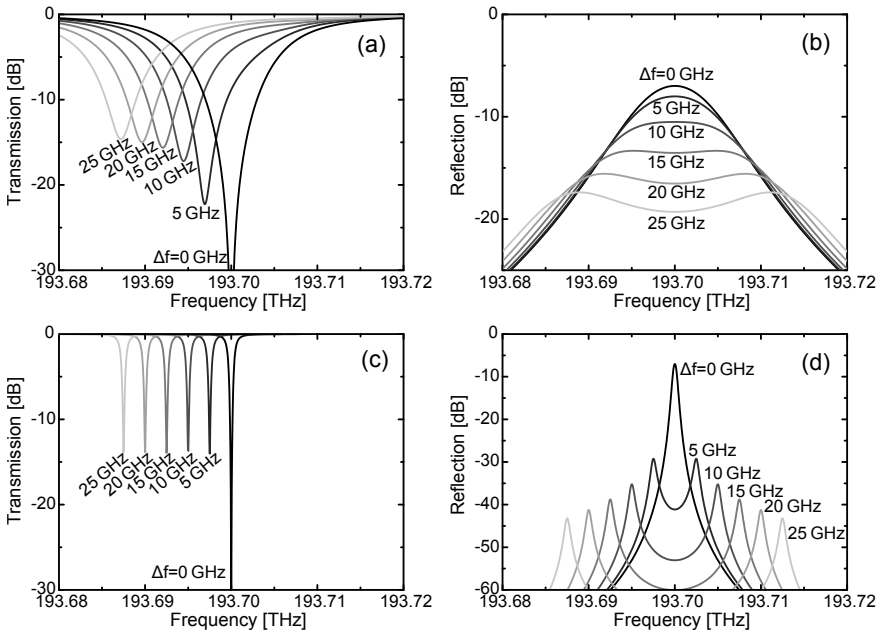

Figure 34: Ring resonators with constant ratio $Q_i = 1.5\,Q_{cpl}$. Transmission (a) and reflection (b) for $Q_{cpl} = 2.5 \times 10^4$ and $Q_i = 1.5\,Q_{cpl} = 3.75 \times 10^4$ and various magneto-optical frequency splittings Δf. (c) and (d) show the transmission and reflection for $Q_{cpl} = 5 \times 10^5$ and $Q_i = 1.5\,Q_{cpl} = 7.5 \times 10^5$.

u, needs to be larger for a larger ratio Q_i/Q_{cpl}. Accordingly, the reflection at zero frequency split is $R = -1\,dB$ and thus is stronger in Fig. 33d as compared to $R = -5\,dB$ in Fig. 33b.

The frequency splitting that is needed to reach the limit of resonance suppression depends on the ratio of $(\Delta\omega Q_{cpl})/\omega_0$. Fig. 34 shows two different arrangements both with a Q_i/Q_{cpl} ratio of 1.5 and thus equal saturation level. Fig. 34a and b show the transmission and reflection for $Q_{cpl} = 2.5 \times 10^4$; Fig. 34c and d for $Q_{cpl} = 5 \times 10^5$. 90% of the saturation limit is reached for the smaller Q_{cpl} in Fig. 34a at $\Delta f = \Delta\omega/(2\pi) = 23\,\mathrm{GHz}$ and for the larger Q_{cpl} in Fig. 34c at $\Delta f = 1.2\,\mathrm{GHz}$.

The demonstrated effect is quite different from the typical ring resonator switch where the resonance is merely shifted in frequency but not eliminated. Switching through resonance shifting can be a problem if wavelength-division-multiplexing channels are used as the switched channel will overlap with the neighbouring channel. Switching off the resonance by means of the application of a magnetic field allows integration of many switches on a single waveguide. By changing the radius of the ring different channels can be addressed and switched on and off simultaneously with the same magnetic field.

3.5 FEM SIMULATIONS

To verify the discussed model, a three dimensional finite element method (FEM) simulation with CST Microwave Studio was carried out. For that we designed a silicon ring resonator with refractive index $n = 3.5$ based on silica substrate $n = 1.43$ and covered by polymer cladding $n = 1.6$. A radius close to 2 µm was chosen to achieve a substantial magneto-optical effect [13]. The radius of the ring resonator was 1.961 µm in order to have its resonance close to 193.7 THz. The height of the ring and access waveguide is 220 nm and the width of the ring waveguide is 500 nm, the width of the access waveguide is 250 nm. The gap between the edges of the ring and access waveguide is 246 nm. Gap width and access waveguide width were chosen such that the coupling is very strong and Q_{cpl} is significantly smaller than Q_i. The outer sidewall of the ring resonator is corrugated by a sinusoidal perturbation $\Delta r = p \sin((2\pi/N)\,\varphi)$, where φ is the azimuthal component in cylindrical coordinates. N was chosen such that periodicity of the perturbation fits the periodicity of the unperturbed resonator mode. Since the magneto-optical perturbation only slightly changes the periodicity, the coupling strength will be insignificantly altered by the fact that N does not exactly match the periodicity of either mode. (This argument is analogous to the one made in section 2.14.2.1 on the change in coupling due to a magneto-optical perturbation) For the given ring N is equal to 40. The amplitude p is set to 0.9 nm such that the critical coupling is achieved with transmission approximately zero for the given geometry and no magneto-optical frequency splitting (see Fig. 35a). The fact, that the periodicities of the perturbation and of the mode are nearly the same, results in a strong coupling between clockwise and counter-clockwise mode already at small amplitudes of Δr. The coupling will be lower for perturbations with a non-matched periodicity or of non-sinusoidal nature (as for example a completely random perturbation). In those cases the amplitude p will have to be larger and that way it will be easier to manufacture. However, a non-matched perturbation will increase scattering losses.

The magneto-optically active material only covers the ring resonator and the coupling section of the waveguide. Accordingly, there are some reflections at the junction between the active medium and the non-active medium. But the effective refractive index $n_{eff} = \sqrt{n^2 \pm g}$ [18] of the magneto-optically active polymer differs less than 1% from the non-magneto-optically active polymer. Thus, the reflections from this junction are expected to be even less than 1% since the electromagnetic field is mainly concentrated in the silicon waveguide. These reflections do not influence the resonance behaviour.

A tetrahedral mesh with linear elements was used with 4 and 5 meshing nodes per wavelength in the material (4 mesh nodes for

0.4 µm for silicon). A PML boundary condition was added. It should be noted that the magneto-optically active material only covers the ring resonator and does not touch the boundaries. The results for a simulation with 4 and 5 mesh cells per wavelength showed a deviation of 0.3% between each other. Thus we consider the results with 4 mesh nodes per wavelength as converged and use this resolution for all the simulations. The amplitude p is approximately 100 times smaller than the average distance between the nodes. But the irregularities on the ring surface vary with a period of several hundred nanometers. Hence, this slowly varying envelope can be resolved even with elements much larger than p.

The quality factors Q_i and Q_e as well as u were obtained by fitting the reflection and transmission curves without magnetic bias. For that the ratio of Q_i and Q_{cpl} as well as the product of Q_{cpl} and u were expressed as a function of maximum reflection and minimum transmission. Then the transmission and reflection curves were fitted to Q_{cpl}. This fitting yielded a $Q_{cpl} = 5.7 \times 10^3$ and a $Q_i = 7.3 \times 10^4$ with a deviation of 1.6×10^{-3}. The actual intrinsic quality factor was simulated separately and is roughly 1.5×10^5. The fitting yields such a low factor because equation 88 does not consider coupling losses which are substantial for such a strong coupling. For further calculations the $Q_i = 7.3 \times 10^4$ was used as ring losses as well as coupling losses need to be considered. Fig. 35a also shows the transmission if the polymer cladding is magneto-optically active with $g = 0.03$ which corresponds to a Faraday rotation of 22000 °/cm. The clockwise and counter-clockwise resonance are then split by 63 GHz and the transmission dip suppressed to −3 dB. The figure shows a curve for the FEM simulation and one curve for the model with the parameters obtained from fitting the curve with no magneto-optical activity. The transmission dips of the FEM simulation and of the model differ by about 0.5 dB which can be explained by reflection and losses in the coupling region not considered in the model. Fig. 35b shows the reflection spectrum with and without magnetic bias. Again model and simulation agree quite well and for the assumed g the reflection can be suppressed to −6 dB. To achieve even stronger reflection suppression and higher transmission at the dip, a stronger magneto-optical effect should be used or resonators with higher quality factors.

In contrast to Figs. 33 and 34 the transmission curve in Fig. 35 shows also a dip at ω_{cw}. This is due to the lower quality factor in this example. Similarly to equation 99 it can be shown that the resonance dip at the clockwise resonance is equal to

$$\left| T_{21}\left(\omega_{cw}\right) \right|^2 = \left(1 + \left(\frac{\omega_0}{\Delta\omega Q_{cpl}} \right)^2 \right)^{-1}. \tag{102}$$

In the curves of Figs. 33 and 34 this dip was strongly suppressed due to higher Q_{cpl}.

An off-diagonal component of the dielectric tensor $g = 0.03$ corresponds to a Verdet constant of $2.2\,10^6\,°/(\mathrm{Tm})$ if a refractive index of 1.6 and a static magnetic field of 1 T is assumed. Such a magnetic field can be generated by two neodymium-iron-boron magnets placed under and on top of the device. A pair of two such magnets could address all devices on one chip. The required Verdet constant is twice as high as what has been published in recent literature [78, 79, 81]. For a Verdet constant of $10^6\,°/(\mathrm{Tm})$ [79] and the magnetic field and polymer refractive index as before, g will be equal to 0.0138 which corresponds to a frequency splitting of 30 GHz. In such a case the resonant dip can be suppressed to only -5.5 dB.

For a larger ring resonator with radius of 3 µm the simulated intrinsic Q-factor will be approximately $Q_i = 40 \times 10^6$. The real Q-factor of the ring resonator will be limited by absorption and scattering losses. The off-diagonal element $g = 0.0138$ produces 20 GHz resonance splitting in a 3 µm ring resonator. If a Q-factor of 10^6 could be achieved then with resonator-waveguide coupling adjusted to $Q_{cpl} = 5 \cdot 10^4$, the transmission dip can be suppressed to -1 dB.

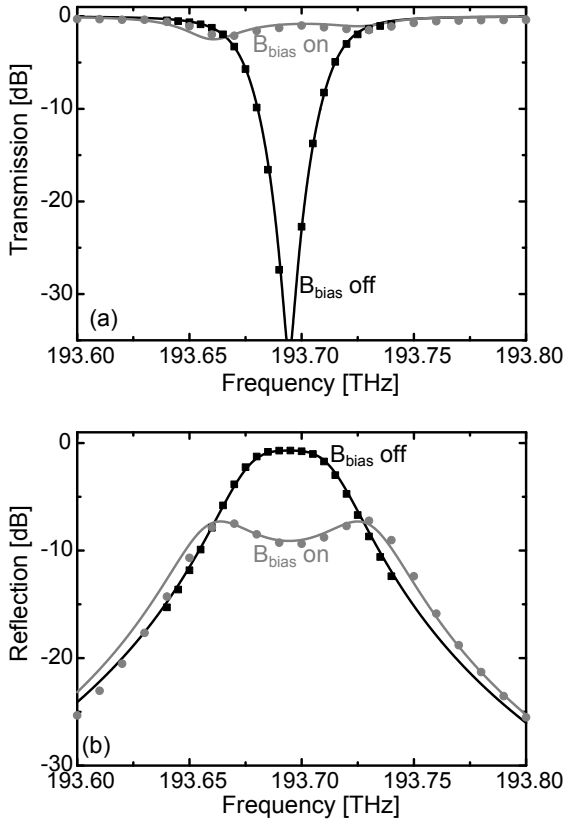

Figure 35: Transmission (a) and reflection (b) spectrum of a resonator with a radius of 1.961 µm. The black squares are the simulation results of the critically coupled resonator without magnetic bias. The black curve is the theoretical fit of that results. The grey dots are the simulation results for $g = 0.03$ which corresponds to $\Delta f = 63\,\mathrm{GHz}$. The grey curve is obtained by applying the fitting Eqs. 88 and 89 with the simulation results.

3.6 CHAPTER SUMMARY

- Both backscattering and magneto-optical frequency splitting can lift the degeneracy of the counter-propagating modes in ring resonators.
- Both effects compete with each other and can cancel each other if one is significantly stronger than the other.
- Sidewall-induced backscattering can be reduced in magneto-optically active ring resonators.
- The interplay between backscattering and magneto-optical frequency splitting can be engineered in such a way that the resonator is critically coupled without a magnetic bias field present and that the resonance is suppressed upon switching on the bias field.
- The suppression of the transmission dip comes to saturation at increasing frequency splitting. This saturation is governed by the ratio between intrinsic quality factor and quality factor of the coupling between ring and the access waveguide Q_i/Q_{cpl}.
- Q_i 10 times larger than Q_e is required to suppress the dip to the level of $-3\,dB$.
- Thus, high Q rings are preferred for the application in view. For a 3 µm ring resonator with 10^6 intrinsic quality factor the suppression of the transmission dip to -1 dB was estimated with a gyrotropic splitting of 20 GHz.

Reciprocity in daily life Ⅳ: Nonreciprocal information flow

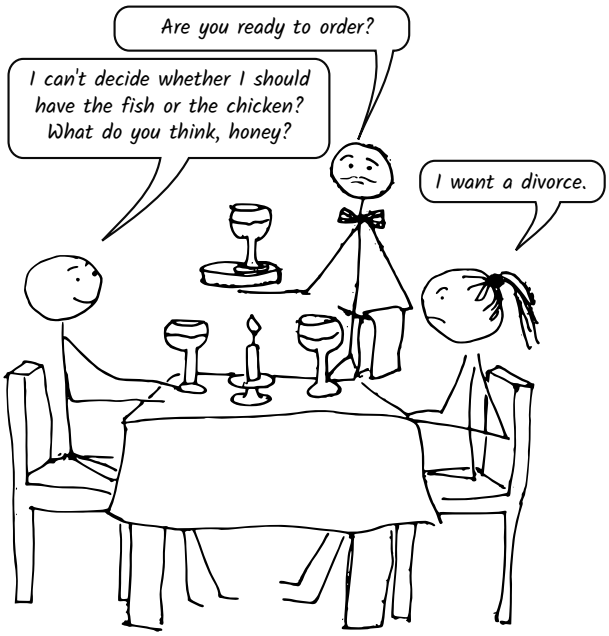

4

OPTICAL THREE-PORT CIRCULATORS MADE WITH RING RESONATORS

A concept for a circulator based on ring resonator is developed. The function is achieved by exciting the clockwise and counter-clockwise travelling modes and letting them interfere at the outputs.

Contents

In the previous chapter we have investigated what happens if the modes of a magneto-optically active ring resonator are coupled by sidewall roughness. In this chapter we show that a completely different behavior can be achieved if we couple the modes through the adjacent waveguides. Namely, we can build a circulator.

Commonly, non-integrated circulators break reciprocity by utilizing magneto-optically active materials. This poses a challenge to the miniaturization of such components as the currently available materials have a relatively weak response. The most compact isolators so far have been achieved by bonding a Ce:YIG garnet to a silicon on insulator waveguide and building an interferometer achieving lengths of 3.2 mm [120] and 325 µm [121]. A further reduction in size can be achieved by a resonance enhancement of the interaction between the light wave and the magneto-optical active medium. In this chapter we present a way to achieve such a resonant enhancement and compare it to existing resonant concepts.

4.1 PHOTONIC CRYSTAL VS RING RESONATOR

Resonant circulators can be divided in two categories: four-port circulators using ring resonators coupled to two waveguides [107, 122] and three-port circulators using photonic crystal resonators [24, 105, 123, 124]. For both concepts the footprint is comparable and is in the $10 \times 10\,\mu m^2$ range.

A circulator based on ring resonators uses the same working principle as the isolator presented in section 2.14.2.2. As shown in Fig. 36(a), an excitation from port 1 at resonance excites a counter-clockwise travelling wave which is either absorbed in the resonator or scattered to port 4 and radiation modes. Hence the transmission from port 1 to port 2 becomes very small. But for an excitation from port 2 only the clockwise resonance can be excited. Thus, at the resonance frequency of the counter-clockwise travelling wave, the power entering port 2 is transmitted to port 1. Fig. 36(b) shows the transmission between port 1 and 4. It is, except for resonator losses, the complementary to Fig. 36(a). It follows that all the power that is blocked from port 1 to port 2 is redirected to port 4 and we get the desired circulator port mapping ($1 \to 2$, $2 \to 3$, $3 \to 4$, $4 \to 1$) at the clockwise resonance and the reversed mapping at the counter-clockwise resonance.

In contrast to the previous approach, a photonic crystal circulator employs standing wave patterns. That means both a clockwise and a counter-clockwise travelling wave are excited and their interference builds two possible patterns that can be distinguished as an even and an odd mode. The magneto-optical phase shift now alters the interference between the two modes at the outputs [24, 105]. This in combination with the right symmetry and an adjusted coupling

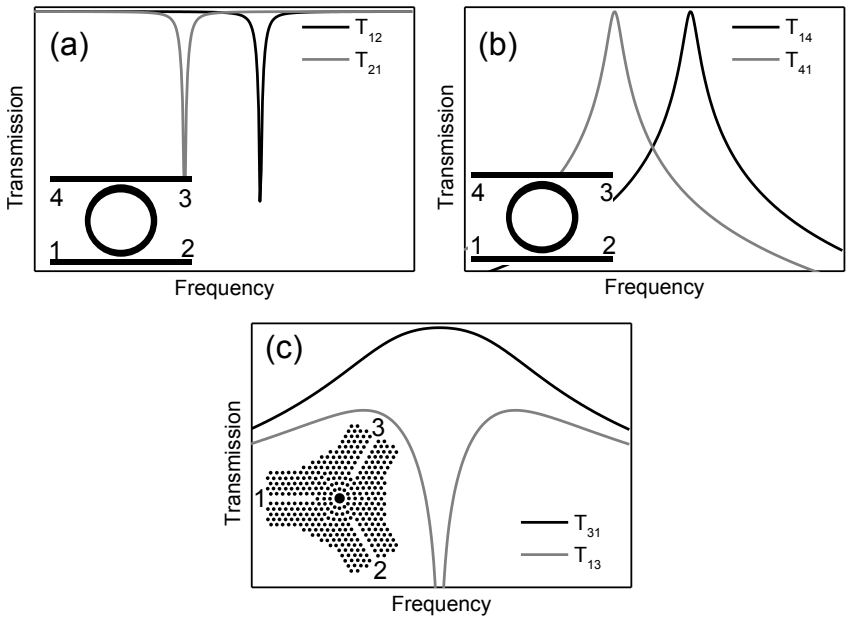

Figure 36: Comparison of the spectra of resonant circulators. (a) and (b) show the transmission spectrum of a magneto-optically active ring resonator coupled to two waveguides. (c) shows the structure and the spectrum of the circulator from Ref. [123].

to the waveguides can be used to build a three-port circulator. The spectrum of such a device is shown in Fig. 36(c).

Up to now ring resonator concepts lack the bandwidth of photonic crystal circulators. This inferior bandwidth is not due to an intrinsic resonator property but due to the way these two resonator types are coupled to the input waveguides (see section 4.4 for details). On the other hand, there are experimental realizations of magneto-optically active ring resonators [25, 26] and no such for photonic crystal resonators. The vertical confinement in the photonic crystal slab is too weak and the device therefore too lossy. The existing works on photonic crystal circulators are thus only concepts assuming a 2-dimensional geometry to circumvent the vertical confinement problem.

We propose to synergistically combine the preferable spectral properties of a three-port photonic crystal circulator with an experimentally much easier to handle ring resonator. The proposed circulator layout is shown in Fig. 37. A magneto-optically active ring resonator is evanescently coupled to three waveguides. Normally, an evanescent coupling would only excite either a clockwise or a counter-clockwise travelling wave, but we add Bragg reflectors to one end of the coupling waveguides to excite both waves. Except for some details we explain below, the working principle for this device is now very similar to the photonic crystal circulators described in Refs. [24, 105, 123, 124]. The magneto-optical active material causes the resonance frequencies of the clockwise and the counter-clockwise

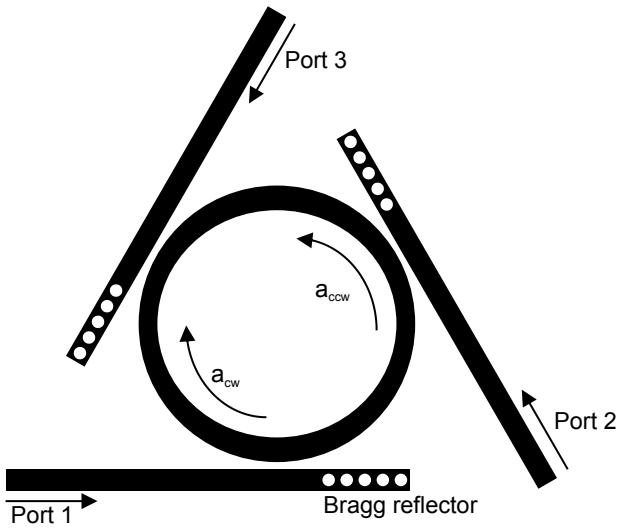

Figure 37: Principal circulator layout: The light is coupled into ports 1, 2, and 3 and excites a clockwise and counter-clockwise travelling wave in the ring resonator. The clockwise wave is excited by reflecting the input waves with a Bragg reflector.

travelling wave to split. By adjusting the waveguide to resonator coupling rate to the frequency splitting, it can be achieved that the clockwise and counter-clockwise waves interfere destructively at one output port and constructively at the other.

4.2 DERIVATION OF TRANSMISSION AND REFLECTION COEFFICIENTS

Like we did in the previous two chapters, we derive the transmission and reflection coefficients by employing temporal coupled-mode theory. As a first step, we investigate the structure without reflectors as shown in Fig. 38. The structure has now a threefold rotational symmetry as well as a mirror symmetry. The temporal coupled-mode equations have the same form as that of the ring resonator coupled to a single waveguide in section 2.14.2.1:

$$\frac{\mathrm{d}\mathbf{a}}{\mathrm{d}t} = \left(j\mathbf{\Omega} - \mathbf{\Gamma}_{cpl} - \Gamma_i\right)\mathbf{a} + \mathbf{K}^T\mathbf{p}_{in}, \tag{103}$$

$$\mathbf{p}_{out} = \mathbf{C}\mathbf{p}_{in} + \mathbf{D}\mathbf{a}. \tag{104}$$

The resonator and waveguide mode state vectors are in this case $\mathbf{a} = e^{j\omega t}\begin{pmatrix} a_{cw} & a_{ccw} \end{pmatrix}^T$, $\mathbf{p}_{in} = e^{j\omega t}\begin{pmatrix} p_{in,1}\ldots & p_{in,6} \end{pmatrix}^T$ and $\mathbf{p}_{out} = e^{j\omega t}\begin{pmatrix} p_{out,1}\ldots & p_{out,6} \end{pmatrix}^T$. Like before we can now greatly reduce the number of independent parameters in equations 103 and 104 by utilizing symmetries. From the mirror symmetry follows

$$\mathbf{D}\mathbf{M}_1 = \mathbf{M}_2\mathbf{D}, \tag{105}$$

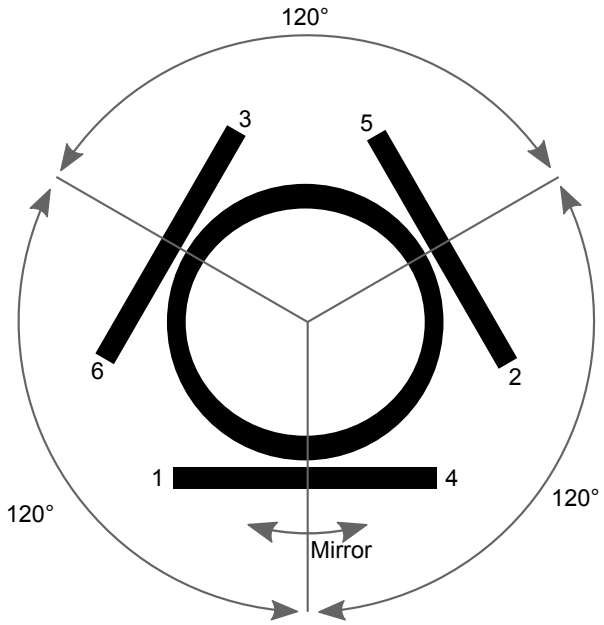

Figure 38: Ring resonator coupled to three waveguides. The light can enter through six ports and the structure has a 120° rotational symmetry as well as a mirror symmetry.

where $\mathbf{M}_1$ transforms the resonator modes

$$\tilde{\mathbf{a}} = \mathbf{M}_1 \mathbf{a} = \begin{pmatrix} 0 & 1 \\ 1 & 0 \end{pmatrix} \mathbf{a} \tag{106}$$

and $\mathbf{M}_2$ the waveguide modes

$$\tilde{\mathbf{p}}_{in/out} = \mathbf{M}_2 \mathbf{p}_{in/out} = \begin{pmatrix} 0 & 0 & 0 & 1 & 0 & 0 \\ 0 & 0 & 0 & 0 & 0 & 1 \\ 0 & 0 & 0 & 0 & 1 & 0 \\ 1 & 0 & 0 & 0 & 0 & 0 \\ 0 & 0 & 1 & 0 & 0 & 0 \\ 0 & 1 & 0 & 0 & 0 & 0 \end{pmatrix} \mathbf{p}_{in/out}. \tag{107}$$

To understand the effect of a rotation by 120° on the resonator modes, we inspect the spatial dependence of the electric field. In cylindrical coordinates it is $\mathbf{E}_{cw/ccw}(\rho, \phi, z) = \mathbf{e}(\rho, z) \exp(\pm jl\phi)$. Here, the coordinates are such that in Fig. 38 z points out of the plane towards the viewer and positive ϕ turn counter-clockwise. Together with the time dependence, $\exp(j\omega t)$, this means that an azimuthal propagation vector component, $+l$, signifies a clockwise travelling wave and a negative component, $-l$, connotes a counter-clockwise travelling wave. Besides being the azimuthal propagation vector component, l is also the azimuthal mode order, i.e. the number of wavelengths that fit into one resonator round trip. Because we model the system close to resonance and hence neglect dispersion, we assume l to be

an integer and to be constant within the considered bandwidth. A rotation by 120° will mean a delay for the clockwise mode and a jump ahead in time for the counter-clockwise mode. For the electric field this means: $\tilde{\mathbf{E}}_{cw/ccw}(\rho,\phi,z) = \mathbf{e}(\rho,z)\exp\left(\pm jl\left(\phi-\frac{2\pi}{3}\right)\right)$. Thus, we can conclude that the state vector components undergo a phase shift under rotation:

$$\tilde{\mathbf{a}} = \mathbf{R}_1\mathbf{a} = \begin{pmatrix} \exp\left(-jl\frac{2\pi}{3}\right) & 0 \\ 0 & \exp\left(+jl\frac{2\pi}{3}\right) \end{pmatrix}\mathbf{a}. \tag{108}$$

The transformation of the in- and out-going waves is much simpler. Here, only the coefficients are exchanged:

$$\tilde{\mathbf{p}}_{in/out} = \mathbf{R}_2\mathbf{p}_{in/out} = \begin{pmatrix} 0 & 0 & 1 & 0 & 0 & 0 \\ 1 & 0 & 0 & 0 & 0 & 0 \\ 0 & 1 & 0 & 0 & 0 & 0 \\ 0 & 0 & 0 & 0 & 0 & 1 \\ 0 & 0 & 0 & 1 & 0 & 0 \\ 0 & 0 & 0 & 0 & 1 & 0 \end{pmatrix}\mathbf{p}_{in/out}. \tag{109}$$

This leads to the following symmetry relation for $\mathbf{D}$:

$$\mathbf{D}\mathbf{R}_1 = \mathbf{R}_2\mathbf{D}. \tag{110}$$

Further, we assume smooth coupling which means that the clockwise travelling mode can only excite a wave leaving port 1, 2 or 3 and likewise the counter-clockwise mode can only excite a wave leaving port 4, 5 or 6. Together with equations 105 and 110, this leads to the fact that $\mathbf{D}$ can be written as:

$$\mathbf{D} = d\begin{pmatrix} 1 & 0 \\ \exp\left(+jl\frac{2\pi}{3}\right) & 0 \\ \exp\left(-jl\frac{2\pi}{3}\right) & 0 \\ 0 & 1 \\ 0 & \exp\left(-jl\frac{2\pi}{3}\right) \\ 0 & \exp\left(+jl\frac{2\pi}{3}\right) \end{pmatrix}. \tag{111}$$

Again there is a degree of freedom in the definition of the phase of d, which we set to be a real number. Equation 49 holds here as well and we obtain

$$d^2 = \frac{2}{3}\gamma_{cpl}. \tag{112}$$

The factor $\frac{1}{3}$ is due to the fact that γ_{cpl} is the decay rate into the three ports each of the two resonator modes can radiate into. If we assume that direct coupling between the ports is only possible for pairs of

ports that are facing each other, i.e. $(1,4)$, $(2,5)$ and $(3,6)$, we can use equation 67 to derive $\mathbf{C}$:

$$\mathbf{C} = \begin{pmatrix} 0 & 0 & 0 & -1 & 0 & 0 \\ 0 & 0 & 0 & 0 & -1 & 0 \\ 0 & 0 & 0 & 0 & 0 & -1 \\ -1 & 0 & 0 & 0 & 0 & 0 \\ 0 & -1 & 0 & 0 & 0 & 0 \\ 0 & 0 & -1 & 0 & 0 & 0 \end{pmatrix}. \tag{113}$$

Previously, we used the fact that $\mathbf{D}$ is a full rank square matrix to derive a relation between $\mathbf{K}$ and $\mathbf{D}$. Since this is not the case for this geometry we have to derive the relation in some other way. In the same way we used equation 40 to derive a symmetry relation for $\mathbf{D}$ (equation 45), we can use equation 103 to derive

$$\mathbf{M}_1\mathbf{K}^T = \mathbf{K}^T\mathbf{M}_2 \tag{114}$$

and

$$\mathbf{R}_1\mathbf{K}^T = \mathbf{K}^T\mathbf{R}_2. \tag{115}$$

Together with equation 64 this yields

$$\mathbf{K} = \mathbf{D}\begin{pmatrix} 0 & 1 \\ 1 & 0 \end{pmatrix}. \tag{116}$$

With these relations the temporal coupled-mode equations 103 and 104 have only five independent parameters left (γ_{cpl}, γ_i, ω_{cw}, ω_{ccw}, l) and we can calculate the scattering matrix of the system:

$$\begin{aligned} \mathbf{p}_{out} &= \mathbf{S}\mathbf{p}_{in} \\ &= \left[\mathbf{C} + \mathbf{D}\left(j\left(\omega\mathbf{I} - \mathbf{\Omega}\right) + \mathbf{\Gamma}_{cpl} + \Gamma_i\right)^{-1}\begin{pmatrix} 0 & 1 \\ 1 & 0 \end{pmatrix}\mathbf{D}^T\right]\mathbf{p}_{in}. \end{aligned} \tag{117}$$

Here, $\mathbf{I}$ is the identity matrix. We can rewrite this solution as

$$\mathbf{p}_{out,1-3} = \left(-\mathbf{I} + \frac{2}{3}\frac{\gamma_{cpl}}{j\left(\omega - \omega_{cw}\right) + \gamma_{cpl} + \gamma_i}\mathbf{P}\right)\mathbf{p}_{in,4-6}, \tag{118}$$

$$\mathbf{p}_{out,4-6} = \left(-\mathbf{I} + \frac{2}{3}\frac{\gamma_{cpl}}{j\left(\omega - \omega_{ccw}\right) + \gamma_{cpl} + \gamma_i}\mathbf{P}^T\right)\mathbf{p}_{in,1-3}, \tag{119}$$

where we splitted the input and output vectors such that $\mathbf{p}_{in,1-3}$ and $\mathbf{p}_{out,1-3}$ contain the first three ports and the other two vectors the last three. Further, the matrix $\mathbf{P}$ is defined as:

$$\mathbf{P} = \begin{pmatrix} 1 & \exp\left(-jl\frac{2\pi}{3}\right) & \exp\left(+jl\frac{2\pi}{3}\right) \\ \exp\left(+jl\frac{2\pi}{3}\right) & 1 & \exp\left(-jl\frac{2\pi}{3}\right) \\ \exp\left(-jl\frac{2\pi}{3}\right) & \exp\left(+jl\frac{2\pi}{3}\right) & 1 \end{pmatrix}. \tag{120}$$

With the six-port system now fully described, we can derive quite easily the scattering parameters for the three-port system with the reflectors in place as shown in Fig. 37. The reflector reflects back the wave leaving port 4, 5 and 6 which means in terms of scattering parameters:

$$\mathbf{p}_{in,4-6} = r \exp(j\psi)\, \mathbf{p}_{out,4-6}, \tag{121}$$

where $r \leq 1$ accounts for the reflection losses and the exponential function models the phase shift upon reflection. From equations 118, 119 and 121 it follows that

$$\mathbf{p}_{out,1-3} = r \exp(j\psi) \left(-\mathbf{I} + \frac{2}{3} \frac{\gamma_{cpl}}{j(\omega - \omega_{cw}) + \gamma_{cpl} + \gamma_i} \mathbf{P} \right) \left(-\mathbf{I} + \frac{2}{3} \frac{\gamma_{cpl}}{j(\omega - \omega_{ccw}) + \gamma_{cpl} + \gamma_i} \mathbf{P}^T \right) \mathbf{p}_{in,1-3}. \tag{122}$$

Since the reflection factor, $r \exp(j\psi)$, only appears here as a product, all scattering parameters are affected in the same way by it and it is just a general loss factor which simply scales the device transmission spectrum. For simplicity, we assume in the following that the reflector has negligible losses ($r \approx 1$) and provides a phase shift of 2π.

Hence, for a wave that is launched into port 1 the transmission and reflection factors are

$$R_{11}(\omega) = \frac{p_{out,1}}{p_{in,1}} = 1 - \frac{2}{3} \frac{\gamma_{cpl}}{j(\omega - \omega_{cw}) + \gamma_{cpl} + \gamma_i} - \frac{2}{3} \frac{\gamma_{cpl}}{j(\omega - \omega_{ccw}) + \gamma_{cpl} + \gamma_i} + A, \tag{123}$$

$$T_{21}(\omega) = \frac{p_{out,2}}{p_{in,1}} = -\frac{2}{3} \frac{\gamma_{cpl} \exp(+jl2\pi/3)}{j(\omega - \omega_{cw}) + \gamma_{cpl} + \gamma_i} - \frac{2}{3} \frac{\gamma_{cpl} \exp(-jl2\pi/3)}{j(\omega - \omega_{ccw}) + \gamma_{cpl} + \gamma_i} + A, \tag{124}$$

$$T_{31}(\omega) = \frac{p_{out,3}}{p_{in,1}} = -\frac{2}{3} \frac{\gamma_{cpl} \exp(-jl2\pi/3)}{j(\omega - \omega_{cw}) + \gamma_{cpl} + \gamma_i} - \frac{2}{3} \frac{\gamma_{cpl} \exp(+jl2\pi/3)}{j(\omega - \omega_{ccw}) + \gamma_{cpl} + \gamma_i} + A, \tag{125}$$

where A is

$$A = \frac{4}{9} \frac{(\gamma_{cpl})^2}{(j(\omega - \omega_{cw}) + \gamma_{cpl} + \gamma_i)(j(\omega - \omega_{ccw}) + \gamma_{cpl} + \gamma_i)} \cdots \ldots * (1 + \exp(+jl2\pi/3) + \exp(-jl2\pi/3)). \tag{126}$$

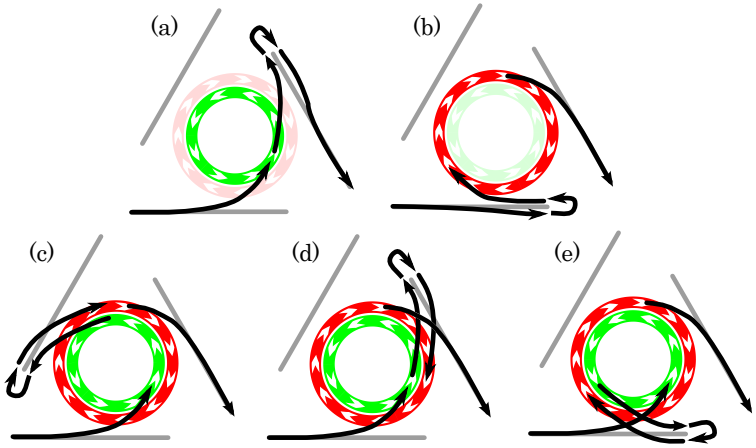

Figure 39: Five different optical paths are shown that contribute to the transmission from port 1 to port 2. The clockwise travelling resonance is depicted by the inner green ring, the counter-clockwise resonance is depicted by the outer red ring.

Due to the three-fold rotational symmetry, all other transmission and reflection coefficients are defined by the above equations as well. The transmission coefficients T_{21} and T_{31} consist of five summands. The first two summands are similar to those found for photonic crystal defect circulators in Refs. [105] and [124] except for one principal difference: the mode order l appears in the exponentials $\exp(+jl2\pi/3)$ and $\exp(-jl2\pi/3)$. The mode order for photonic crystal defects is usually 1 and was therefore not explicitly mentioned in Refs. [105, 124]. For ring resonators l can be an arbitrary high integer and will influence the device behaviour. The remaining three summands are collected as A in equations 123–126 and are not found in photonic crystal defect circulators.

Apart from the mode order only Ref. [124] models intrinsic resonator losses and thus γ_i do not appear in Ref. [105].

The five summands can be understood as the possible paths the light can take from one port to the other. Figure 39 shows the five possible optical paths which contribute to the transmission from port 1 to port 2. For the first path the light is coupled to the counter-clockwise travelling wave, is then coupled to the waveguide of port 2, is reflected in the Bragg reflector and then transmitted to port 2. For the second path the light is reflected from the Bragg reflector of the waveguide of port 1, is then coupled to the clockwise resonance and transmitted to port 2. These two paths create the first two summands in Eq. 124 and if only these two paths were possible the transmission would be identical to those of photonic crystal circulators in Refs. [105, 124]. But for our circulator there are three additional paths possible which are shown in Fig. 39 (c–e) and are responsible for the three summands in Eq. 126. For these paths, first the counter-clockwise resonance is excited, then the light is coupled to one of the three waveguides, reflected in the Bragg reflector and now not like in Fig. 39a transmitted to the port but coupled to the clockwise reson-

ance and only then transmitted to port 2. These three paths involve a successive excitation of the counter-clockwise and the clockwise resonance. That is why the three summands of A are proportional to $(\gamma_{cpl})^2$ and have both resonances in their denominator.

4.3 CRITICAL COUPLING AND EFFECT OF THE MODE SYMMETRY

Critical coupling means for this resonator that at resonance $T_{21}$is zero and T_{31} is maximized, or vice versa. Setting T_{21} to zero in equation 124 yields:

$$l \neq 3n \tag{127}$$

where n is an integer, and

$$\gamma_{cpl} + \gamma_i = -\sqrt{3}\delta\omega\,(-1)^l\,. \tag{128}$$

Setting T_{31} to zero yields also Eq. 127 and

$$\gamma_{cpl} + \gamma_i = +\sqrt{3}\delta\omega\,(-1)^l\,. \tag{129}$$

We define the frequency splitting as $\delta\omega = \omega_0 - \omega_{ccw} = \omega_{cw} - \omega_0$. In contrast to the critical coupling conditions of the previous devices, the frequency splitting and the mode order need to be considered. Firstly, the splitting needs to be balanced with the total resonator loss rate. Secondly, since we are only concerned with passive devices, the loss rate is a positive number which means the right-hand sides of equations 128 and 129 need to be positive as well. As both cases have opposite signs, T_{21} and T_{31} cannot simultaneously be zero. Thus the mode order has a strong influence on the device behaviour. Assuming a positive $\delta\omega$, for $l = 3n - 1$ the transmission from port 1 to 3 is zero and the port mapping is ($1 \to 2$, $2 \to 3$, $3 \to 1$) and for $l = 3n - 2$ it is ($1 \to 3$, $3 \to 2$, $2 \to 1$) and T_{21} is zero. For negative $\delta\omega$ the port mapping is reversed. Fig. 40 shows the transmission spectra for negative $\delta\omega$. It can be seen that a change in mode order indeed influences whether port 1 and 2 or port 1 and 3 are coupled. The figure further shows the phasors of the three paths in Fig. 39c–e summarized as A in equations 123–126. For the cases in which the device shows circulation ($l = 3n - 1$, $l = 3n - 2$) the paths interfere destructively and the phasors add up to zero. Only for $l = 3n$ there is constructive interference, but in this case T_{21} equals T_{31} and the device does not function as a circulator.

This statement is only true for $\gamma_i \neq 0$. For $\gamma_i = 0$, $T_{21} = T_{31} = 0$ if $l = 3n$.

4.4 ISOLATION BANDWIDTH AND INSERTION LOSS

Since a four-port circulator like the one in Fig. 36a can be turned into a three-port circulator by terminating one port with a reflector, the here presented circulator has no functional advantage over the ring resonator concept with travelling waves. However, we will show that

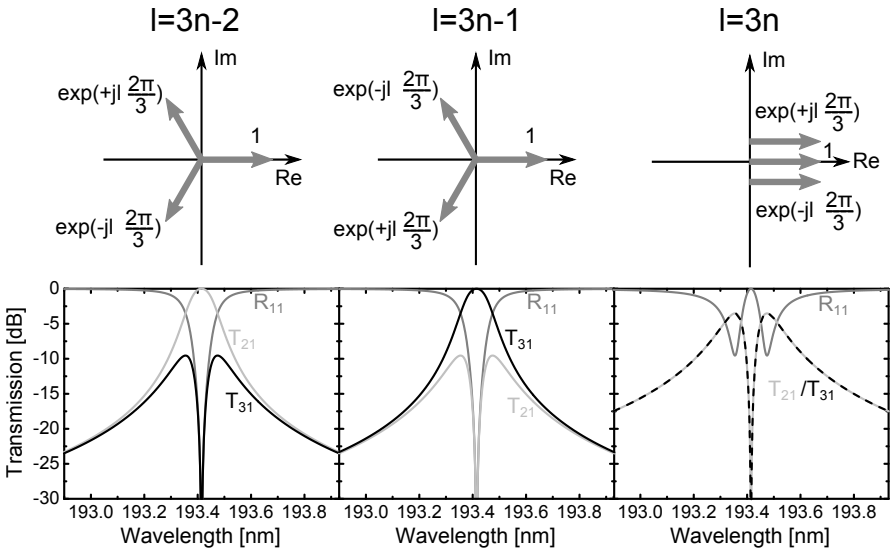

Figure 40: Phasors of the paths in Fig. 39c–e and transmission spectra for different mode orders. The frequency splitting $\delta\omega$ is negative and $\gamma_i = 0$.

the former design offers a better device performance. In the following we will compare which of the two devices is the more efficient arrangement in terms of bandwidth and isolation loss. We start with the standing wave circulator. If we assume that T_{21} is the blocking direction, we obtain the isolation bandwidth by equating the desired isolation ratio I to the ratio $|T_{21}/T_{31}|^2$, inserting equations 124 and 125 and solve for ω. This will yield a quadratic equation. The difference between the two roots is the isolation bandwidth. We obtain

$$\Delta\omega_{IBW} = 2\pi\Delta f_{IBW} = 4\sqrt{3}|\delta\omega|\sqrt{\frac{I}{1-I}}. \tag{130}$$

If T_{31} was the blocking direction we would have obtained the same result. The isolation bandwidth solely depends on $\delta\omega$ but it should be noted that if the frequency splitting gets very small the critical coupling condition in equations 128 and 129 cannot be fulfilled any more because γ_i cannot be arbitrarily small as there are always intrinsic resonator losses.

The insertion loss is the inverted transmission coefficient in passing direction squared, i.e. $1/|T_{21}|^2$ or $1/|T_{31}|^2$. At resonance this is

$$IL = \frac{3\delta\omega^2}{\left(\sqrt{3}|\delta\omega| - \gamma_i\right)^2}. \tag{131}$$

An insertion loss of $IL = 1$ would mean that there are no transmission losses. The larger the intrinsic resonator loss rate γ_i is in relation to the frequency splitting $\delta\omega$, the larger is the insertion loss.

Using temporal coupled-mode theory, as we did for the previous cases, yields the following transmission coefficients for the travelling wave four-port circulator:

$$T_{41} = \frac{(-1)^l \gamma_{cpl}}{j(\omega - \omega_{ccw}) + \gamma_i + \gamma_{cpl}}, \tag{132}$$

$$T_{14} = \frac{(-1)^l \gamma_{cpl}}{j(\omega - \omega_{cw}) + \gamma_i + \gamma_{cpl}}, \tag{133}$$

$$T_{21} = \frac{\gamma_{cpl}}{j(\omega - \omega_{ccw}) + \gamma_i + \gamma_{cpl}} - 1 \tag{134}$$

and

$$T_{12} = \frac{\gamma_{cpl}}{j(\omega - \omega_{cw}) + \gamma_i + \gamma_{cpl}} - 1. \tag{135}$$

The port naming is as in Fig. 36a and the remaining transmission coefficients can be obtained from the rotational symmetry. Calculating the isolation bandwidth as before yields for the connection between port 1 and 4:

$$\Delta\omega_{IBW,14} = 2\pi\Delta f_{IBW,14} = 2\sqrt{\frac{4I}{(1-I)^2}\delta\omega^2 - \left(\gamma_{cpl} + \gamma_i\right)^2}. \tag{136}$$

We can find the minimally necessary $\delta\omega$ by setting the above equation to zero:

$$|\delta\omega| \geq \frac{\gamma_{cpl} + \gamma_i}{2}\sqrt{\frac{(1-I)^2}{I}}. \tag{137}$$

Finding the isolation bandwidth between port 1 and 2 involves solving a fourth-order polynomial which yields a long winded expression. But a compact expression can be obtained if one assumes that $\delta\omega \gg \gamma_i + \gamma_{cpl}$. This means that the clockwise and the counter-clockwise resonance are well separated and the transmission in passing direction is roughly unity. The bandwidth is in this case only dependent on the two resonator loss rates:

$$\Delta\omega_{IBW,12} = 2\pi\Delta f_{IBW,12} = 2\sqrt{\frac{I\left(\gamma_{cpl} + \gamma_i\right)^2 - \gamma_i^2}{1-I}}. \tag{138}$$

The extinction in the large $\delta\omega$ limit is dependent on the coupling strength in relation to the intrinsic loss rate. For a four-port resonator there is no critical coupling condition and the transmission between port 1 and 2 cannot be zero for non-zero γ_i. The stronger the resonator is coupled the better the extinction. Thus to reach the required isolation level I, γ_{cpl} needs to be larger than $\left(\sqrt{\frac{1}{I}} - 1\right)\gamma_i$, otherwise the expression in equation 138 becomes complex. Thus, for the isolation level, I, to be $1/100$ or $-20\,\mathrm{dB}$, γ_{cpl} needs to be 9 times larger than γ_i. The condition for the quality factors is inverse and thus Q_i needs to be 9 times larger than Q_{cpl}.

The strongest isolation is approximately achieved at the resonance of the blocking direction. We can find the minimally necessary $\delta\omega$ to

achieve a certain isolation by calculating the isolation at the respective resonance frequency and solving for $\delta\omega$:

$$|\delta\omega| \geq \frac{\gamma_i \left(\gamma_{cpl} + \gamma_i\right)}{2} \sqrt{\frac{1 - I}{I \left(\gamma_{cpl} + \gamma_i\right)^2 - \gamma_i^2}}. \tag{139}$$

We assume here that the maximum isolation is found exactly at the resonance frequency in blocking direction which is only correct if the slope of the spectral function in transmitting direction is zero. The slope of the transmission spectrum goes to zero if both resonances are infinitely seperated but it is already a good approximation for frequency splittings of twice the FWHM.

In contrast to $(1 \rightarrow 2)$, the connection between port 1 and port 4 is off resonance in blocking direction and the isolation bandwidth grows for large $\delta\omega$ linearly. Nonetheless, this increase in bandwidth is limited for practical purposes as here the transmission direction is on-resonance and the insertion loss will become prohibitively high for frequencies too far away from the resonance frequency.

We can also calculate the insertion loss for the travelling wave circulator at resonance frequency:

$$IL_{14} = \frac{\left(\gamma_{cpl} + \gamma_i\right)^2}{\gamma_{cpl}^2} \tag{140}$$

and

$$IL_{12} = \frac{\left(\gamma_{cpl} + \gamma_i\right)^2 + 4\delta\omega^2}{\gamma_i^2 + 4\delta\omega^2}. \tag{141}$$

The larger the coupling rate is compared to the intrinsic loss rate, the more efficiently light can be coupled from port 1 to port 4. The insertion loss between port 1 and 2 goes to 1, i.e. there are no losses, if the clockwise and the counter-clockwise resonance are well separated.

These rather abstract relations are summarized in Fig. 41. A ring resonator with an intrinsic quality factor of $Q_i = 200000$ and with varying frequency splitting $\Delta f = \delta\omega/\pi$ is used for a standing wave three-port circulator and for a travelling wave four-port circulator. Both designs are compared in terms of isolation bandwidth and insertion loss. One can immediately see that the three-port circulator outperforms the four-port circulator. The three-port circulator features a larger isolation bandwidth and a lower insertion loss. Furthermore, the four-port circulator has conflicting requirements for the isolation between two ports connected through the ring resonator (e.g. port $1 \leftrightarrow 4$) and the isolation in one waveguide (e.g. port $1 \leftrightarrow 2$). The latter is shown in Fig. 41c. The stronger the coupling and thus the lower Q_{cpl}, the better the extinction in the resonance dip and with that the isolation. If Q_{cpl} gets too big, the extinction becomes even so low that the desired isolation of $-20\,\mathrm{dB}$ cannot be achieved at all. In this case the expression for $\Delta\omega_{IBW,12}$ in equation 138 becomes complex.

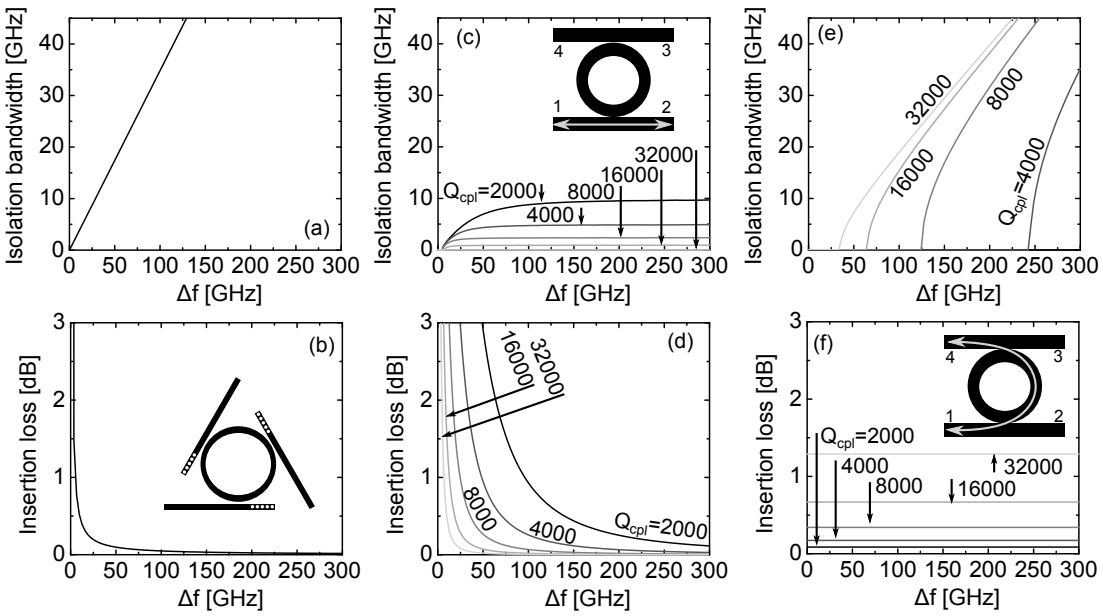

Figure 41: Comparison of the $-20\,\mathrm{dB}$ isolation bandwidth and the insertion loss of a three-port and a four-port circulator. In both cases a ring resonator with an intrinsic quality factor of $Q_i = 200000$ and a resonance at $1.55\,\mu\mathrm{m}$ was considered. (a) and (b) show the two parameters for the three-port circulator. γ_{cpl} and thus Q_{cpl} are chosen according to the conditions for critical coupling 128 and 129. (c) to (f) show the investigated parameters for the four-port circulator. The first two panels depict the parameters for a connection between port 1 and 2 and the last two for a connection between port 1 and 4 through the resonator. As there is no critical coupling condition for the four-port circulator, the parameters are shown for five different Q_{cpl}.

For this particular example the upper limit for Q_{cpl} is $Q_i/9 = 22222$. Thus, in Fig. 41c the isolation bandwidth for $Q_{cpl} = 32000$ is zero for all Δf. In contrast, for the $1 \leftrightarrow 4$ isolation we profit from a high Q_{cpl}. In that case we transmit on-resonance and block off-resonance. Here we profit from a narrow resonance such that both resonances can be clearly distinguished. A narrow resonance is synonymous with a large total quality factor, $1/Q_{total} = 1/Q_i + 1/Q_{cpl}$. It follows that a lower Q_{cpl} will cause a lower Q_{total} and, thus, a larger Δf is needed to separate the two resonances. The needed $\delta\omega = \pi\Delta f$ can be calculated from equation 137. For example, a ring resonator with $\Delta f = 75\,\text{GHz}$ and an isolation bandwidth of 10 GHz requires a Q_{cpl} of larger or equal 16000. Combined with the upper limit for the $1 \leftrightarrow 2$ connection there is only a narrow range of values for Q_{cpl} that achieve sufficient isolation. For more realistic Q_i around 10000 this problem gets even more severe such that the upper and lower requirement Q_{cpl} can only simultaneously satisfied for unrealistically high Δf. These demanding requirements for Δf, Q_i and Q_{cpl} can be slightly less severe if one allows for a lower isolation ratio. Accordingly, the four-port isolator has been shown to work in experiment but only with an isolation of $-10\,\text{dB}$ [125].

The three-port circulator as well has a minimal requirement on Δf to ensure functionality. Depending on the mode order, we need to fulfill either the critical coupling condition 128 or 129, from which we can derive the minimally necessary Δf:

$$\frac{\gamma_i}{\pi} = \frac{f_0}{Q_i} = \sqrt{3}\Delta f_{min}. \tag{142}$$

We arrive at the above equation, if we assume a resonator with a certain intrinsic loss rate, γ_i. We arrive at the minimally necessary frequency splitting by assuming that the resonator is infinitely weakly coupled and thus the coupling loss rate, γ_{cpl}, approaches zero. For a resonance wavelength of 1.55 µm corresponding to $f_0 = 193.5\,\text{THz}$ and an intrinsic quality factor of $Q_i = 200000$, we obtain $\Delta f_{min} = 0.56\,\text{GHz}$. Note that this is the limit case of infinitely weak coupling to the resonator which would cause 100 % reflection from the input waveguide. Thus a γ_{cpl} slightly larger than zero is needed and with that also a Δf slightly larger than Δf_{min}. A detailed discussion of this follows in the next section. For a lower $Q_i = 50000$, we obtain $\Delta f_{min} = 2.2\,\text{GHz}$. In contrast to this number we can derive from equation 137 the minimally necessary frequency splitting to achieve $-20\,\text{dB}$ isolation between port 1 and port 4 of the travelling wave circulator. In case of $Q_i = 50000$, we get $\Delta f_{min} = \frac{f_0}{2Q_i}\sqrt{\frac{(1-I)^2}{I}} = 19.2\,\text{GHz}$ and thus almost an order of magnitude more than what is needed for the standing wave circulator.

4.5 REFLECTIONS FROM LOW Q_i CIRCULATORS

A parameter that we have neglected so far is the reflection of the three-port circulator. The reason is that for large Q_i and $\Delta f = \pi \delta \omega$ these are negligible. We can derive the reflection at the resonance frequency f_0 from equation 123 by inserting the appropriate critical coupling condition, 128 and 129. This yields the following power reflection factor:

$$|R_{11}(f_0)|^2 = \frac{1}{3}\left(\frac{\gamma_i}{\delta\omega}\right)^2. \tag{143}$$

Firstly, we see that although the critical coupling condition ensures that the transmission is zero at resonance in blocking direction, it does not ensure zero reflections from the circulator. Secondly, a large Q_i and with that a low γ_i combined with a large $\delta\omega$ yield a low reflection device. However, if $\delta\omega$ is of the same order of magnitude as γ_i, the three-port circulator will feature substantial reflections. This case is shown in Fig. 42b for a ring resonator with $Q_i = 35000$ and $\Delta f = 20\,\text{GHz}$. Although, the device shows low insertion loss and good isolation, $-15\,\text{dB}$ of the incoming signal will be immediately reflected. This defeats the intended purpose of the circulator. A solution can be found in Fig. 42a. The figure shows the isolation and reflection at resonance for various γ_{cpl} and the corresponding Q_{cpl}. We can see that the isolation and reflection are zero for different γ_{cpl} and we can find a simultaneously low isolation and reflection for an intermediate γ_{cpl}. Fig. 42c shows the case in which γ_{cpl} was chosen such that the $-20\,\text{dB}$ bandwidth is the same for reflection and isolation. The corresponding γ_{cpl} can be roughly found in Fig. 42a at the crossing point of isolation and reflection. The reason why it is not exactly the crossing point is that the spectral shape of transmission and reflection is slightly different and thus optimizing for maximized bandwidth in reflection and isolation is only approximately the same as optimizing for minimal reflection and transmission at resonance. For all practical purposes the two optimizing goals can be considered identical. In the example of Fig. 42, optimizing for minimal reflection and transmission would yield a $\gamma_{cpl} = 109 \times 10^9\,1/\text{s}$ and optimizing for maximal bandwidth would yield $\gamma_{cpl} = 110 \times 10^9\,1/\text{s}$.

Fig. 43 shows the resulting $-20\,\text{dB}$ bandwidth for reflection and isolation as a function of Δf in case of a critically coupled resonator and in case of a resonator with coupling optimized for simultaneously maximized reflection and isolation bandwidth. We can see that the critically coupled resonator has a much lower threshold for isolation but achieves low reflections only for much larger Δf. The resonator with optimized coupling yields an intermediate threshold for both parameters and therefore allows for practical devices for lower Δf.

The discontinuity at $\Delta f = \Delta f_{min} = 3.2\,\text{GHz}$ for the critically coupled resonator is due to the fact that we enforce critical coupling condition.

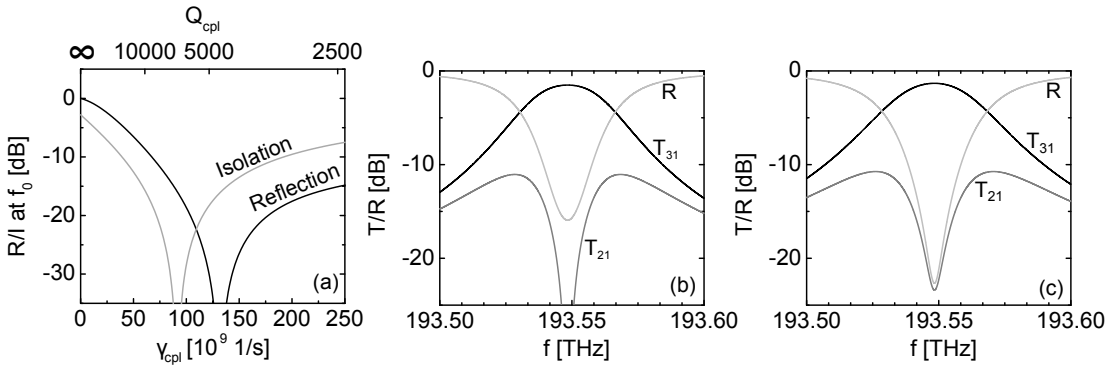

Figure 42: (a) Reflection and isolation at resonance frequency as a function of γ_{cpl} (lower axis) and Q_{cpl} (upper axis). As a basis for this circulator serves a ring with $Q_i = 35000$ and $\Delta f = 20\,\text{GHz}$. (b) Transmission and reflection in dB with a critically coupled ring, $\gamma_{cpl} = 91.5 \times 10^9\,1/\text{s}$. (c) Transmission and reflection for a slightly stronger coupling, $\gamma_{cpl} = 110 \times 10^9\,1/\text{s}$.

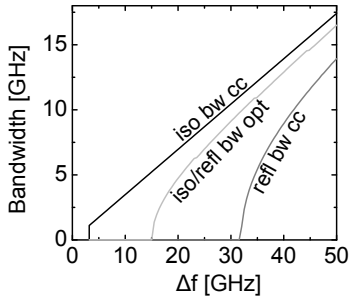

Figure 43: $-20\,\text{dB}$ isolation and reflection bandwidth if the resonator is critically coupled (iso bw cc, refl bw cc) compared to the case with an optimized bandwidth (iso/refl bw opt). The ring resonator has an internal quality factor of 35000.

For lower Δf it is not possible to find a γ_{cpl} such that the transmission in blocking direction is zero.

4.6 THE CIRCULATOR AS AN ISOLATOR

Interestingly, the three-port circulator can also serve as an isolator that can outperform the isolator build up from one ring resonator and a single waveguide as described in section 2.14.2.2. For this purpose one of the three ports is reflection-free terminated such that the power leaving this port is either radiated or absorbed. One possible implementation of this would be a gradual decreasing waveguide width which would transform the guided waveguide mode into radiation modes.

Fig. 44 shows the comparison between the two devices. In both cases the device is based on a ring resonator with an internal quality factor of $Q_i = 35000$. The two-port isolator behaves similarly to the $1 \leftrightarrow 2$ connection of the four-port circulator. For large Δf the

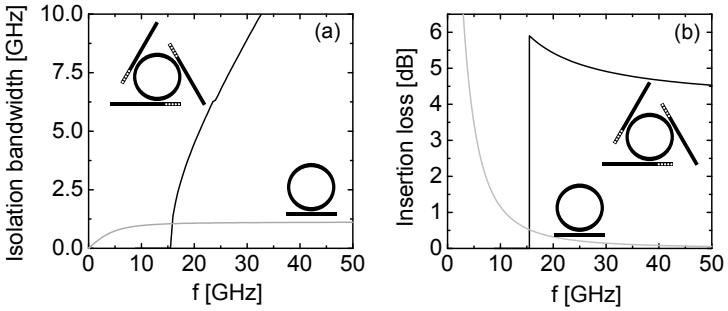

Figure 44: Comparison of a three-port circulator serving as an isolator to an isolator build up from a single waveguide. The intrinsic quality factor is in both cases $Q_i = 35000$. The -20 dB isolation bandwidth is shown in (a) and (b) shows the insertion loss for both devices.

isolation bandwidth is limited by the resonance width and therefore saturates. A difference to the four-port circulator is that the two-port isolator can be critically coupled (equation 79) and therefore the device provides isolation already for infinitesimal small Δf. The isolation bandwidth of the three-port circulator does not saturate and can therefore provide a superior isolation bandwidth for large enough Δf. The coupling was adjusted for optimal reflection and isolation bandwidth as discussed in the previous section. As we can see from Fig. 44b we pay for the increased bandwidth with a higher insertion loss. The reason that the insertion loss of the single waveguide isolator asymptotically approaches zero with increasing Δf is the fact that in transmission direction the resonance frequency is moving further and further away from the operating frequency and the light interacts less and less with the ring. On the other hand, in case of the three-port circulator, both in forward in backward direction the light needs to strongly interact with the ring resonator.

4.7 EXAMPLE

To prove the validity of our concept we simulated a ring resonator similar to Ref. [107]. The ring consists of inactive material (in our case silicon ($n = 3.5$), in Ref. [107] it is Si3N4) and magneto-optically active garnet. The garnet has a refractive index of 2.22 and a Verdet constant of $4000\,^\circ/m$. If magnetized perpendicularly to the ring plane, the two degenerate TE-polarized clockwise and counter-clockwise modes split in frequency. In our example we choose a ring with 10 µm radius with silicon and garnet thickness of 220 nm. The silicon part is 250 nm wide and the garnet is 700 nm wide. Such a ring resonator features a resonance splitting of $2\delta\omega = 2\pi\Delta f = 2\pi \cdot 63\,\mathrm{GHz}$. We would like to emphasize that this type of ring resonator only serves as an example. The concept will also work with other types of magneto-optically active ring resonators like for example the TM-mode resonator in [26] as long as there is a rotational symmetry. The

coupling waveguides are considered to be made from silicon and are assumed to be 330 nm wide. Similar to Refs. [105, 124] the coupling strength should be adjusted for the maximal transmission, thus the gap between coupling waveguide and ring waveguide is 250 nm. The Bragg reflector is built from regularly spaced holes in the waveguide [126], which are 200 nm in diameter. The whole structure is buried in silica with a refractive index of 1.45. We used the FEM frequency domain solver in CST Microwave Studio to calculate the circulator response. To reduce memory consumption, we inserted in the centre of the ring a perfectly conducting cylinder of radius 9 µm. This does not have any effect on the rings optical properties as with or without this cylinder the field is practically zero in this region. Because Microwave Studio only allows rectangular boundaries we needed to bend two of the coupling waveguides in order for them to touch the boundary orthogonally (see Fig. 45). The simulation results can be seen in Fig. 46. The dots represent the FEM results and the lines show the fit of equation 123–126 to the simulation data. It can be seen that the temporal coupled-mode theory can reproduce the spectral behaviour very well and the $\delta\omega$ obtained from fitting agrees with the $\delta\omega$ obtained from simulating the uncoupled ring within 5%. Fig. 45 shows the out-of-plane H-field at resonance for an excitation from all three sides. As expected the excitation from port 1 transmits the power to port 3, an excitation from port 2 is transmitted to port 1 and an excitation from port 3 ends up in port 2. Thus, the desired circulating behaviour is achieved. The isolation bandwidth can be calculated from equation 130, which yields a 22 GHz bandwidth. The insertion loss of the device is 0.6 dB. The intrinsic Q-factor of our ring is 36000. As it can be seen from equation 130, the isolation bandwidth is independent of the Q-factor. A lower intrinsic Q-factor would only mean a higher insertion loss [124].

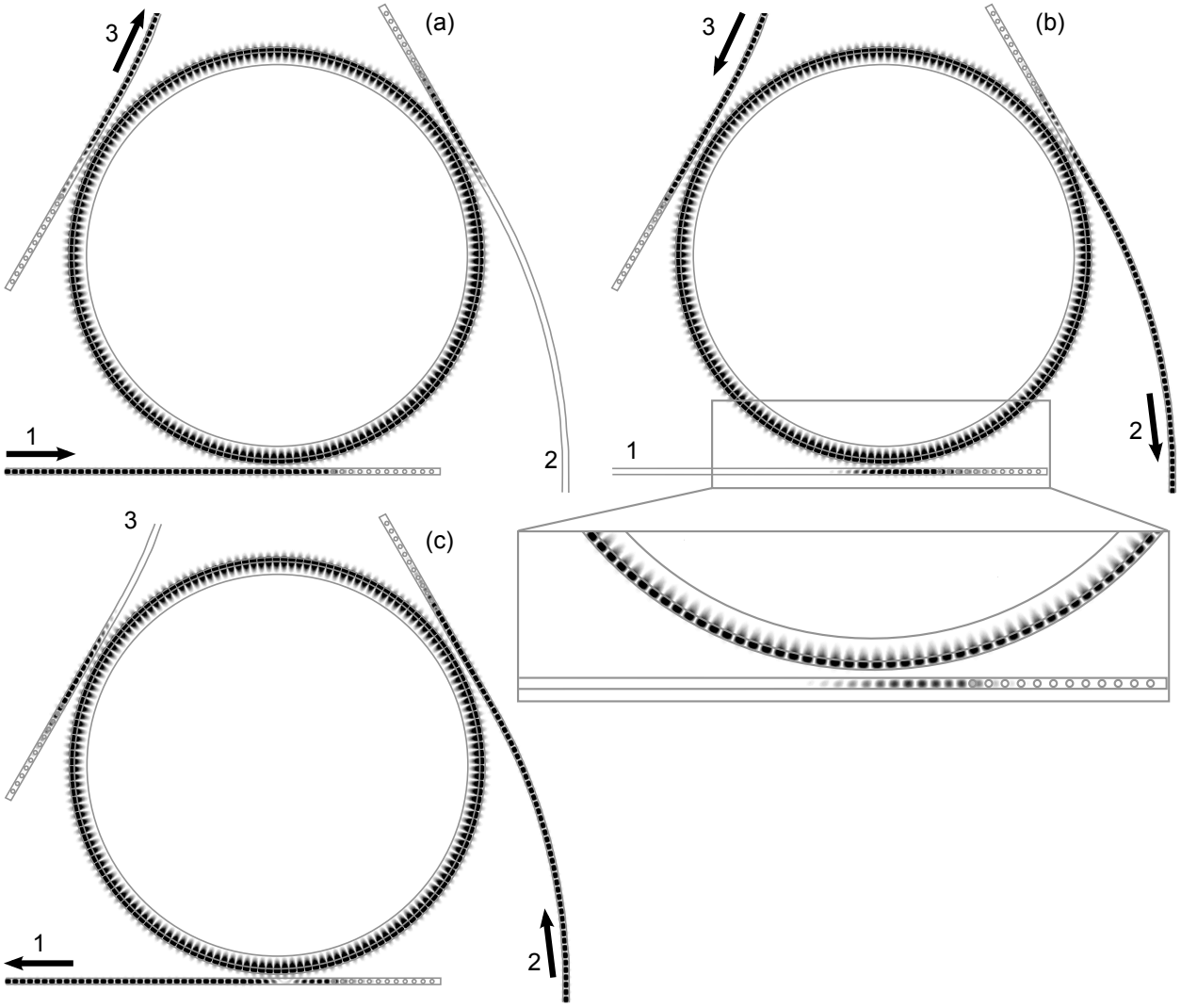

Figure 45: H-field. The arrows indicate where the light enters the structure and where it exits. (a) shows the excitation from port 1, (b) from port 3 and (c) from port 2. The inset shows how the wave coming directly from the resonator interferes destructively with that coming from the reflector in order to block the transmission to port 1.

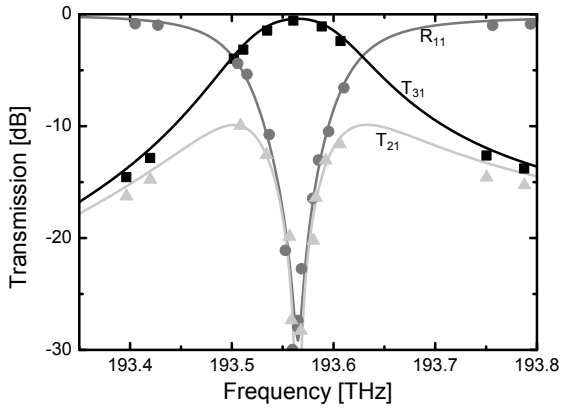

Figure 46: Resonator spectrum: The dots are obtained from an FEM frequency domain simulation. The solid lines are obtained from fitting the FEM results to the coupled-mode theory model in Eqs. 123–126. In this fitting procedure ω_0, $\delta\omega$, γ_r, and γ_c were used as variables.

4.8 CHAPTER SUMMARY

- Ring resonator-based travelling wave circulators rely on the splitting of the counter-clockwise and the clockwise propagating mode.
- Photonic crystal defect-based circulators employ the nonreciprocal coupling between two standing wave patterns.
- We have proposed a circulator based on a ring resonator working on the same principles as photonic crystal circulators but which is much easier to implement experimentally.
- Our approach yields a superior isolation bandwidth compared to travelling wave resonators.
- Such a device yields also a superior isolation bandwidth when compared to a travelling wave isolator, albeit with inferior insertion loss.

Reciprocity in daily life V: Nonreciprocal traffic

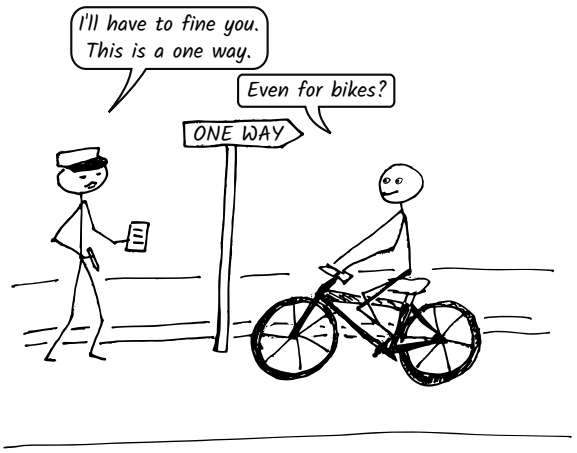

5

MEASURING THE MAGNETO-OPTICAL PHASE SHIFT

A method to measure the magneto-optical phase shift is presented. The method is so sensitive that even the relatively weak effect in silicon waveguides could be measured.

Contents

5.1 LAYOUT TO MEASURE THE MAGNETO-OPTICAL PHASE SHIFT

In this chapter a measurement setup is presented that can measure the magneto-optical phase shift in integrated waveguides. It is based on Ref. [127]. The setup is intended to be so sensitive that it can measure the contribution of silicon to the phase shift. In Fig. 47a the principle layout of the experiment, a Mach-Zehnder interferometer (MZI), is shown. A tunable laser serves as a light source while the polarization is adjusted with a fibre paddle, a polarizing beam splitter cube and a half-wave plate. The interferometer is made up of a free-space reference arm and a sample arm that leads through the waveguide. The magnetic field is applied with a magnetic head similar to the one used in Ref. [128]. The magnetic field is produced by a coil with 2000 turns which is driven with 20 mA and is applied to the waveguide through an air gap of 300 µm width and 3 mm length. Thus, roughly 0.2 T can be applied to the waveguide. Fig. 47b shows a cross-section of the magnetic head and waveguide. The magnetic field is applied horizontally, which means that the TM-mode will feature a magneto-optical phase shift and the TE-mode will not (see section 2.12.2). For the given magnetic field and gap length the expected magneto-optical phase shift of a silicon slab waveguide on silica substrate will be of the order of a fraction of a degree which is too small to measure directly. Therefore, the magnetic field is modulated with $f_{mod} = 1\,\mathrm{kHz}$ and a lock-in amplifier is used to filter the modulated signal. Simultaneously, the time average signal is recorded with a voltmeter. From the ratio of lock-in signal to voltmeter signal the magneto-optical phase shift can be calculated [127].

The photocurrent of the detector is proportional to the optical intensity which depends on the interference between sample and reference arm:

$$I_{photo} \sim |E_{MZI}|^2 = |E_{sample} e^{j(\varphi + \delta\varphi(t))} + E_{reference}|^2, \qquad (144)$$

where I_{photo} is the photocurrent, E_{MZI} is the amplitude of the wave leaving the MZI, E_{sample} and $E_{reference}$ are the wave amplitudes in the sample and the reference arm, φ is the static phase difference between sample and reference arm and $\delta\varphi(t) = \delta\varphi_{max} \sin(2\pi f_{mod} t)$ is the change in phase due to magneto-optical modulation. Because of the aperture in the reference arm in Fig. 47a, E_{sample} and $E_{reference}$ can always be adjusted to be equal ($E_{sample} = E_{reference} = E_0$). Evaluating the absolute square in Eq. 144 gives a $(1 + \cos(\varphi + \delta\varphi(t)))$ dependence. Hence, with the assumption that $\delta\varphi(t)$ is much smaller than 1 this dependence can be approximated by $(1 + \cos(\varphi) + \sin(\varphi)\,\delta\varphi(t))$. Thus, Eq. 144 can be written as:

$$I_{photo} \sim 2|E_0|^2 \left(1 + \cos(\varphi) + \sin(\varphi)\,\delta\varphi_{max} \sin(2\pi f_{mod} t)\right). \qquad (145)$$

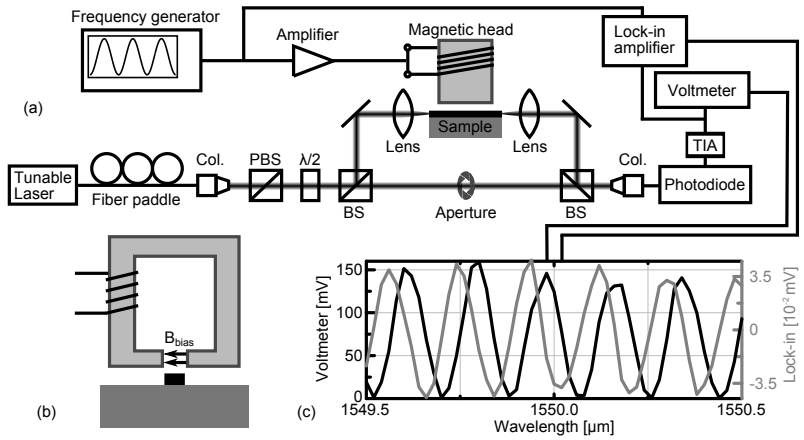

Figure 47: (a) Measurement setup. Col.: collimator, which transforms the fiber mode into a freespace beam, PBS: polarizing beam splitter, $\lambda/2$: half-wave plate, BS: beam splitter, TIA: transimpedance amplifier, which gives a voltage signal proportional to the photocurrent for the lock-in amplifier and voltmeter. The aperture in the reference arm is used to level the signals in both arms. (b) Cross-section of waveguide and magnetic head. (c) Sample measurement data. The magneto-optical phase shift can be derived from the ratio of lock-in to voltmeter signal.

The voltmeter acts as a low-pass filter, which cannot follow the modulation with f_{mod}. The measured voltage will therefore be proportional to $V_{VM} \sim 1 + \cos(\varphi)$. The lock-in amplifier is a band-pass filter centered around f_{mod} and its signal will be proportional to the last term in Eq. 145, $V_{LI} \sim \sin(\varphi)\,\delta\varphi_{max}$. The phase φ changes with the wavelength λ according to $\frac{2\pi}{\lambda}\Delta L$, where ΔL is the optical pathlength difference between reference and sample arm. If the wavelength is tuned in a small range, V_{LI} and V_{VM} have a sinusoidal wavelength dependence as can be seen in Fig. 47b. We can conclude from the given proportionality relations that the ratio of maximum lock-in signal to the maximum voltmeter signal is

The measured signals are voltages and not currents, because the transimpedance amplifier gives a voltage proportional to the photocurrent.

$$\frac{V_{LI}|_{max}}{V_{VM}|_{max}} = \frac{\delta\varphi_{max}}{2}, \tag{146}$$

In [127, 129] the effective value of the lock-in voltage is used and eq. 146 features an additional factor of $\sqrt{2}$.

which can be used to calculate $\delta\varphi_{max}$. The factor $\frac{1}{2}$ originates from the fact that the voltmeter signal is offset to have its minimum at 0 V. The phase shift can be related to material properties via $\delta\varphi_{max} = \delta\beta_{MO}L$ and equation 34. L is the length over which the magnetic field is applied to the waveguide.

Section 5.3 deals with the slightly more complicated case where the applied magnetic field is not constant over L.

The Faraday rotation that corresponds to the measured phase shift, $\delta\varphi_{max}$, can be found with perturbation theory. In the coordinate system of Fig. 48, where magnetic field is applied in x-direction and the wave travels along z-direction, equation 34 can be simplified to

$$\delta\beta_{MO} = \omega\varepsilon_0 \frac{\iint 2g\,\Im\left(E_z^* E_y\right)\mathrm{d}x\mathrm{d}y}{\iint \left(\mathbf{E}\times\mathbf{H}^* + \mathbf{E}^*\times\mathbf{H}\right)_z \mathrm{d}x\mathrm{d}y} \tag{147}$$

by rewriting the integrand in the numerator to

$$\mathbf{E}^* \Delta\varepsilon \mathbf{E} = \mathbf{E}^* \begin{bmatrix} 0 & 0 & 0 \\ 0 & 0 & jg \\ 0 & -jg & 0 \end{bmatrix} \mathbf{E}$$
$$= jgE_y^* E_z - jgE_z^* E_y = 2g\,\Re\left(-jE_z^* E_y\right) = 2g\,\Im\left(E_z^* E_y\right). \quad (148)$$

The required modal fields to calculate equation 147 can be obtained with the eigenmode solver described in Ref. [130]. The magneto-optical off-diagonal component g can be obtained by matching the experimentally found $\delta\beta_{MO}$ to the one obtained with equation 147. The off-diagonal component is in turn related to the Faraday rotation by $\Theta = \frac{180° g}{\lambda n}$.

5.2 MAGNETIC FIELD SHAPE

To conclude from $\delta\varphi_{max}$ the magneto-optical activity, the biasing magnetic field has to be known. Accordingly, we measured the field with a Hall probe. The sensor had a sensitive volume of $0.15 \times 0.01 \times 0.15\,\mathrm{mm}^3$ with a 0.1 mm thick housing on top which limits the minimal distance to the magnetic head for that the field could be evaluated. Fig. 48a shows a magnetic field measurement of the horizontal field component for the centre cross-section of the head. For the distances smaller than 0.1 mm a 2D FEM solver [131] was used to simulate the magnetic field. The measurement agrees reasonably well with the simulation close to head. On the surface of the magnetic head a field strength of 0.2 T can be produced. The divergence of the field in the horizontal direction can be used to adjust the magnetic head with respect to the waveguide. Fig. 48b shows the measured magneto-optical phase shift for a horizontal scan of the magnetic head. The phase shift is the largest if the gap is aligned with the waveguide.

Fig. 49 shows magnetic field measurements along the gap for various distances from the magnetic head. For small distances the field is nearly constant close to the centre and quickly decays when moving out of it. For larger distances the field distribution smooths and becomes more spread out.

5.3 MEASURING THE MO-EFFECT OF SILICON

A with distance varying divergence of the magnetic field in gap direction as shown in Fig. 49 can be used to assess the height of the magnetic head above waveguide and with that the magnetic field that is applied to it. Because the applied magnetic field along the waveguide is not constant, the contribution to the overall phase shift

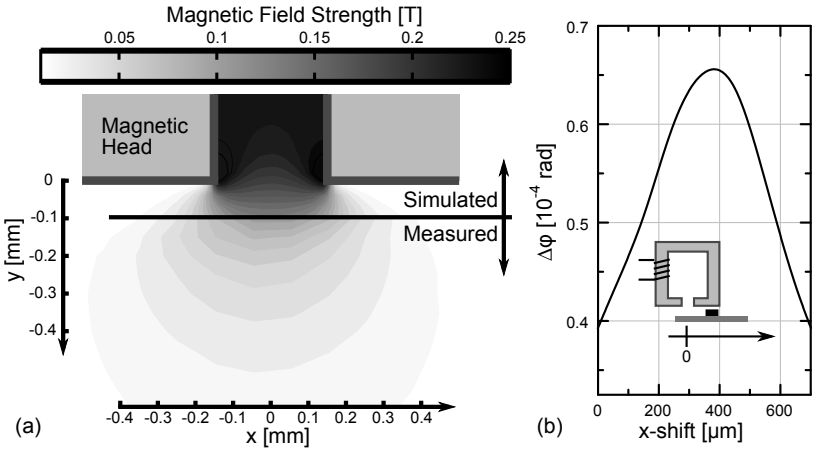

Figure 48: (a) Magnetic field measurement in x-direction. For distances larger than 100 µm the field was measured with a Hall probe. For smaller distances the field was simulated with a 2D FEM solver [131]. (b) Magneto-optical phase shift for a scan of the magnetic head in x-direction.

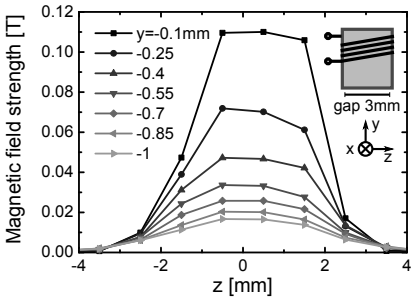

Figure 49: Measurement of the magnetic field strength in x-direction for various heights y along the gap in z-direction.

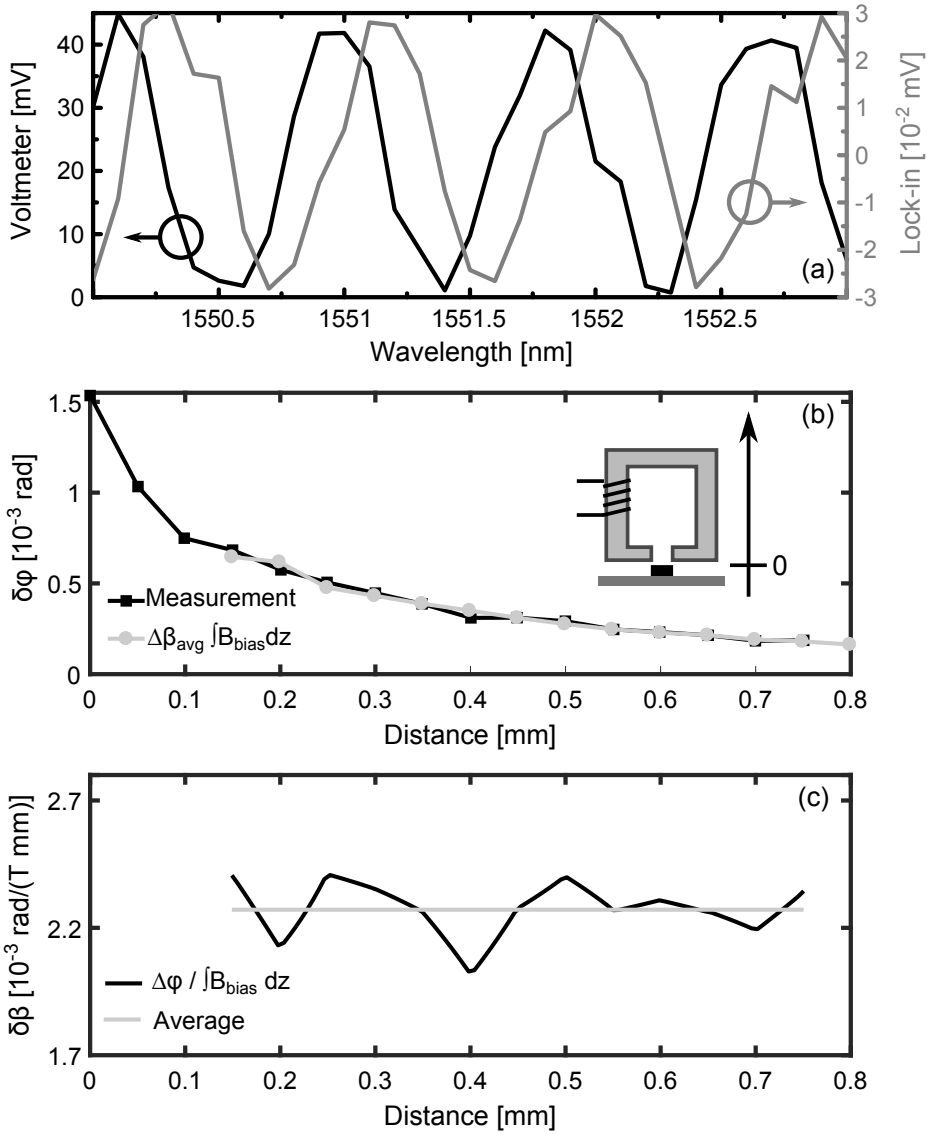

Figure 50: (a) Measurement for the case that the magnetic head is at its lowest position. (b) Measurement of the magneto-optical phase shift of a 500 nm × 220 nm silicon waveguide for various distances between the magnetic head and the waveguide. Further, the product of the found magneto-optical change in propagation constant with the integral of the biasing field. (c) Ratio phase shift and integral over biasing field as well as average, which is the shift in propagation constant.

will vary over distance and the phase shift needs to be obtained via integration:

$$\delta\varphi(y) = \int_0^L \delta\beta B_{bias}(y,z)\, dz = \delta\beta \int_0^L B_{bias}(y,z)\, dz, \qquad (149)$$

where $\delta\beta$ is the magnetic field-dependent change in propagation constant. The biasing field $B_{bias}(y,z)$ is integrated over the waveguide length L. The coordinates are defined as in Fig. 48 and 49. Because $\delta\beta$ is only dependent on the geometry of the waveguide cross-section, which does not change along the z-direction, it can be pulled in front of the integral, meaning that $\delta\beta$ is the ratio of the measured phase shift to the integral of the biasing field over the waveguide length. However, the quantities are obtained from two separate measurements; $\delta\varphi(y)$ is obtained from an experiment as described in Fig. 47 and $B_{bias}(y,z)$ is obtained from a measurement as done in Fig. 49. This makes it difficult to precisely control the height y such that it is exactly the same for both experiments. Providentially, the unknown height can be remedied by utilizing the fact that $\delta\beta$ is also independent of the height y and must be the same for measurements at various heights y_n. Accordingly, the integral over the biasing field and the magneto-optical phase shift can be evaluated for various magnetic head heights and the right relative position of the two can be found by shifting both curves with respect to each other and calculating the ratio $\delta\beta(y) = \delta\varphi(y+\Delta y) \,/\, \int_0^L B_{bias}(y,z)\, dz$. The correct relative shift Δy is the one for which $\delta\beta(y)$ becomes constant or for a real measurement with noise has the minimal spread. In the latter case the change in propagation constant can be found by averaging, $\delta\beta_{avg} = \langle\delta\beta(y)\rangle$. This was done in Fig. 50 for a 500 nm × 220 nm silicon waveguide on a silica substrate. In part (b) of the figure the measured magneto-optical phase shift is shown as well as the product of $\delta\beta_{avg}$ and the integral over the biasing magnetic field. The two curves are nearly identical as expected from Eq. 149. Fig. 50c shows the spread of $\delta\beta(y)$ as well as the average, $\delta\beta_{avg}$. The found change in propagation constant is $2.27 \times 10^{-2}\, 1/(\mathrm{T\ cm}) \pm 10\%$. Assuming the refractive index of silicon to be 3.5, that of silica to be 1.45, the Verdet constant of silicon to be $15\,°/(\mathrm{T\,cm})$ [132] and that of silica to be $0.38\,°/(\mathrm{T\,cm})$ [133], the expected change in propagation constant is $\delta\beta_{sim} = 2.2 \times 10^{-2}\, 1/(\mathrm{T\ cm})$ which agrees very well with the constant found in experiment. The simulated change in propagation constant was calculated with equation 34.

5.4 POLYTHIOPHENES

The very promising Verdet constants obtained from thin film measurements of polytiophene films led us to try to reproduce these numbers in integrated silicon waveguides. For this we cooperated with the originators of the thin film studies ([79, 80, 84], see section 2.11.2)

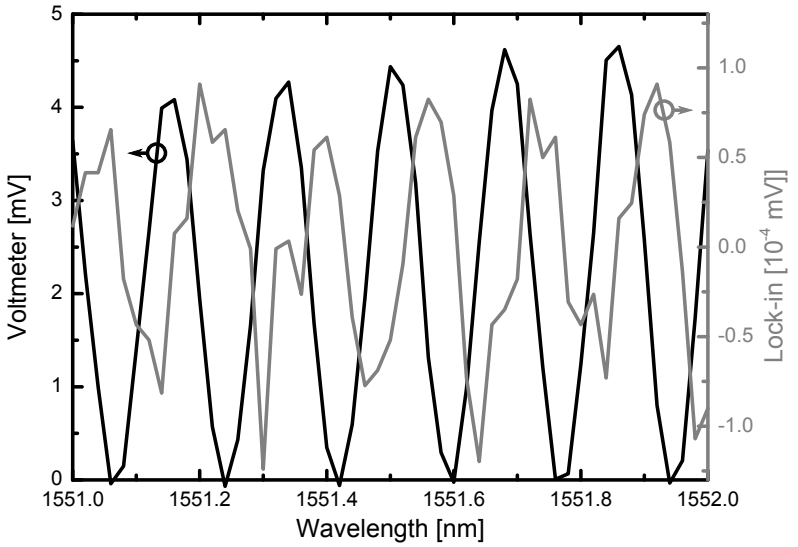

Figure 51: Magneto-optical phase shift measurement of a 3 µm × 220 nm SOI waveguide covered with a 150 nm film of poly(3-dodecylthiophene). The applied magnetic field is 0.2 T.

from the University of Arizona and the University of Leuven. The polymers were synthesized in Leuven and the film deposition was done in Arizona. Fig. 51 shows the magneto-optical phase shift measurement of a silicon waveguide covered with a 150 nm film of poly(3-dodecylthiophene). The phase shift is so small that the modulation signal is very noisy. The resulting phase shift is 5×10^{-5} rad which corresponds to a change in propagation constant of $\delta\beta = 1.67 \times 10^{-4}$ 1/cm. The Faraday rotation of the same material was previously measured by the University of Arizona in a thin film configuration on a silica substrate which yielded a Verdet constant of 415 °/(Tcm) at 1550 nm. Based on this value, the expected change in propagation constant of such a material is $\delta\beta = 5.17 \times 10^{-1}$ 1/cm. Therefore, the measured phase shift and the phase shift expected from the thin film measurement are three orders of magnitude apart. In fact, if one assumes that the polymer is completely magneto-optically inactive, the expected phase shift is $\delta\beta = 2.66 \times 10^{-4}$ 1/cm, which is very close to the measured one. The value is smaller than that of the silicon waveguide in the previous section for two reasons: Firstly, the waveguide is wider, which reduces the field at the surface of the waveguide. We can see from Fig. 17 that this area contributes the most to the phase shift. Secondly, using a polymer cladding instead of air makes the vertical refractive index profile more symmetric, which as well reduces the magneto-optical phase shift.

The material parameters for this calculation were that of the previous section. The refractive index of the polymer was 1.6.

We can give an upper estimate for the measured Faraday rotation by roughly determining the measurement sensitivity. If we assume that the measured $\delta\beta$ would have been ten times bigger than the actually measured value, i. e. 1.67×10^{-3} 1/cm instead of $1.67 \times$

10^{-4} 1/cm, it would correspond to a Verdet constant of 1.34 °/(Tcm). The measurement setup is clearly able to distinguish between the measured $\delta\beta$ and the assumed result. Thus, we can conclude that the measurement can at least resolve 1.34 °/(Tcm) in Faraday rotation and the value of the material must be below this value. As this is a very rough estimate of the measurement resolution, the actual $\delta\beta$ is likely to be even lower. We did also measurements on poly(3-alkoxythiophene)s. These, as well, yielded either intransparent films or null findings.

The discrepancy between the thin film and the waveguide measurement of at least two orders of magnitude is not understood just as origin of the Faraday rotation in polythiophenes is not understood.

5.5 MAGNETIC NANOPARTICLES

Besides polytiophene coatings, waveguide claddings made from polymer iron oxide nanoparticle composites were produced in cooperation with the University of Leuven and the University of Arizona. Fig. 52 shows the measurement of a 3 µm × 220 nm silicon waveguide covered with a composite consisting of polystyrene doped with 1 wt% Fe_3O_4-nanoparticles of 35 nm diameter. The composite was produced by the University of Leuven [134]. The measurement yielded a surprising result. Compared to Fig. 50 and 51, where voltmeter and lock-in signal are offset by a quarter period, in Fig. 52 the lock-in signal now follows the voltmeter signal. This indicates that for this sample there is amplitude instead of phase modulation.

The reason for this behaviour can be found revisiting the Zeeman splitting in Fig. 8. The magnetic field causes different permittivities for left hand and right hand polarized light. The difference in real part is responsible for Faraday rotation. The difference in imaginary part causes a biasing magnetic field-dependent difference in damping of a left- and right-hand polarized wave. For a linearly polarized wave which can be described as equal parts left- and right-hand polarized this difference in damping means that it is slowly turned into an elliptically polarized wave as one part decays stronger than the other. For this reason this effect is referred to as Faraday ellipticity [135]. The Faraday rotation becomes in this case a complex number, $\Theta + j\eta$. The real part indicates the rotation of polarisation and the imaginary part the ellipticity. A wave travelling in a waveguide with its circular polarized fields at the edges (Fig. 17) will feature a biasing magnetic field-dependent loss. Therefore, a waveguide with a cladding that features a small Faraday rotation but has considerable Faraday ellipticity will feature amplitude modulation for a varying biasing field as seen in Fig. 52a.

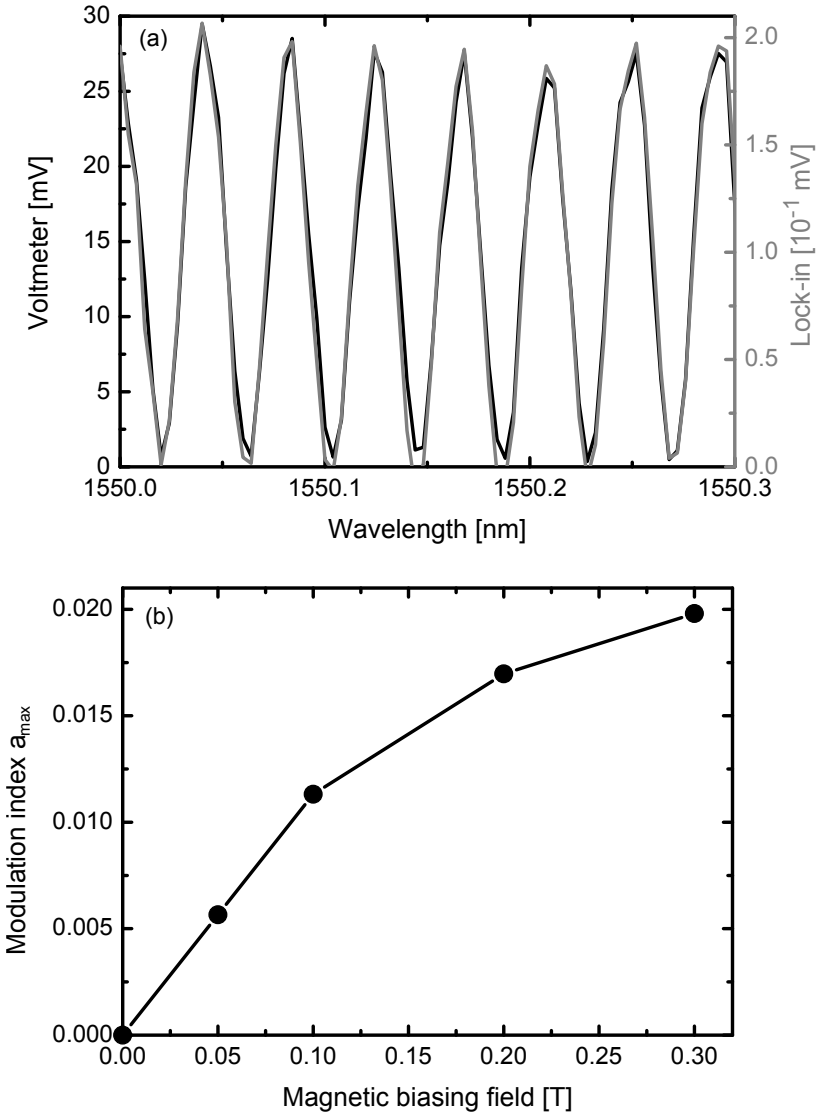

Figure 52: (a) Magneto-optical phase shift measurement of a 3 µm × 220 nm SOI waveguide covered with a several micron thick film of magnetite nanoparticles in polystyrene. (b) Modulation index as a function of biasing magnetic field.

The derivation of the phase shift in section 5.1 only needs to be slightly altered to produce the magneto-optical amplitude modulation. We start with the photocurrent which is now:

$$I_{photo} \sim |E_{MZI}|^2 = |E_{sample} e^{j\varphi - a(t)} + E_{reference}|^2. \tag{150}$$

Instead of the phase difference between reference and sample arm, here, the attenuation in the waveguide is modulated with the exponent $a(t)$. Just as in the previous case the modulation is sinusoidal, $a(t) = a_{max} \sin(2\pi f_{mod} t)$. By evaluating the absolute square in Eq. 150 and using $e^{-a(t)} \approx 1 - a(t)$ we obtain

$$I_{photo} \sim \left(2|E_0|^2 + 2|E_0|^2 \cos(\varphi)\right)\left(1 - a_{max} \sin(2\pi f_{mod} t)\right), \tag{151}$$

where we assumed that $E_{sample} = E_{reference} = E_0$. Equation 151 means that the low-pass-filtered voltmeter signal and the bandpass-filtered lock-in signal will be both proportional to $2|E_0|^2 + 2|E_0|^2 \cos(\varphi)$. We can conclude that

$$a_{max} = \frac{|V_{LI}|}{V_{VM}}. \tag{152}$$

In the same way that the magneto-optical phase shift is related to the Faraday rotation, the modulation index, a_{max}, is related to the Faraday ellipticity η. Just like for the polytiophenes we can derive η from a_{max} with the help of a perturbation integral similar to equation 34 and a mode solver. In this case the modulation index is equal to the product of the imaginary part of the perturbed propagation constant and the optical path length, $a_{max} = \delta\gamma L$.

In Fig. 52b the modulation index as a function applied magnetic field is shown. Because the magnetisation in the iron oxide particles saturates, the modulation index saturates as well. The saturation magnetic field strength agrees well with values found in literature [136–138]. The saturated index of $a_{max} = 0.02$ corresponds to $\delta\gamma = 0.067\,1/\text{cm}$. The off-diagonal component of the dielectric tensor is in this case a complex number, $\pm j(g + jh)$, where h is related to $\delta\gamma$ in the same way as $\delta\beta_{MO}$ is related to g:

$$\delta\gamma = \omega\varepsilon_0 \frac{\iint 2h\,\Im\left(E_z^* E_y\right) \mathrm{d}x\mathrm{d}y}{\iint \left(\mathbf{E} \times \mathbf{H}^* + \mathbf{E}^* \times \mathbf{H}\right)_z \mathrm{d}x\mathrm{d}y}. \tag{153}$$

The off-diagonal component h is related to the Faraday ellipticity by $\eta = \frac{\pi h}{\lambda n}$. The found $\delta\gamma$ corresponds to a $h = 1.18 \times 10^{-5}$, which corresponds to an ellipticity of $\eta = 0.15\,1/\text{cm}$. For the calculation of h the cladding refractive index was assumed to be that of polystyrene ($n = 1.57$). The influence of the iron oxide nanoparticles on the refractive index was neglected due to their low concentration.

In cooperation with the University of Arizona waveguides were covered with a PMMA cladding doped with 4 wt% cobalt ferrite particles of 20 nm diameter [96]. The resulting measurement at a biasing

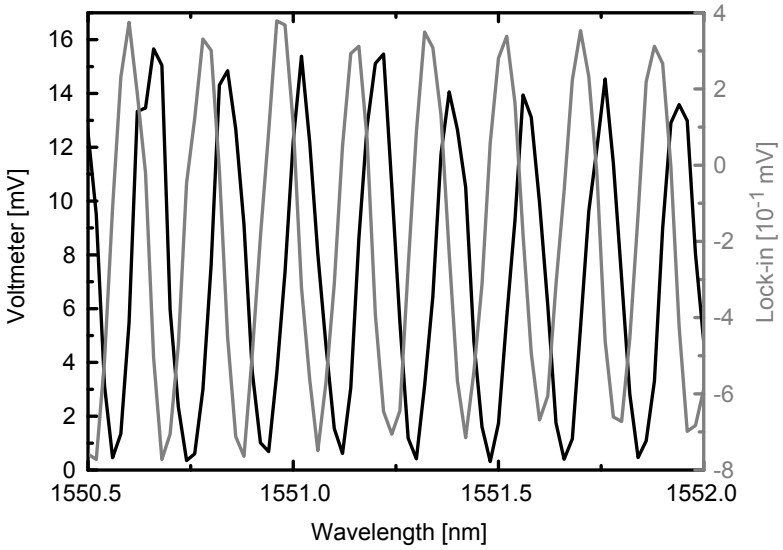

Figure 53: Magneto-optical phase shift measurement of a 3 µm × 220 nm SOI waveguide covered with a several micron thick film of cobalt ferrite nanoparticles in PMMA for a biasing field of 0.2 T.

field of 0.2 T is shown in Fig. 53. Compared to the previous measurements, the lock-in signal is neither proportional to the voltmeter signal nor is it shifted by a quarter period with respect to the latter, since this cladding features Faraday rotation and ellipticity in the same order of magnitude. The approach to obtain both ellipticity and rotation is the same as for the previous samples. We start by modelling the time dependence of the photocurrent:

$$I_{photo} \sim |E_{MZI}|^2 = |E_{sample} e^{j(\varphi+\delta\varphi(t))-a(t)} + E_{reference}|^2, \tag{154}$$

which features now both an amplitude as well as a phase modulation. In the same way as for equations 145 and 151 we can rewrite the photocurrent to

$$\begin{aligned} I_{photo} \sim\ & 2|E_0|^2 \left(1+\cos\left(\varphi\right)\right) \\ & + 2|E_0|^2 \left(\sin\left(\varphi\right)\delta\varphi_{max} - \cos\left(\varphi\right) a_{max} - a_{max}\right) \sin\left(2\pi f_{mod} t\right) \\ & - |E_0|^2 a_{max} \sin\left(\varphi\right)\delta\varphi_{max}\ \sin^2\left(2\pi f_{mod} t\right). \end{aligned} \tag{155}$$

The proportionality of the low-pass-filtered voltmeter signal is the same as in the previous cases. Additionally, there is a sine-square-dependent term. It can be neglected because it gives a negligible contribution to the voltmeter signal and a signal at the second harmonic of the modulation signal which is filtered out by both voltmeter and lock-in. In this case the lock-in signal is proportional to $V_{LI} \sim \sin\left(\varphi\right)\delta\varphi_{max} - \cos\left(\varphi\right) a_{max} - a_{max}$, which can be rewritten to $V_{LI} \sim -\sqrt{\delta\varphi_{max}^2 + a_{max}^2} \sin\left(\varphi + \arctan\left(\frac{\varphi_{max}}{a_{max}}\right)\right) - a_{max}$. This means the lock-in signal is a sinusoidal function with an offset proportional

to a_{max} and an amplitude proportional to $\sqrt{\delta\varphi_{max}^2 + a_{max}^2}$. Knowing this we can conclude:

$$\frac{2V_{LI}|_{offset}}{V_{VM}|_{max}} = -a_{max} \tag{156}$$

and

$$\frac{2V_{LI}|_{amp}}{V_{VM}|_{max}} = \sqrt{\delta\varphi_{max}^2 + a_{max}^2}. \tag{157}$$

From these two equations the magnitude of amplitude and phase modulation can be obtained. For the measurement in Fig. 53 this yields $a_{max} = 0.025$ and $\delta\varphi_{max} = 0.057\,\text{rad}$. These values correspond to a change in damping constant of $\delta\gamma = 0.084\,1/\text{cm}$ and a change in propagation constant of $\delta\beta = 0.19\,1/\text{cm}$. These constants result in $h = 1.45 \times 10^{-5}$ and $g = 3.27 \times 10^{-5}$ as well as a Faraday ellipticity of $\eta = 0.2\,1/\text{cm}$ and a rotation of $\Theta = 25.66\,°/\text{cm}$ at 1.55 µm. A thin film measurement of the same material was conducted by the University of Arizona. It yielded a Faraday rotation of $\Theta = 12\,°/\text{cm}$. The deviation might be explained by an increased particle concentration at the waveguide surface due to sedimentation. The thin film experiment measures the average Faraday rotation and is therefore not sensitive to a redistribution of the nanoparticles, whereas the waveguide experiment is exclusively sensitive in the volume close to the waveguide surface. These particles showed the same saturating magnetic field dependence with roughly the same saturation value as the magnetite particles which again agrees with previous findings [96].

For the calculation of g and h the composite refractive index of $n = 1.48$ was assumed.

5.6 YTTRIUM IRON GARNET

In cooperation with the University of Augsburg, yttrium iron garnet was deposited via pulsed laser deposition on top of silicon waveguides [139]. Fig. 54a shows magneto-optical phase shift measurement. There is a little more noise in the signal compared to the previously shown measurements because only part of the waveguide was covered and the transition from covered to uncovered waveguide caused reflections. The saturated phaseshift is $\delta\varphi_{max} = 0.045\,\text{rad}$, which corresponds to a change in propagation constant of $\delta\beta = 0.17\,1/\text{cm}$. Assuming a YIG refractive index of $n = 2.19$, the propagation constant can be linked to an off-diagonal tensor component of $g = 2.52 \times 10^{-4}$ and a Faraday rotation of $\Theta = 134\,°/\text{cm}$. This value is roughly half of what has been achieved with single crystal YIG substrates but agrees well with the value obtained for pulsed laser-deposited thin films [140]. Polycrystallinity and an incomplete crystallisation are reasons for the reduced Faraday rotation [140]. Unfortunately, these very promising results could not be reproduced. Subsequent samples yielded intransparent waveguides. The uncontrolled parameters that led to the inconsistency in film quality could not be

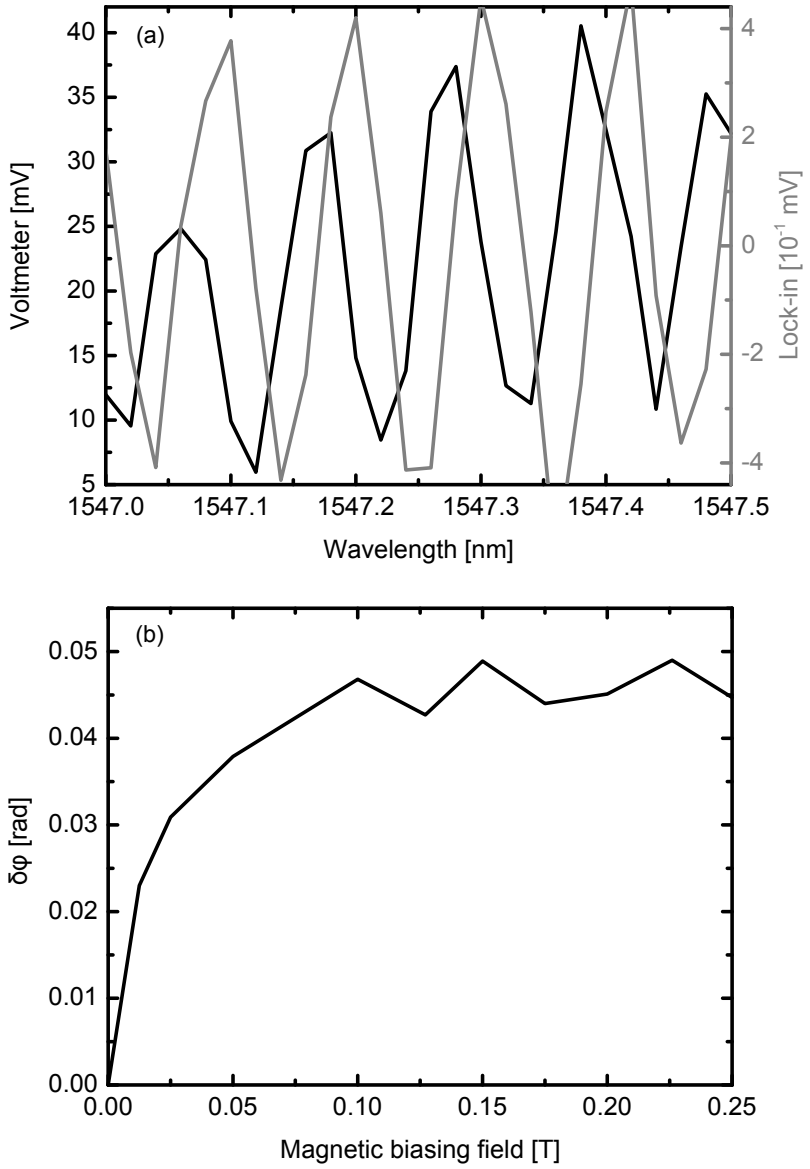

Figure 54: (a) Magneto-optical phase shift measurement of a 3 µm × 220 nm SOI waveguide covered with a 30 nm film of YIG. The biasing field is 0.2 T. (b) Phase shift versus biasing field.

identified within the running time of this project. Possible factors are the sample temperature during deposition, the ambient conditions during the subsequent annealing of the film or inconsistencies within the deposition target [139].

5.7 ARE THE MEASURED EFFECTS SUFFICIENT FOR THE PROPOSED DEVICES?

Now we want to find out whether the measured magneto-optical phase shifts are sufficient for the applications proposed in the previous chapters. In summary, we have presented an isolator in section 2.14.2.2, the reduction of backscattering in section 3.3, resonance suppression in section 3.4 and finally a circulator in chapter 4. The performance of all of these applications is governed by two factors: the intrinsic quality factor of the ring resonator, Q_i, and the magneto-optical frequency splitting, Δf. We start by estimating the experimentally available intrinsic quality factor. The Q_i of a ring resonator can be calculated by

$$Q_i = \frac{\omega_0}{\alpha v_g}. \tag{158}$$

The damping constant for power ($P_{loss} = P_0 e^{-\alpha l}$) is due to three contributions: scattering losses due to sidewall roughness, bending losses and material absorption, $\alpha = \alpha_{sc} + \alpha_{bend} + \alpha_{mat}$. Further, ω_0 is the radial resonance frequency and v_g is the group velocity. Maybe surprisingly, the quality factor depends only on the damping constant and not on the resonator length, l. This means that although the larger of two resonators with identical damping constants would loose more power, both resonators would feature the same Q_i. This is because the quality factor is defined as $Q = \omega_0 \frac{\text{energy stored}}{\text{power loss}}$. Accordingly, the larger resonator stores more energy which cancels the larger power loss. The bending loss will exponentially decrease with radius. For this estimation, we simply assume that the radius is sufficiently large that bending losses can be neglected. The scattering loss due to sidewall roughness can be reduced by careful manufacturing but can never be fully avoided. Thus, based on current manufacturing properties we can find the ultimately possible quality factor by assuming a large ring resonator with sidewall scattering but made from non-absorbing materials.

The state of the art propagation loss is 2.7 dB/cm [141]. This corresponds to $\alpha_{sc} = 62.21/\text{m}$. If we further assume that $v_g = c_0/4$ as we already assumed in the derivation of equation 72 and that the resonator is at resonance at $\omega_0 = 2\pi \times 193.5\,\text{THz}$, we obtain an intrinsic quality factor as high as $Q_i = 260000$. Depending on the exact group velocity of the resonator mode, this number can slightly vary, but we are here only interested in an order of magnitude estimation. Using smaller rings or introducing lossy materials will reduce this number.

	Phase shift $\delta\beta$	Frequency splitting Δf
Silicon	$2.27 \times 10^{-2}\,\mathrm{cm}^{-1}$	54 MHz
Polythiophenes	$8.35 \times 10^{-4}\,\mathrm{cm}^{-1}$	1.9 MHz
Nanoparticles	$1.9 \times 10^{-1}\,\mathrm{cm}^{-1}$	453 MHz
YIG	$1.7 \times 10^{-1}\,\mathrm{cm}^{-1}$	406 MHz

Table 2: Measured phase shift and corresponding frequency splitting. For silicon and the thiophenes a biasing field of 1 T is assumed, for the other two materials the saturation magnetization is considered.

In the following, we will consider two different rings with quality factors of 20000 and 260000. The former is what is typically achieved for ring resonators with magneto-optical cladding [25, 27] and latter serves as an ultimate example of what is possible.

The frequency splitting available with materials at hand can be calculated from the magneto-optical phase shift, $\delta\beta$, measured as described in the previous sections. From equation 73 we know that $\Delta f = v_g \delta\beta/\pi$. As with the quality factor, the exact phase shift and corresponding frequency splitting will depend on the exact waveguide shape and the mode used, but the phase shift, that is ultimately possible with these materials, will not be orders of magnitude away from what we measured. Table 2 summarizes the measured magneto-optical phase shifts and the corresponding frequency splittings. As mentioned in section 5.4, the value for the phase shift and frequency splitting of the polythiophene-coated waveguide is most likely not due to the polythiophenes but due to the silicon in the waveguide core. It is lower than the value for the silicon waveguide with air on top because the polymer on top yields an almost symmetric mode profile (section 2.12.2).

Now that we have collected all the information on quality factor and frequency splitting, we can investigate the possible performance of our four applications. We start with the isolator. The two characteristic parameters are insertion loss and bandwidth. Both can be derived from equations 77–79. The insertion loss is $IL_{iso} = \frac{\delta\omega^2+\gamma_i^2}{\delta\omega^2}$ and for $\gamma_i \gg \delta\omega$ the isolation bandwidth is approximately $\Delta f_{IBW,iso} = \Delta f \frac{2\sqrt{I}}{1-I}$. Accordingly, for small $\delta\omega$ the bandwidth is independent of the intrinsic resonator quality factor and only dependent on the frequency splitting. The resulting device performance for the quality factors and the respective materials can be found in table 3. While the isolation bandwidth of the ring with $Q_i = 20000$ might be something that can be usable for a few applications, the insertion loss for these materials is absolutely unacceptable for any reasonable device. The larger Q_i in 3b improves the insertion loss coming close to something that could be potentially of use in case of the nanoparticle and YIG-cladding, but due to the high quality factor the coupling between

the ring and the waveguide will have to be adjusted very precisely making the production of such a device very challenging.

The next application for magneto-optically active ring resonators is the reduction of backscattering. The possible reduction can be gathered from equations 97 and 98 which gives $\rho_{red} = \frac{\gamma_i^2}{\gamma_i^2+\delta\omega^2}$. In table 3 we can see that for both rings this yields a probably not even measurable reduction except for the nanoparticles and YIG cladding combined with the high Q_i ring resonator. But even these two case do not yield practical results.

The level to which the resonance can be suppressed is encoded in equation 99. It depends on the resonance splitting, the internal and external quality factor and implicitly via the critical coupling condition 92 on the backscattering rate. In the current case, $Q_{cpl} \leq Q_i \ll f_0/\Delta f$ holds true such that we can simplify equation 99 to $T^2 = \left(\frac{\Delta f}{f_0}\right)^2 \left(\frac{Q_{cpl}\left(Q_i - Q_{cpl}\right)}{Q_i + Q_{cpl}}\right)^2$. As we want to suppress the resonance, the transmission T^2 should be as close to one, or equivalently 0 dB, as possible. The Q_{cpl} that maximizes the transmission for the given Q_i and Δf is then $Q_{cpl} = \left(\sqrt{2}-1\right) Q_i$. This is corresponding to a transmission of $T^2 = \left(17 - 12\sqrt{2}\right) \left(\frac{\Delta f}{f_0}\right)^2 Q_i^2$. As we can see from the table, the frequency splitting is equally insufficient as for the previous applications.

Finally, the circulator yields the same conclusion. The minimal frequency splitting to achieve critical coupling (equation 128 and 129) is 5.6 GHz for the low quality factor resonator and 430 MHz for the high quality factor resonator. Accordingly, the -20 dB isolation ratio is zero for all cases except for the nanoparticle cladding. This cladding yields a measurable response but as with the isolator it will be challenging to fabricate such a device due to the tight requirements on the coupling geometry.

In summary, the measured phase shifts are not sufficient to provide functional devices. We now want to evaluate whether we can obtain functioning devices with experimental realizations of magneto-optically active ring resonators found in literature. We examine three works. Firstly, Bi(2011) [25] is a silicon ring resonator with a Ce:YIG layer deposited via pulsed laser deposition. Secondly, Sun(2015) [142] is a ring resonator produced by the same group with the same method but the production was optimized to yield a higher intrinsic quality factor. And thirdly, Huang(2017) [27] is a ring resonator on which a Ce:YIG layer was bonded. The corresponding intrinsic quality factors and magneto-optical frequency splittings can be found in table 4a. The resulting hypothetical device parameters can be found in table 4b. Although Bi(2011) and Sun(2015) improve the device parameters compared to table 3, the values are still not at a practically usable level. Only Huang(2017) yields parameters that are of practical rel-

(a)		$Q_i = 20000$			
		Silicon	Thiophenes	Nanoparticles	YIG
Isolator	$\Delta f_{IBW,iso}$	11 MHz	0.4 MHz	92 MHz	82 MHz
	IL_{iso}	45 dB	73 dB	27 dB	28 dB
Backscattering reduction		-1.4×10^{-4} dB	-1.8×10^{-7} dB	-9.5×10^{-3} dB	-7.6×10^{-3} dB
Resonance suppression		−60 dB	−89 dB	−42 dB	−43 dB
Circulator $\Delta f_{IBW,circ}$		0 Hz	0 Hz	0 Hz	0 Hz

(b)		$Q_i = 260000$			
		Silicon	Thiophenes	Nanoparticles	YIG
Isolator	$\Delta f_{IBW,iso}$	11 MHz	0.4 MHz	92 MHz	82 MHz
	IL_{iso}	23 dB	51 dB	5.7 dB	6.4 dB
Backscattering reduction		-2.3×10^{-2} dB	-3.1×10^{-5} dB	−1.4 dB	−1.1 dB
Resonance suppression		−38 dB	−67 dB	−20 dB	−21 dB
Circulator $\Delta f_{IBW,circ}$		0 Hz	0 Hz	158 MHz	0 Hz

Table 3: Device parameters achievable with the materials presented in this chapter. (a) parameters for ring with $Q_i = 20000$ and (b) parameters for ring with $Q_i = 260000$.

evance. The important distinction is that the garnet is not directly grown onto the silicon and can therefore be single-crystalline, which yields a stronger magneto-optical activity and lower losses. As discussed in section 4.6, we can see that our circulator design yields the better isolation bandwidth compared to a ring coupled to a single waveguide. For the same ring we see an eight times larger bandwidth. An interesting aspect of Huang(2017) is that the magnetic field to bias the garnet is produced by an electrical current. Such an arrangement is immediately capable of the switching properties aimed at with the resonance suppression. The needed current is in this case around 100 mA. A lower current would be possible if one could further improve the magneto-optical activity of the material or the quality factor of the ring resonator.

(a)	Bi(2011) [25]	Sun(2015) [142]	Huang(2017) [27]
Intrinsic quality factor Q_i	11000	90000	22500
Frequency splitting Δf	2.3 GHz	1.2 GHz	40 GHz

(b)		Bi(2011) [25]	Sun(2015) [142]	Huang(2017) [27]
Isolator	$\Delta f_{IBW,iso}$	0.48 GHz	0.21 GHz	1.7 GHz
	IL_{iso}	18 dB	6 dB	0.2 dB
Backscattering reduction		−0.07 dB	−1.2 dB	−13.5 dB
Resonance suppression		−33 dB	−21 dB	−6.8 dB
Circulator $\Delta f_{IBW,circ}$		0 Hz	0 Hz	13.9 GHz

Table 4: Device parameters achievable with resonators presented in literature.

5.8 CHAPTER SUMMARY

- In order to measure small magneto-optical phase shifts, we presented a method based on a modulated magnetic biasing field.
- The method is capable of resolving the magneto-optical phase shift of silicon.
- Polythiophenes deposited on silicon waveguides showed no measurable magneto-optical response.
- Magnetic nanoparticles showed Faraday rotation as well as ellipticity.
- The deposition of YIG onto silicon waveguides showed phase shifts which could have been promising in combination with another garnet with larger Verdet constant but the result could not be reproduced.
- The magneto-optical phase shifts produced by all three investigated materials is not sufficient for the devices presented in the earlier chapters.
- Of all the systems presented in literature only ring resonators bonded to iron garnets show a sufficient quality factor and magneto-optical frequency splitting to realize our proposed devices.
- Using our circulator design in chapter 4 we can increase the isolation bandwidth by a factor of 8 compared to already existing designs.

Reciprocity in daily life VI: Nonreciprocal attention

6

ALL-SILICON FARADAY ROTATORS

We propose a novel concept for a Faraday rotator which utilizes silicon as a sole magneto-optical active material. Although silicon has a Faraday rotation two orders of magnitude smaller than commonly used materials, its extremely low losses in the NIR allow for long device lengths. To keep the footprint small, we present a concept for wrapping up the Faraday rotator in a spiral fashion. 180° phase shifters are proposed to allow continuous accumulation of the Faraday rotation in a folded waveguide.

Contents

Material	Faraday Rotation [deg/cm]	Losses [dB/cm]	FoM [deg/dB]
CeYIG	-3300 [68]	5.8 [68]	570
γ-Fe_2O_3	25000 [98]	3.5×10^5 [100]	0.07
Orthoferrites	~500 [143]	<2 [144]	>250
$CoFe_2O_4$ nanoparticles	310 [95]	130 [95]	2.4
Silicon	15 [132]	7.4×10^{-3}[145]	2030

Table 5: Comparison of typical magneto-optical materials [73] with silicon. All values are given for a wavelength of 1.55 µm. The saturated Faraday rotation is given, except for silicon which Faraday rotation is proportional to the applied magnetic field in the feasible field range and which rotation is given for a field of 1 Tesla. To estimate the silicon losses we have assumed a typical residual impurity concentration of $10^{15}\,cm^{-3}$. The resulting damping coefficient was interpolated from experimental data given in Ref. [145].

6.1 INTRODUCTION

The previous chapter has shown that it is very difficult to introduce materials with strong magneto-optical activity into integrated photonic circuits. Either these materials show a very low effect or too high optical losses or they pose other problems like the crystal lattice mismatch between silicon and the magneto-optical material. Table 5 shows some of commonly investigated magneto-optically active materials [73]. In contrast to these materials, silicon shows very low optical losses and features a figure of merit (FoM) which is 4 times larger than the best magneto-optically active materials. The FoM is defined as the ratio of Faraday rotation to loss factor. Despite this much better ratio, silicon is usually not considered as a candidate for magneto-optical material. The reason for this is the relatively low Faraday rotation and that in order to achieve a reasonable rotation a relatively strong magnetic bias field is needed. However, silicon has a Faraday rotation which is only 1 to 2 orders of magnitude lower than that of commonly used materials. In view of the severe problems that these materials pose to the on-chip integration of non-reciprocal devices, it is worth investigating the potential of silicon for this application.

6.2 MAGNETO-OPTICAL PHASE SHIFT OR FARADAY ROTATION?

The magneto-optical activity of silicon can be exploited through either of two effects: the magneto-optical phase shift or Faraday rotation. Upon deciding which is the more appropriate it is important to know that silicon is usually the material with the highest refractive index used in integrated photonic systems and therefore serves as wave-

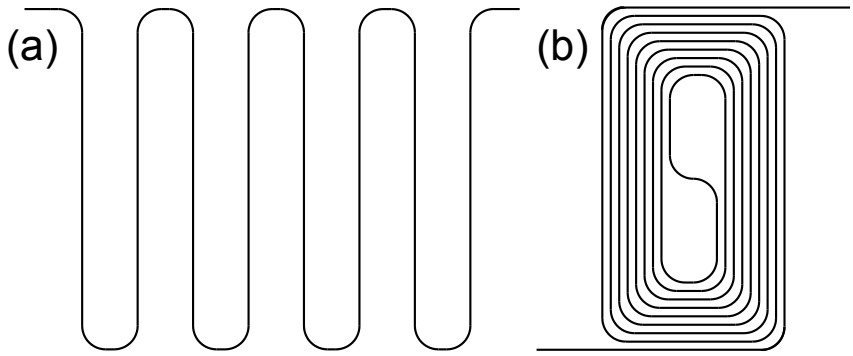

Figure 55: Possible ways to wrap up a photonic waveguide: (a) in meander form, (b) in spiral form.

guide core material. The high index contrast between silicon in the core and the cladding materials such as silica ensures that the optical wave is to a large part concentrated in the silicon. This is very advantageous for many applications as it ensures compact dimension and high optical field strengths. However, for the usage of the magneto-optical phase shift it is disadvantageous. In this case a strong asymmetry in the electro-magnetic field distribution is needed (see section 2.12.2 or [19]). But because the field is concentrated in the silicon, the field distribution is very symmetric and the magneto-optical phase shift is very small. Faraday rotation is not limited by the need of a strong asymmetry and for this reason we will investigate in the following the potential of silicon waveguides as Faraday rotators.

6.3 WRAPPING UP FARADAY-ROTATING WAVEGUIDES

To use a silicon waveguide for an optical isolator, one needs 45° Faraday rotation accumulated over the length of the waveguide [18]. If one assumes for simplicity that the field is completely confined in the silicon, it would mean that the waveguide has to be 3 cm long if a 1 T magnetic biasing field is applied. Assuming a more realistic 0.25 T, our waveguide would have to be 12 cm long. These and much longer lengths are feasible with silicon waveguides [146, 147], but the form factor of such long straight waveguides might not be desirable and shortening of the lengths by meandering (Fig. 55a) or spiraling (Fig. 55b) the waveguide might be necessary.

To understand what bending does to a Faraday rotator, we will first discuss a commonly used straight Faraday rotator as depicted in Fig. 56a, where the waveguide is magnetically biased along its axis. To describe the polarization state, we need to define a coordinate system. This is arbitrarily chosen such that $\mathbf{e}_y$ is always vertical and $\mathbf{e}_x = \mathbf{k} \times \mathbf{e}_y$, where $\mathbf{k}$ is the wave vector of the light travelling in the waveguide. This definition implies that the coordinate system is relative to the wave vector and thus will change if the propagation

direction changes. If a wave is launched from the bottom into the waveguide with a polarization angle of 0°, the polarization will be rotated clockwise to 45° in this example. For the reversed direction (right side of Fig. 56a) the wave vector and bias field are opposing. With our definition of the coordinate system the initial polarization is now 135°. And the opposing bias field and wave vector cause the sense of polarization rotation now to be counter-clockwise. Thus the polarization is not rotated back to its input state but is rotated further to a polarization angle of 90°. This is a typical arrangement of an isolator based on Faraday rotation. The light reflected back into the output port is rotated by 90° with respect to input polarization and hence can be blocked by a polarizer.

In case the waveguide is bent, the Faraday rotator behaves differently as is shown in Fig. 56b. The waveguides before and after the bend Faraday rotator behave analogous to the straight waveguide with the left arm in Fig. 56b behaving like the forward travelling case in Fig. 56a and the right arm like the backward travelling case. The one difference is that the bend preserves the polarization state with respect to the wave vector and does not mirror it. From this follows that the right arm will reverse the Faraday rotation of the left arm such that the net rotation is zero. To have a non-zero Faraday rotation in a bend waveguide, the bend has to mirror the polarization. This can be done by introducing birefringence into the bend as shown in Fig. 56c. Here, the vertical and horizontal polarization are phase-shifted with respect to each other by 180°, which makes the case of Fig. 56c analogous to Fig. 56a.

6.4 MULTI-MODE WAVEGUIDE BENDS

In this and the following sections we will elaborate a design using the above mentioned concept. The first choice we have to make is the waveguide profile. Most commonly, the silicon waveguide layer is 220 nm high and the waveguide width is adjusted such that there is only a single-mode for each polarization. We cannot use such waveguides for Faraday rotation. In Fig. 57a and b the quasi-TE and the quasi-TM modes of such a waveguide are depicted. The field distributions of both modes are very different which leads to strongly different propagation constants. This effect is referred to as form birefringence. But an efficient Faraday rotation is only possible if both modes have roughly the same propagation constant [19]. Another disadvantage of a single-mode waveguide is that a large part of the field is outside the silicon core where it cannot contribute to the polarization rotation assuming the surrounding material is inactive. This calls for a large and symmetric cross-section as depicted in Fig. 57c and d. For this $3\,\mu m \times 3\,\mu m$ waveguide the field is nicely

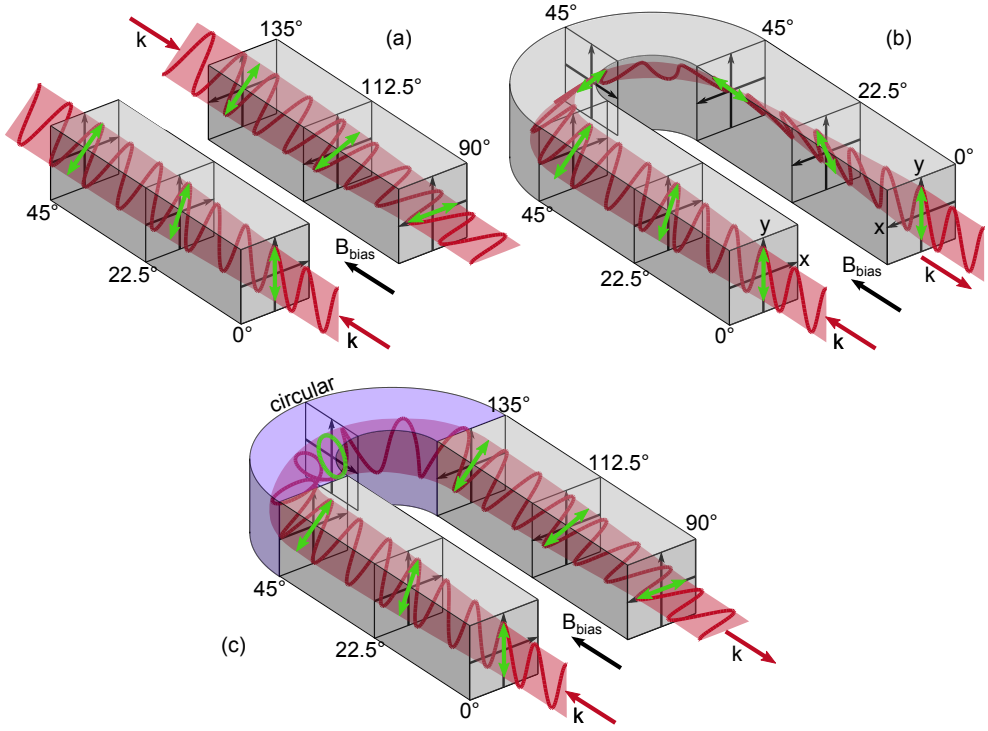

Figure 56: Evolution of the polarization for a folded Faraday rotator. (a) A standard Faraday rotator as used for an optical isolator. The left part depicts a wave travelling in forward direction; the right part shows a wave travelling in backward direction. (b) Two Faraday rotators that are connected by a bend that preserves the polarization state. The net Faraday rotation is in this case zero. (c) The same Faraday rotators as in (b) but now they are connected via a birefringent bend that accumulates 180° phase shift between the vertical and horizontal polarization. The polarization rotation in the two parts adds up in this case.

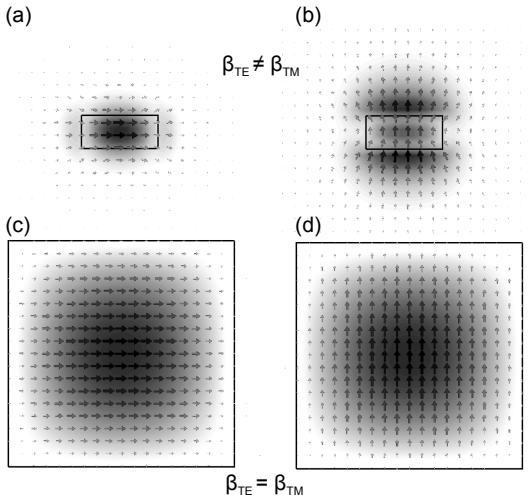

Figure 57: Form birefringence and electric fields for a single- and multi-mode waveguide with silicon core and silica cladding for $\lambda = 1.55\,\mu m$: (a) TE-mode for a $500\,nm \times 220\,nm$ single-mode waveguide and (b) TM-mode for the same waveguide. (c) TE-mode for a $3\,\mu m \times 3\,\mu m$ multi-mode waveguide and (b) TM-mode for the same waveguide.

confined in the silicon and the field distributions of the two modes look identical leading to identical propagation constants.

The large cross-section causes another problem: The waveguide allows for higher order modes beside the two fundamental modes. These higher order modes spoil the device functionality as a Faraday rotator, should they be excited. Two positions are critical in terms of higher order mode coupling: the bends and the coupling section from a free-space wave to the waveguide mode. The free-space coupling can be addressed by coupling into a ridge waveguide which only guides the two fundamental modes and then carefully transitioning into the multi-mode waveguide [148]. These single mode ridge waveguides ensure that the device can still work as an isolator as defined in section 2.3. In blocking direction the two fundamental modes are non-reciprocally rotated and can be blocked by a polariser. The higher order modes are blocked in both directions by the ridge waveguides. Thus all modes are blocked in one direction as needed for complete isolation. The issue of the coupling of modes in the bends was solved in Refs. [148–150]. Commonly, circular bending sections are used. This poses an abrupt change in curvature from zero in the straight section to $1/R$ in the bend section, where R is the bending radius. This transition causes the coupling to higher order modes. The most simple way to remedy this problem is making the bending radius so large that the curvature is negligible. For multi-mode waveguides with a micron-sized cross-section, this leads to bending radii of a few hundred micron [148]. A more elegant and compact way to design such a bend is to linearly increase the curvature. Such a bend will have the shape of the first section of a Euler spiral and is there-

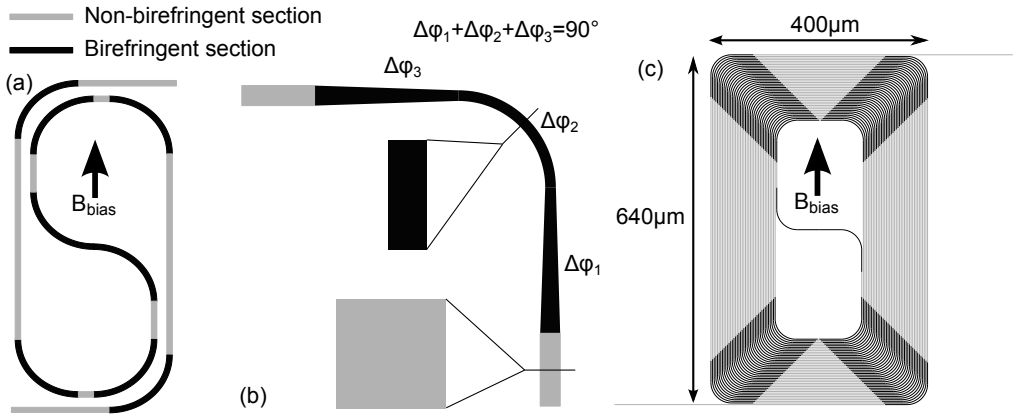

Figure 58: (a) Silicon Faraday rotator design. The non-birefringent square waveguide section is depicted in grey. The birefringent parts are depicted in black. (b) Layout of the birefringent section. The width is narrowed down, then follows an Euler bend and the waveguide is again widened. The grey part in (b) has a total birefringence of 90°. (c) Possible implementation of an integrated silicon Faraday rotator.

fore referred to as an Euler bend [148]. For such a curve there is a gradual change in curvature which significantly reduces the coupling to higher order modes. In Ref. [148] it was shown that for a waveguide cross-section of $2\times4\,\mu m^2$ the effective bending radius can be as small as 17.2 µm and the coupling to higher order modes may still be below 20 dB per bend.

6.5 DESIGN

Fig. 58 depicts a possible implementation of the presented design. The Faraday rotation is generated in the waveguide sections that are parallel to the biasing field. The needed 180° phase shift between the two orthogonal modes of each turn is achieved by two sections each adding 90° phase shift between the TE- and TM-mode. These two sections are connected with a non-birefringent waveguide which will not contribute to the Faraday rotation as the direction of wave propagation is orthogonal to the biasing field [19]. The birefringent section consists of three parts: a taper from the square waveguide cross-section to one with a large aspect ratio, an Euler bend and a taper back to the square cross-section. An Euler bend with large aspect ratio is for two reasons beneficial. Firstly, it creates the needed birefringence. Secondly, it allows for tighter bending radii. The reasons for this are that a more narrow waveguide will have less undesired modes that can be coupled and that a larger aspect ratio of the waveguide cross-section will increase the propagation mismatch between the modes and thus suppress coupling. Fig. 58c shows a possible implementation of such an integrated silicon Faraday rotator. With a 1 T biasing field the active waveguide section needs

to be in total 3 cm long to achieve the required 45° polarization rotation. The rotating sections have a 3 µm × 3 µm cross-section. The effective bending radius of the Euler bend was chosen to be 20 µm with a 1 µm × 3 µm waveguide cross-section. The tapers are 40 µm long. The total device has a footprint of only 640 × 400 µm^2, which is comparable to devices relying on iron garnets which use ring resonators ([25], 290 × 90 µm^2) and Mach-Zehnder interferometers ([151], 1500 × 4 µm^2, [152], 1160 × 260 µm^2). Despite the more than two orders magnitude smaller Faraday rotation of silicon compared to iron garnets, the iron garnet-based devices roughly cover the same area. The reason is twofold: Firstly, the iron garnet based isolators utilize silicon as the high index material for the waveguide core. The strongly magneto-optically active garnet is only used as cladding and, therefore, there is much less overlap of the optical field with the magneto-optically active material compared to the multi-mode silicon waveguide, where nearly all the field is concentrated in the magneto-optically active section. Secondly, the introduced technique of folding the Faraday rotator into a spiral or meander allows for much larger propagation distances per device area. Isolators based on ring resonators and Mach-Zehnder interferometers rely on the magneto-optical phase shift, which like the Faraday rotation cancels for a folded waveguide and a homogeneous field.

6.6 TOLERANCES

To ensure the functionality of the device, two questions are of importance: How much unwanted birefringence is allowed in the polarization rotating section and how accurately has the intended birefringence in the bend to be adjusted. The former constraint originates from the fact that a mismatch in propagation constant limits the maximum power that can be coupled from one mode to the other. The maximum efficiency can be calculated by [103]

$$\eta = \frac{|\kappa|^2}{|\kappa|^2 + |\frac{\Delta\beta}{2}|^2}, \tag{159}$$

where $\Delta\beta$ is the mismatch of propagation constants between the TE and TM mode and κ is the coupling constant between the two modes, which is for strong mode-overlap equal to the Faraday rotation given in rad/m. For an isolator the polarization needs to be rotated by 45°. This means that 50% of the power needs to be coupled from the TE to the TM mode or vice versa. Accordingly, η needs to be larger than 0.5. This constraint leads to an upper bound for the allowable birefringence of

$$|\Delta\beta| < |\kappa|. \tag{160}$$

For a silicon waveguide and a biasing field between 0.25 T and 1 T the coupling constant κ lies between 6.5 rad/m and 26 rad/m, which is hence also the upper bound for $\Delta\beta$. Although the birefringence in the waveguide in Fig. 57c and d is ideally zero, there might still be some birefringence due to stress and strain occurring in the manufacturing process. If this is the case, the birefringence has to be counteracted by a change of aspect ratio of the waveguide or by post-fabrication tuning described in the following section.

The accuracy with which the birefringence in the bend needs to be adjusted can be calculated in a similar fashion. One can define an effective birefringence of one Faraday section and a 180° bend

$$\Delta\beta_{eff} = \frac{N\pi - 2\Delta\beta_{EB}L_{EB} - 4\int \Delta\beta_T(l)\,dl}{L_{FR}}, \tag{161}$$

where $\Delta\beta_{EB}$ and L_{EB} are the birefringence and length of the Euler bend. Further, $\Delta\beta_T(l)$ is the length-dependent birefringence of the taper integrated over its length and $L_{FR}$is the length of the Faraday active section. The $N = 2n - 1$ with n being an integer accounts for the fact that the intended phase difference is allowed to be an uneven multiple of π other than $1 \cdot \pi$. The reasoning behind this effective birefringence is that as long as the Faraday rotation of each section is small, the deviation from 180° phase shift between TE- and TM-mode in the turn can be interpreted as a mode mismatch between the TE and TM mode in the polarization rotating section. Equation 159 and 160 are also valid for $\Delta\beta_{eff}$, yielding the same upper bounds. The fact that the length of the bending section occurs in the numerator and the length of the polarization rotating section occurs in the denominator means that the smaller the ratio of former to latter length is, the more relaxed the constraints for $\Delta\beta_{EB}$ and $\Delta\beta_T(l)$ will be. We want to estimate now the allowable error in birefringence. We simplify this estimation by defining an average birefringence for the whole section, $\Delta\beta_{bend}$, as $2\Delta\beta_{EB}L_{EB} + 4\int \Delta\beta_T(l)\,dl = \Delta\beta_{bend}(2L_{EB} + 4L_T)$. We further assume that $\Delta\beta_{bend} = \Delta\beta_{bend,designed} - \Delta\beta_{bend,error}$, where $\Delta\beta_{bend,designed}$ yields zero in equation 161 such that the remainder can be written as $\Delta\beta_{eff} = \frac{2L_{EB}+4L_T}{L_{FR}}\Delta\beta_{bend,error}$. For the design in Fig. 58c, the path length of the Euler bend is $L_{EB} = 33.6\,\mu m$ and the taper length is $L_T = 40\,\mu m$. The shortest active section in the centre of the spiral is 250 µm long. This means that $\Delta\beta_{bend}$ must be adjusted to an accuracy of 24 1/m for a 1 T biasing field. A design for lower biasing fields would yield even stricter requirements. For a $1\,\mu m \times 3\,\mu m$ waveguide profile, where the change of birefringence with width is $\frac{d\Delta\beta}{d\text{width}} = 188 \cdot 10^9\,1/m^2$ at 1.55 µm wavelength, this corresponds to an accuracy in width of 0.13 nm. This is not feasible with current fabrication techniques and calls for a post-fabrication trimming.

6.7 TUNING AND TRIMMING

For the post-fabrication trimming we present two mechanisms: tuning by temperature and trimming by oxidization. The former utilizes the fact that the refractive index of the silicon waveguide core and the silica cladding slightly change with temperature via the thermo-optical effect (TO). For silicon the TO coefficient, $\partial n/\partial T$, is $1.86 \cdot 10^{-4}\,1/\mathrm{K}$ [153, 154], for silica it is $1 \cdot 10^{-5}\,1/\mathrm{K}$ [155].

Silica and Silicon have different thermal expansion coefficients which induces stress into the silicon when the structure is heated up. This stress does in principle also change the refractive index. The effect can however be estimated to be at least two orders of magnitude lower than the TO effect. The thermal expansion coefficient of silicon is $\alpha_{Si} = 2.6 \cdot 10^{-6}\,1/\mathrm{K}$ [156] and that of silica is $\alpha_{SiO2} = 0.5 \cdot 10^{-6}\,1/\mathrm{K}$. If we assume as an upper estimate that the silica is much stiffer than the silicon, we can estimate the induced silicon stress per K as $\partial s/\partial T = E_{si}(\alpha_{Si} - \alpha_{SiO2})$, with $E_{si} = 160\,\mathrm{GPa}$ being the Young's modulus of silicon [157]. By multiplying the induced stress per K with the photoelastic coefficient $\partial n/\partial s = 12 \cdot 10^{-3}\,1/\mathrm{GPa}$ [158] we obtain the TO coefficient induced by mismatched thermal expansion between substrate and waveguide, $\partial n/\partial T|_{THEXP} = \partial n/\partial s \cdot \partial s/\partial T = 4 \cdot 10^{-6}\,1/\mathrm{K}$, which is a negligible correction to the already established TO coefficient.

The thermally slightly altered refractive index causes a change in birefringence that can be calculated with

$$\frac{d\Delta\beta}{dT} = \frac{\partial\Delta\beta}{\partial n_{Si}}\frac{\partial n_{Si}}{\partial T} + \frac{\partial\Delta\beta}{\partial n_{SiO2}}\frac{\partial n_{SiO2}}{\partial T}. \tag{162}$$

For the $1\,\mu\mathrm{m} \times 3\,\mu\mathrm{m}$ waveguide profile $d\Delta\beta/dT$ is $-5\,1/(\mathrm{m}\cdot\mathrm{K})$. For an adjustable temperature range of $\Delta T = 100\,\mathrm{K}$ the birefringence has a tuning range of $d\Delta\beta/dT \cdot \Delta T = -500\,1/\mathrm{m}$. Hence, one can compensate for a change in width of $500\,1/\mathrm{m} \cdot \left(\frac{d\Delta\beta}{d\mathrm{width}}\right)^{-1} = 2.66\,\mathrm{nm}$.

Larger errors in width can be compensated by oxidizing the outer part of the waveguide. For this approach, we omit the silica top cladding in the bend and gradually oxidize the surface of the waveguide (see Fig. 59). Only the open faces are oxidized. Thus the aspect ratio and with that the birefringence changes. For the waveguide in Fig. 59 this yields an oxide thickness-dependent change in birefringence of $d\Delta\beta/dw_{Oxide} = 377 \cdot 10^9\,1/\mathrm{m}^2$. This means that by oxidizing 50 nm of the outer silicon, one can compensate for an error in width of 100 nm, which is well within the limits of current manufacturing processes.

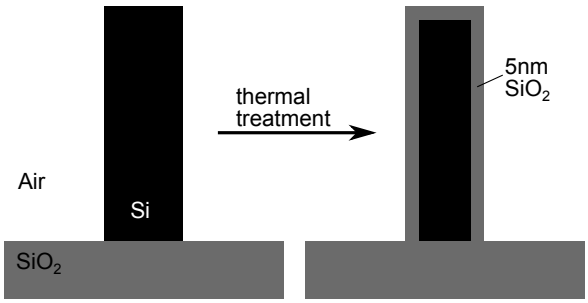

Figure 59: Tuning by oxidation: If the edge of the waveguide cross-section is oxidized, the aspect ratio changes slightly. This causes a change in birefringence.

6.8 CHAPTER SUMMARY

- Silicon has an outstanding figure of merit for magneto-optical applications.
- For compact devices the silicon waveguide needs to be spiralled in order to achieve the required propagation length.
- To enable continuous Faraday rotation for a spiralled waveguide, the bends need to feature a 180° phase difference between TE- and TM-mode.
- For efficient Faraday rotation, large 3 µm × 3 µm waveguides are employed.
- Compact bending radii without mode coupling are ensured by the utilization of Euler bends.
- Upper bounds for the allowable birefringence in the Faraday-active region and for the error in phase difference in the bend were given.
- Minor fabrication errors can be mitigated by temperature tuning.
- Larger fabrication errors can be corrected by post fabrication oxidization of the waveguide.

Reciprocity in daily life VII: Reciprocal dependence

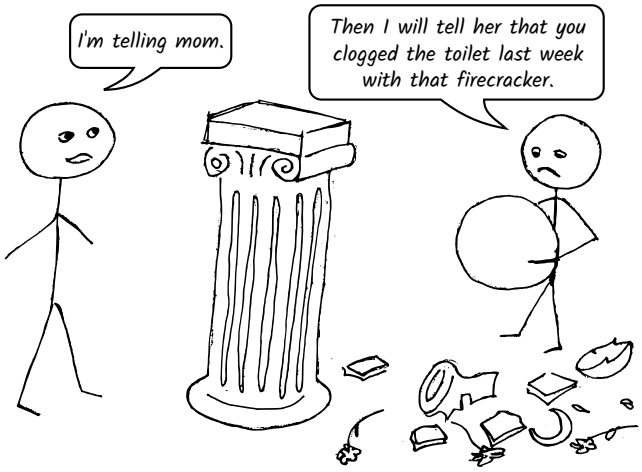

7

WRAPPING UP AND LOOKING FURTHER

7.1 CONCLUSION

In the preceding chapters we have explored new concepts pursuing the miniaturization of magneto-optical components. Such devices, especially isolators, have the potential for cost reduction in optical systems as they relax design requirements by suppressing unwanted back-reflections. Unfortunately, the underlying effects are quite weak requiring large interaction volumes which makes their introduction into integrated photonic platforms a difficult task.

Figure 60 summarizes the phenomena we exploited in this work. The magnetic field causes a difference in permittivity between a right-handed circularly polarized wave and a left-handed polarized one. This difference was used in two ways: Firstly, we made use of the fact that linearly polarized light is a superposition of right- and left-handed circularly polarized light. The difference in permittivity leads to a difference in propagation constants between the two circular states which, in turn, causes the linear polarization to rotate in a non-reciprocal way. Secondly, we used the electric field at the interface between core and cladding. This part of the waveguide mode is circularly polarized and also changes the handedness upon reversing the propagation direction. Hence, we see a direction-dependent propagation constant in asymmetric waveguides. If the waveguide is bent to a ring resonator, this yields a frequency splitting between the clockwise and the counter-clockwise travelling mode. A ring resonator with sufficiently high quality factor greatly enhances the light-matter interaction and therefore offers the possibility for device size reduction.

We have made use of the magneto-optical frequency splitting in three different ways summarized in figure 61. If such a ring resonator is coupled to a waveguide, it is on resonance only for one of the two directions of propagation and can therefore be used as an isolator (Fig. 61a).

Next, we added to the frequency splitting a competing effect (Fig. 61b). We coupled the clockwise and the counter-clockwise travelling mode by a corrugation of the ring's sidewall. This we used to two ends: The frequency splitting can suppress unwanted backscattering in case the sidewall corrugation is an unavoidable outcome of the fabrication process. A separation of the two ring modes in frequency will limit the fraction of energy that can be coupled from one mode to the other and thus limit the backscattering. The second way to

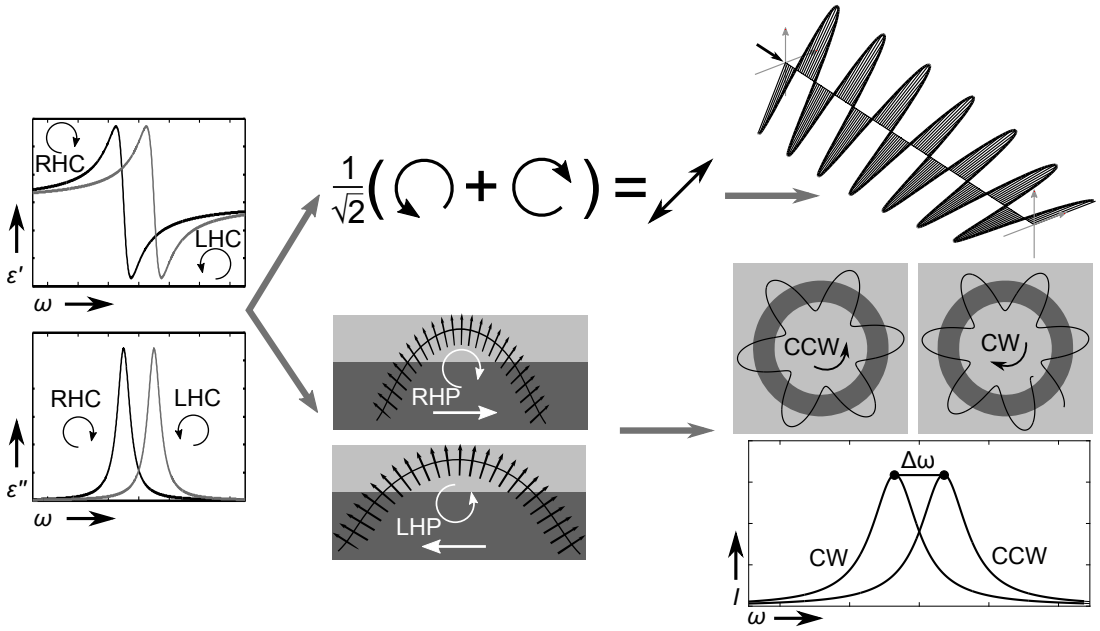

Figure 60: Summary of the employed physical phenomena. Upper arm: Faraday rotation. Lower arm: Magneto-optical phase shift and frequency splitting.

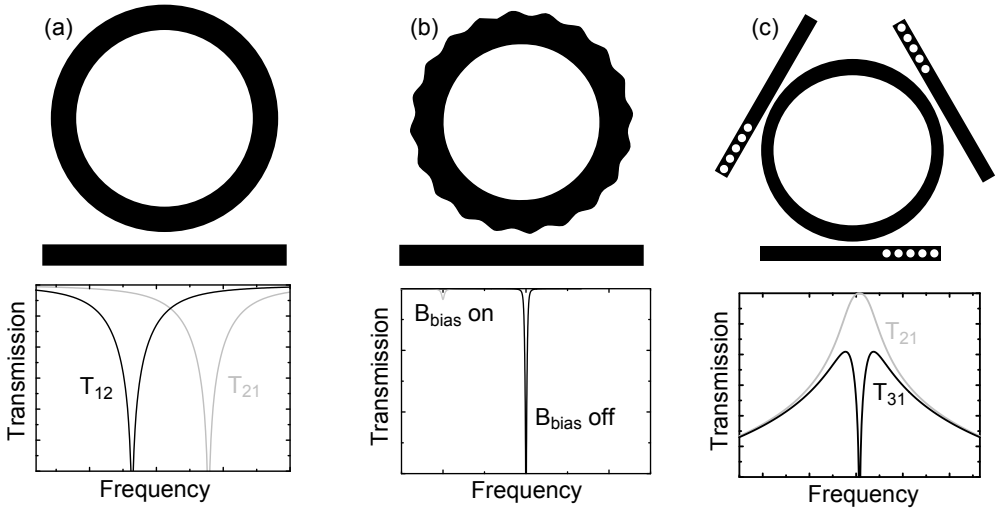

Figure 61: Devices based on magneto-optical frequency splitting and their respective transmission spectra. (a) The isolator from chapter 1. (b) The magneto-optical switch from chapter 3. (c) The circulator from chapter 4.

make use of coupling and frequency splitting is to functionalize the two effects as a magnetic bias-dependent switch. The critical coupling condition will depend on the coupling to the waveguide and the coupling between the two resonator modes. As the latter coupling process can be suppressed by frequency splitting, we can thereby violate the critical coupling condition and let the resonance disappear from the transmission spectrum.

The final device is shown in Fig. 61c. This device relies on an interference between the clockwise and the counter-clockwise mode. The threefold symmetry combined with the magneto-optical effect yields a circulator. We have shown that such an arrangement yields superior isolation bandwidth compared to the slightly simpler arrangement of a ring coupled to two waveguides. With sufficient frequency splitting the circulator can be even used as an isolator outperforming the ring coupled to a single waveguide in Fig. 61a.

On the experimental side of things, we have presented a method to measure magneto-optical phase shift in waveguides. The method is capable of resolving very small phase shifts, which unfortunately was also necessary as the investigated waveguide systems turned out to show only weak phase shifts, so weak that none of the presented devices are feasible with the material systems investigated. From magneto-optical ring resonators found in literature only Ref. [27] showed a sufficiently high quality and frequency splitting to yield practically interesting device parameters. The resonator in that study was bonded to a Ce:YIG garnet. While this production method gives the best device performance, it is at odds with the initial motivation to introduce isolators into integrated photonic systems: cost reduction. The process is difficult and needs bulky pieces of single crystalline garnets that cover a much larger area than just the magneto-optical device. The garnet thus takes up space for things that also need to be bonded to the photonic chip like sources and detectors.

Due to the difficulty of introducing magneto-optical materials into the integrated silicon photonic platform, we tried to go a different route in chapter 6. Silicon has a roughly hundred times weaker magneto-optical activity compared to commonly used materials but it counters this deficiency by having orders of magnitudes lower losses which allows for long propagation lengths. To achieve a sufficiently strong effect, we switched from the magneto-optical phase shift, which is only generated at the edges of the waveguide, to Faraday rotation, which is produced over the whole active waveguide cross-section. Commonly used waveguide cross-sections of around $500\,\mathrm{nm} \times 220\,\mathrm{nm}$ feature strong form birefringence and carry a large part of their energy outside the silicon core, both of which spoil the efficiency of the Faraday rotation. We therefore utilized a large $3\,\mu\mathrm{m} \times 3\,\mu\mathrm{m}$ cross-section with carefully engineered bends and coupling section [148, 149]. For a 0.5 T biasing field 6 cm propagation length are required.

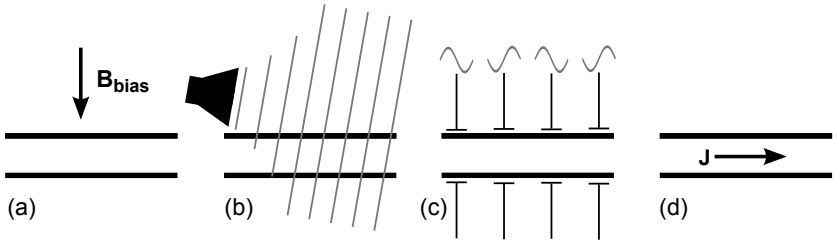

Figure 62: Possible ways to achieve a nonreciprocal phase shift. (a) Magneto-optical effects. (b) A travelling refractive index perturbation produced by sound waves. (c) A travelling refractive index perturbation produced by electro-optical modulation. (d) An electrical current aligned with the wave propagation vector.

To bring this into a decent form factor, we proposed a spiral with engineered birefringence in the bends such that the Faraday rotation can accumulate continuously in the straight sections of the spiral which are parallel to the magnetic field. Such a device will achieve similar footprints as already proposed nonreciprocal concepts without the need for a separate magneto-optical material.

7.2 OUTLOOK

We have seen that all three ring resonator-based concepts yield a convincing performance if combined with bonded garnets which is a difficult process to include in the production. The obvious step here is to improve the direct deposition of garnets onto silicon or to search for better suited materials. One of the latest examples for the former approach is Ref. [142] where Ce:YIG was deposited directly onto silicon without the need of a YIG seedlayer [25], thus bringing the magneto-optical material closer to the waveguide core and improving the efficiency. Nonetheless, as we can see from table 4 the magneto-optical activity is still not sufficient. Recent examples for new materials are Refs. [159] and [160] which deposited bismuth-doped terbium iron garnet and iron-substituted strontium titanate onto silicon, respectively. Both do not exceed the performance of Ce:YIG, so far. Another recent research direction, is to use garnet substrates and deposit waveguide materials other than silicon on top. For example, in Ref. [161] a ring resonator with chalcogenide core is placed on top of a Ce:YIG garnet achieving an insertion loss of 3 dB and 40 dB isolation ratio.

Another option to realize the proposed devices is to produce the frequency splitting in the ring resonator by other means than magneto-optical effects. Fig. 62 summarizes ways to produce a nonreciprocal phase shift. It can be produced by a travelling modulation of the permittivity [162],

$$\varepsilon(x,y,z,t) = \varepsilon_{static}(x,y) + \Delta\varepsilon(x,y)\cos(\omega_m t - k_m z). \tag{163}$$

Mostly, such a perturbation is used to nonreciprocally couple a pair of modes [39, 41, 163–166], but it can also be used as a nonreciprocal phase shifter [167]. Alù and co-workers realized a circulator operating in the microwave regime based on a ring resonator with a travelling modulation [168] and proposed a scheme for optical wavelengths based on three coupled resonators all modulated with the same frequency but each modulation is off-set by a phase difference of 120° with respect to the adjacent resonator [169, 170]. Index perturbations as in eq. 163 have been realized in various ways. They can be produced from acoustic waves that can be either created by stimulated Brillouin scattering [34] or by a piezoelectric transducer [41]. Alternatively, one can produce the perturbation through electro-optical modulation or modulating the charge carrier density in a PN-junction [40]. Or they can be produced by an strong optical pump pulse which creates free charge carriers inside the silicon which thereby creates a travelling refractive index front [171]. The last effect differs from the previous effects in that instead of a refractive index modulation a travelling front is introduced. This can serve as a nonreciprocal device for transient signals but cannot block CW signals which would require a continuous modulation. All these schemes are particularly interesting for a switch as in chapter 3 as they are all caused by an electrical or optical signal which is potentially faster switched on or off than a magnetic biasing field.

The last way to produce a nonreciprocal phase shift was recently proposed by Bliokh and co-workers [172]. They predict that a current along a plasmon waveguide will cause a Doppler shift of the wave frequency in the drifting electron plasma which will make the metal's permittivity nonreciprocal. For a gold nanowire with a diameter of 40 nm a measurable nonreciprocal phase shift is expected for currents in the mA-range.

Finally, we want to discuss the future steps for the silicon Faraday rotator in chapter 6. The concept is submitted as an international patent. The obvious route is to build a proof of principle. A first prototype was already realized in cooperation with VTT in Finland [173]. This prototype combined with external polarizers already showed a very promising isolation ratio of 4, 5 dB (see Fig. 63). However, due to a not fully optimized fabrication process, the side of the waveguide core was not fully etched away and the remanent silicon caused reciprocal coupling between the TE- and the TM-mode in the bends. This coupling combined with the Faraday rotation caused quite a chaotic isolation spectrum as seen in Fig. 63b that is difficult to engineer and to tune to a desired wavelength. Work is therefore done to produce well behaved structures with fully etched waveguides.

Besides for our system with silicon waveguides the idea to enable spiralling Faraday waveguides by ensuring 180° birefringence in the bends is also interesting for shape-anisotropic Faraday rotators with

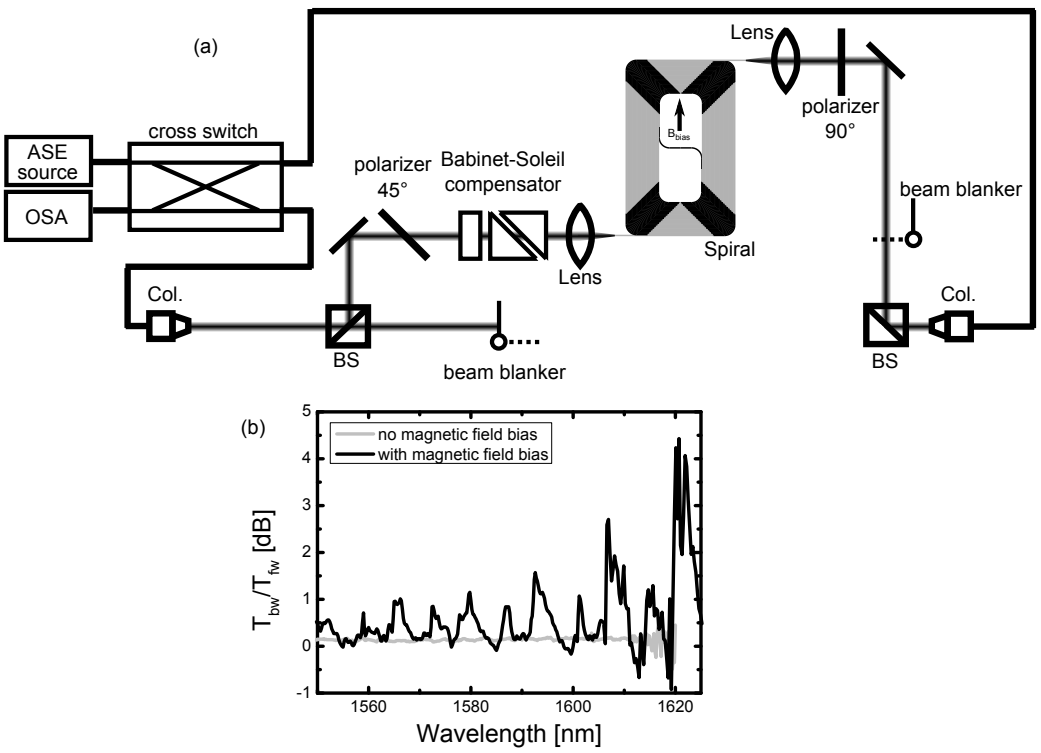

Figure 63: (a) Experimental isolator with external polarisers. A Babinet-Soleil compensator is used to mitigate the birefringence after the spiral where the light is polarized at 45°. To make sure that a potential asymmetry in the cross switch does not influence the measured isolation ratio, we measure the transmission through an reference arm. The device's isolation ratio is obtained by: $I = \frac{T_{bw}}{T_{fw}} \frac{T_{fw,ref}}{T_{bw,ref}}$. (b) Resulting Isolation. It can be clearly seen that without magnetic bias the device is reciprocal. The biasing field is 0.3 Twhich yields a rotation of 27° in the 6 cm long active section and an expected isolation of 4.88 dB which fits well with what we measure.

quasi phase matching [159]. The propagation lengths needed here are as well in the cm-range and profit therefore as well from compacted dimensions.

BIBLIOGRAPHY

[1] P. N. Howard, A. Duffy, D. Freelon, M. Hussain, W. Mari, and M. Mazaid, "Opening Closed Regimes: What Was the Role of Social Media During the Arab Spring?," Available at SSRN: https://ssrn.com/abstract=2595096, 2011. (Cited on page 3.)

[2] S. Hong and D. Nadler, "Which candidates do the public discuss online in an election campaign?: The use of social media by 2012 presidential candidates and its impact on candidate salience," *Government Information Quarterly* **29**, pp. 455–461, oct 2012.

[3] H. Allcott and M. Gentzkow, "Social Media and Fake News in the 2016 Election," *Journal of Economic Perspectives* **31**(2), pp. 211–236, 2017. (Cited on page 3.)

[4] Cisco, "Cisco Visual Networking Index: Forecast and Methodology, 2015-2021," White Paper C11-738085-00, 2016. (Cited on pages 3 and 4.)

[5] Cisco, "Cisco Visual Networking Index: Forecast and Methodology, 2016-2022," White Paper C11-481360-01, 2017. (Cited on page 4.)

[6] Cisco, "The Zettabyte Era: Trends and Analysis," White Paper C11-739110-00, 2017. (Cited on pages 3 and 4.)

[7] D. Thomson, A. Zilkie, J. E. Bowers, T. Komljenovic, G. T. Reed, L. Vivien, D. Marris-Morini, E. Cassan, L. Virot, J.-M. Fédéli, J.-M. Hartmann, J. H. Schmid, D.-X. Xu, F. Boeuf, P. O'Brien, G. Z. Mashanovich, and M. Nedeljkovic, "Roadmap on silicon photonics," *Journal of Optics* **18**, p. 073003, jul 2016. (Cited on page 3.)

[8] Yole Développement, "Silicon Photonics for Data Centers and Other Applications 2016," Report, 2016. (Cited on pages 3 and 4.)

[9] E. Agrell, M. Karlsson, A. R. Chraplyvy, D. J. Richardson, P. M. Krummrich, P. Winzer, K. Roberts, J. K. Fischer, S. J. Savory, B. J. Eggleton, M. Secondini, F. R. Kschischang, A. Lord, J. Prat, I. Tomkos, J. E. Bowers, S. Srinivasan, M. Brandt-Pearce, and N. Gisin, "Roadmap of optical communications," *Journal of Optics* **18**, p. 063002, jun 2016. (Cited on page 3.)

[10] R. Tkach and A. Chraplyvy, "Regimes of feedback effects in 1.5-um distributed feedback lasers," *Journal of Lightwave Technology* **4**(11), pp. 1655–1661, 1986. (Cited on page 3.)

[11] N. Schunk and K. Petermann, "Numerical analysis of the feedback regimes for a single-mode semiconductor laser with external feedback," *IEEE Journal of Quantum Electronics* **24**(7), pp. 1242–1247, 1988.

[12] M. L. Masanovic, V. Lal, J. A. Summers, J. S. Barton, E. J. Skogen, L. G. Rau, L. A. Coldren, and D. J. Blumenthal, "Widely Tunable Monolithically Integrated All-Optical Wavelength Converters in InP," *Journal of Lightwave Technology* **23**(3), p. 1350, 2005. (Cited on page 3.)

[13] D. Jalas, "Optical Isolation using nonreciprocal Ring Resonators," Master's thesis, Technische Universität Hamburg-Harburg, 2010. (Cited on pages 5, 38, 42, and 68.)

[14] A. Maznev, A. Every, and O. Wright, "Reciprocity in reflection and transmission: What is a 'phonon diode'?," *Wave Motion* **50**, pp. 776–784, jun 2013. (Cited on pages 10 and 16.)

[15] C. Vassallo, *Optical waveguide concepts*, Elsevier Science Limited, Amsterdam, 1991. (Cited on pages 11, 15, and 16.)

[16] H. A. Haus, *Waves and fields in optoelectronics*, vol. 464, Prentice-Hall Englewood Cliffs, NJ, 1984. (Cited on pages 15, 43, 45, 49, 50, and 59.)

[17] Y. Shoji, M. Ito, Y. Shirato, and T. Mizumoto, "MZI optical isolator with Si-wire waveguides by surface-activated direct bonding.," *Optics express* **20**, pp. 18440–8, jul 2012. (Cited on page 18.)

[18] B. E. A. Saleh and M. C. Teich, *Fundamentals of Photonics*, Wiley, New York, 1991. (Cited on pages 18, 25, 68, and 119.)

[19] H. Dötsch, N. Bahlmann, O. Zhuromskyy, M. Hammer, L. Wilkens, R. Gerhardt, P. Hertel, and A. F. Popkov, "Applications of magneto-optical waveguides in integrated optics: review," *Journal of the Optical Society of America B* **22**(1), p. 240, 2005. (Cited on pages 18, 32, 38, 119, 120, and 123.)

[20] Y. Shoji, K. Miura, and T. Mizumoto, "Optical nonreciprocal devices based on magneto-optical phase shift in silicon photonics," *Journal of Optics* **18**(1), p. 013001, 2016.

[21] Y. Shoji and T. Mizumoto, "Waveguide magneto-optical devices for photonics integrated circuits [Invited]," *Optical Materials Express* **8**(8), pp. 2387–2394, 2018.

[22] P. Pintus, D. Huang, P. Morton, Y. Shoji, T. Mizumoto, and J. E. Bowers, "Integrated Optical Isolator and Circulator in Silicon Photonics," in *2018 European Conference on Optical Communication (ECOC)*, pp. 1–3, 2018. (Cited on page 18.)

[23] W. Van Parys, B. Moeyersoon, D. Van Thourhout, R. Baets, M. Vanwolleghem, B. Dagens, J. Decobert, O. Le Gouezigou, D. Make, R. Vanheertum, and L. Lagae, "Transverse magnetic mode nonreciprocal propagation in an amplifying AlGaInAs/InP optical waveguide isolator," *Applied Physics Letters* **88**(7), p. 071115, 2006. (Cited on page 18.)

[24] Z. Wang and S. Fan, "Optical circulators in two-dimensional magneto-optical photonic crystals," *Optics Letters* **30**(15), p. 1989, 2005. (Cited on pages 18, 76, and 77.)

[25] L. Bi, J. Hu, P. Jiang, D. H. Kim, G. F. Dionne, L. C. Kimerling, and C. A. Ross, "On-chip optical isolation in monolithically integrated non-reciprocal optical resonators," *Nat Photon* **5**, pp. 758–762, dec 2011. (Cited on pages 28, 40, 77, 112, 113, 115, 124, and 132.)

[26] M.-C. Tien, T. Mizumoto, P. Pintus, H. Kromer, and J. E. Bowers, "Silicon ring isolators with bonded nonreciprocal magneto-optic garnets.," *Optics express* **19**, pp. 11740–5, jun 2011. (Cited on pages 40, 77, and 92.)

[27] D. Huang, P. Pintus, C. Zhang, P. Morton, Y. Shoji, T. Mizumoto, and J. E. Bowers, "Dynamically reconfigurable integrated optical circulators," *Optica* **4**(1), pp. 23–30, 2017. (Cited on pages 18, 112, 113, 115, and 131.)

[28] F. D. M. Haldane and S. Raghu, "Possible Realization of Directional Optical Waveguides in Photonic Crystals with Broken Time-Reversal Symmetry," *Physical Review Letters* **100**, p. 13904, jan 2008. (Cited on page 18.)

[29] S. Raghu and F. D. M. Haldane, "Analogs of quantum-Hall-effect edge states in photonic crystals," *Physical Review A* **78**, p. 33834, sep 2008.

[30] Z. Wang, Y. D. Chong, J. D. Joannopoulos, and M. Soljačić, "Reflection-Free One-Way Edge Modes in a Gyromagnetic Photonic Crystal," *Physical Review Letters* **100**, p. 13905, jan 2008.

[31] Z. Wang, Y. Chong, J. D. Joannopoulos, and M. Soljacic, "Observation of unidirectional backscattering-immune topological electromagnetic states," *Nature* **461**, pp. 772–775, oct 2009.

[32] L. Lu, J. D. Joannopoulos, and M. Soljacic, "Topological photonics," *Nat Photon* **8**, pp. 821–829, nov 2014. (Cited on page 18.)

[33] M. Krause, H. Renner, and E. Brinkmeyer, "Optical isolation in silicon waveguides based on nonreciprocal Raman amplification," *Electronics Letters* **44**(11), pp. 691–693, 2008. (Cited on page 18.)

[34] C. G. Poulton, R. Pant, A. Byrnes, S. Fan, M. J. Steel, and B. J. Eggleton, "Design for broadband on-chip isolator using Stimulated Brillouin Scattering in dispersion-engineered chalcogenide waveguides.," *Optics express* **20**, pp. 21235–46, sep 2012. (Cited on pages 18 and 133.)

[35] M. D. Tocci, M. J. Bloemer, M. Scalora, J. P. Dowling, and C. M. Bowden, "Thin-film nonlinear optical diode," *Applied Physics Letters* **66**(18), p. 2324, 1995. (Cited on page 18.)

[36] K. Gallo, G. Assanto, K. R. Parameswaran, and M. M. Fejer, "All-optical diode in a periodically poled lithium niobate waveguide," *Applied Physics Letters* **79**(3), p. 314, 2001. (Cited on page 18.)

[37] Y. Shi, Z. Yu, and S. Fan, "Limitations of nonlinear optical isolators due to dynamic reciprocity," *Nature Photonics* **9**, p. 388, may 2015. (Cited on page 18.)

[38] H. Lira, Z. Yu, S. Fan, and M. Lipson, "Electrically Driven Nonreciprocity Induced by Interband Photonic Transition on a Silicon Chip," *Phys. Rev. Lett.* **109**, p. 33901, jul 2012. (Cited on page 18.)

[39] Z. Yu and S. Fan, "Complete optical isolation created by indirect interband photonic transitions," *Nat Photon* **3**, pp. 91–94, feb 2009. (Cited on pages 18 and 133.)

[40] H. Lira, Z. Yu, S. Fan, and M. Lipson, "Electrically Driven Nonreciprocity Induced by Interband Photonic Transition on a Silicon Chip," *Physical Review Letters* **109**, p. 033901, jul 2012. (Cited on pages 18 and 133.)

[41] D. B. Sohn, S. Kim, and G. Bahl, "Time-reversal symmetry breaking with acoustic pumping of nanophotonic circuits," *Nature Photonics* **12**(2), pp. 91–97, 2018. (Cited on pages 18 and 133.)

[42] C. Wang, X.-L. Zhong, and Z.-Y. Li, "Linear and passive silicon optical isolator," *Sci. Rep.* **2**, sep 2012. (Cited on page 19.)

[43] C. Wang, C.-Z. Zhou, and Z.-Y. Li, "On-chip optical diode based on silicon photonic crystal heterojunctions.," *Optics express* **19**, pp. 26948–55, dec 2011.

[44] X. Fang, "Polarization-independent all-fiber isolator based on asymmetric fiber tapers," *Optics Letters* **21**, p. 1792, nov 1996.

[45] L. Feng, M. Ayache, J. Huang, Y.-L. Xu, M.-H. Lu, Y.-F. Chen, Y. Fainman, and A. Scherer, "Nonreciprocal Light Propagation in a Silicon Photonic Circuit," *Science* **333**, pp. 729–733, aug 2011. (Cited on page 19.)

[46] S. Fan, R. Baets, A. Petrov, Z. Yu, J. D. Joannopoulos, W. Freude, A. Melloni, M. Popovic, M. Vanwolleghem, D. Jalas, M. Eich, M. Krause, H. Renner, E. Brinkmeyer, and C. R. Doerr, "Comment on "Nonreciprocal Light Propagation in a Silicon Photonic Circuit"," *Science* **335**(6064), pp. 38–38, 2012. (Cited on page 19.)

[47] A. Petrov, D. Jalas, M. Eich, W. Freude, S. Fan, Z. Yu, R. Baets, M. Popović, A. Melloni, and J. D. Joannopoulos, "Comment on "Linear and passive silicon optical isolator" in Scientific Reports 2, 674," *arXiv preprint arXiv:1301.7243* , 2013. (Cited on page 19.)

[48] H. Kurt, D. Yilmaz, A. E. Akosman, and E. Ozbay, "Asymmetric light propagation in chirped photonic crystal waveguides.," *Optics express* **20**, pp. 20635–46, aug 2012. (Cited on page 19.)

[49] M. Lockyear, A. Hibbins, K. White, and J. Sambles, "One-way diffraction grating," *Phys. Rev. E* **74**, p. 56611, nov 2006.

[50] A. Serebryannikov, "One-way diffraction effects in photonic crystal gratings made of isotropic materials," *Phys. Rev. B* **80**(15), p. 155117, 2009.

[51] W.-M. Ye, X.-D. Yuan, C.-C. Guo, and C. Zen, "Unidirectional transmission in non-symmetric gratings made of isotropic material.," *Optics express* **18**, pp. 7590–5, apr 2010. (Cited on page 19.)

[52] P. R. Berman, "Optical Faraday rotation," *American Journal of Physics* **78**(3), pp. 270–276, 2010. (Cited on page 20.)

[53] P. W. Milonni and J. H. Eberly, "Laser Physics," ch. 3, John Wiley & Sons, 2010. (Cited on page 20.)

[54] M. Born and E. Wolf, *Principles of Optics, seventh expanded edition*, Cambridge University Press, Cambridge, England, 1999. (Cited on pages 20 and 21.)

[55] M. Fox, *Optical properties of solids*, Oxford University Press, Inc., 2010. (Cited on page 20.)

[56] A. K. Zvezdin and V. A. Kotov, *Modern Magnetooptics and Magnetooptical Materials: Studies in Condensed Matter*, vol. 1, Taylor & Francis Group, Boca Raton, FL USA, 1997. (Cited on pages 23 and 27.)

[57] E. U. Condon, "Theories of Optical Rotatory Power," *Reviews of Modern Physics* **9**, pp. 432–457, oct 1937. (Cited on page 25.)

[58] A. Lakhtakia, V. V. Varadan, and V. K. Varadan, "Field equations, Huygens's principle, integral equations, and theorems for radiation and scattering of electromagnetic waves in isotropic chiral media," *Journal of the Optical Society of America A* **5**(2), pp. 175–184, 1988. (Cited on page 25.)

[59] M. Born, *Optik*, Springer-Verlag Berlin Heidelberg, 1972. (Cited on page 25.)

[60] L. D. Landau and E. M. Lifshitz, *Course of Theoretical Physics. Vol. 8: Electrodynamics of Continuous Media*, Pergamon Press, London, GB, 1960. (Cited on page 25.)

[61] H. Iwamura, S. Hayashi, and H. Iwasaki, "A compact optical isolator using a Y3Fe5O12 crystal for near infra-red radiation," *Optical and Quantum Electronics* **10**(5), pp. 393–398, 1978. (Cited on page 27.)

[62] R. C. Booth and E. A. D. White, "Magneto-optic properties of rare earth iron garnet crystals in the wavelength range 1.1-1.7μm and their use in device fabrication," *Journal of Physics D: Applied Physics* **17**(3), p. 579, 1984. (Cited on page 27.)

[63] W. A. Crossley, R. W. Cooper, J. L. Page, and R. P. van Stapele, "Faraday Rotation in Rare Earth Iron Garnets," *Journal of Applied Physics* **40**(3), 1969.

[64] W. Wettling, B. Andlauer, P. Koidl, J. Schneider, and W. Tolksdorf, "Optical absorption and Faraday rotation in yttrium iron garnet," *physica status solidi (b)* **59**, pp. 63–70, sep 1973. (Cited on page 27.)

[65] T. Nakano, H. Yuri, and U. Kihara, "Magneto-optical properties of YIG single crystal by TSFZ method," 1984. (Cited on page 27.)

[66] G. F. Dionne, *Magnetic oxides*, vol. 14, Springer-Verlag US, 2009. (Cited on page 27.)

[67] S. Higuchi, Y. Furukawa, S. Takekawa, O. Kamada, and K. Kitamura, "Magneto-Optical Properties of Cerium-Substituted Yttrium Iron Garnet Single Crystals Grown by Traveling Solvent Floating Zone Method," *Japanese Journal of Applied Physics* **38**(7R), p. 4122, 1999. (Cited on page 27.)

[68] T. Shintaku, A. Tate, and S. Mino, "Ce-substituted yttrium iron garnet films prepared on Gd[sub 3]Sc[sub 2]Ga[sub 3]O[sub 12] garnet substrates by sputter epitaxy," *Applied Physics Letters* **71**(12), p. 1640, 1997. (Cited on pages 27 and 118.)

[69] T. Shintaku, "Integrated optical isolator based on nonreciprocal higher-order mode conversion," *Applied Physics Letters* **66**(21), p. 2789, 1995. (Cited on page 27.)

[70] M. Gomi, H. Furuyama, and M. Abe, "Strong magneto-optical enhancement in highly Ce-substituted iron garnet films prepared by sputtering," *Journal of Applied Physics* **70**(11), p. 7065, 1991. (Cited on page 27.)

[71] X. Liang, J. Xie, L. Deng, and L. Bi, "First principles calculation on the magnetic, optical properties and oxygen vacancy effect of CexY3-xFe5O12," *Applied Physics Letters* **106**, p. 052401, feb 2015. (Cited on page 27.)

[72] T. Wehlus, T. Körner, S. Leitenmeier, A. Heinrich, and B. Stritzker, "Magneto-optical garnets for integrated optoelectronic devices," *physica status solidi (a)* **208**, pp. 252–263, feb 2011. (Cited on page 28.)

[73] L. Bi, J. Hu, P. Jiang, H. Kim, D. Kim, M. Onbasli, G. Dionne, and C. Ross, "Magneto-Optical Thin Films for On-Chip Monolithic Integration of Non-Reciprocal Photonic Devices," *Materials* **6**, pp. 5094–5117, nov 2013. (Cited on pages 28 and 118.)

[74] T. Mizumoto, Y. Shoji, and R. Takei, "Direct Wafer Bonding and Its Application to Waveguide Optical Isolators," *Materials* **5**, pp. 985–1004, may 2012. (Cited on page 28.)

[75] T. Goto, Y. Eto, K. Kobayashi, Y. Haga, M. Inoue, and C. A. Ross, "Vacuum annealed cerium-substituted yttrium iron garnet films on non-garnet substrates for integrated optical circuits," *Journal of Applied Physics* **113**(17), p. 17A939, 2013. (Cited on page 28.)

[76] T. Goto, M. C. Onbasli, and C. A. Ross, "Magneto-optical properties of cerium substituted yttrium iron garnet films with reduced thermal budget for monolithic photonic integrated circuits," *Optics Express* **20**(27), pp. 28507–28517, 2012. (Cited on page 28.)

[77] T. Goto, M. C. Onbasli, D. H. Kim, V. Singh, M. Inoue, L. C. Kimerling, and C. A. Ross, "A nonreciprocal racetrack resonator based on vacuum-annealed magnetooptical cerium-substituted yttrium iron garnet," *Optics Express* **22**(16), pp. 19047–19054, 2014. (Cited on page 28.)

[78] G. Koeckelberghs, M. Vangheluwe, K. V. Doorsselaere, E. Robijns, A. Persoons, and T. Verbiest, "Regioregularity in Poly(3-alkoxythiophene)s: Effects on the Faraday Rotation and Polymerization Mechanism," *Macromolecular Rapid Communications* **27**(22), pp. 1920–1925, 2006. (Cited on pages 28, 29, and 70.)

[79] P. Gangopadhyay, S. Foerier, G. Koeckelberghs, M. Vangheluwe, A. Persoons, and T. Verbiest, "Efficient Faraday rotation in conjugated polymers," 2006. (Cited on pages 29, 70, and 103.)

[80] P. Gangopadhyay, R. Voorakaranam, A. Lopez-Santiago, S. Foerier, J. Thomas, R. A. Norwood, A. Persoons, and N. Peyghambarian, "Faraday Rotation Measurements on Thin Films of Regioregular Alkyl-Substituted Polythiophene Derivatives," *The Journal of Physical Chemistry C* **112**, pp. 8032–8037, may 2008. (Cited on pages 29 and 103.)

[81] F. Araoka, M. Abe, Y. Takakazu, and T. Hideo, "Large Faraday Rotation in a \pi-Conjugated Poly(arylene ethynylene) Thin Film," *Applied Physics Express* **2**(1), p. 11501, 2009. (Cited on pages 28, 29, and 70.)

[82] K. Messaad, J. Charrier, A. Mosqueron, D. Bosc, and P. Rochard, "Study of optical losses in poly(3-octylthiophene) planar and inverted RIB waveguides," *Journal of Applied Polymer Science* **121**, pp. 2134–2142, aug 2011. (Cited on page 28.)

[83] S. V. Kamat, S. H. Tamboli, V. Puri, R. K. Puri, R. B. Patil, and M.-F. Luo, "Determination of optical transmission loss in poly (3-methyl thiophene) thin film planar waveguide: effect of vapour chopping," *Progress In Electromagnetics Research M* **18**, pp. 197–207, 2011. (Cited on page 28.)

[84] P. Gangopadhyay, G. Koeckelberghs, A. Lopez-Santiago, R. A. Norwood, N. Peyghambarian, and A. Persoons, "Magnetic and magneto optic properties of substituted polythiophenes," in *Proc. SPIE*, **7413**, pp. 74130F–74130F–9, 2009. (Cited on pages 29, 30, and 103.)

[85] L. D'Amico, F. D'Orazio, J. Dormann, D. Fiorani, F. Lucari, and E. Tronc, "Magneto-Optical Effects on γ-Fe₂O₃ Nanometric Particles in Polyvinylic Alcohol," *Materials Science Forum* **195**, pp. 173–178, 1995. (Cited on page 31.)

[86] F. Bentivegna, M. Nyvlt, J. Ferré, J. P. Jamet, A. Brun, S. Visnovsky, and R. Urban, "Magnetically textured γ-Fe2O3 nanoparticles in a silica gel matrix: Optical and magneto-optical properties," *Journal of Applied Physics* **85**, pp. 2270–2278, feb 1999. (Cited on page 31.)

[87] M. Domínguez, D. Ortega, J. S. Garitaonandía, R. Litrán, C. Barrera-Solano, E. Blanco, and M. Ramírez-del Solar, "Magneto-optic Faraday effect in maghemite nanoparticles/silica matrix nanocomposites prepared by the Sol-Gel method,"

Journal of Magnetism and Magnetic Materials **320**(20), pp. e725–e729, 2008. (Cited on page 31.)

[88] H. Guerrero, G. Rosa, M. P. Morales, F. del Monte, E. M. Moreno, D. Levy, R. Pérez del Real, T. Belenguer, and C. J. Serna, "Faraday rotation in magnetic γ-Fe2O3/SiO2 nanocomposites," *Applied Physics Letters* **71**, pp. 2698–2700, nov 1997. (Cited on page 31.)

[89] G. Rosa, H. Guerrero, D. Levy, A. Álvarez-Herrero, and R. P. del Real, "Surface effects in magnetic nanoparticles measured by means of a magneto-optical method," *Journal of Applied Physics* **97**, p. 64314, mar 2005. (Cited on pages 30, 31, and 32.)

[90] F. Royer, D. Jamon, J. J. Rousseau, V. Cabuil, D. Zins, H. Roux, and C. Bovier, "Experimental investigation on γ-Fe2O3 nanoparticles Faraday Rotation: particles size dependence," *The European Physical Journal Applied Physics* **22**, pp. 83–87, may 2003. (Cited on pages 30 and 31.)

[91] M. Zayat, F. del Monte, M. P. Morales, G. Rosa, H. Guerrero, C. J. Serna, and D. Levy, "Highly Transparent γ-Fe2O3/Vycor-Glass Magnetic Nanocomposites Exhibiting Faraday Rotation," *Advanced Materials* **15**, pp. 1809–1812, nov 2003. (Cited on page 31.)

[92] Y. A. Barnakov, B. Scott, V. Golub, L. Kelly, V. Reddy, and K. Stokes, "Spectral dependence of Faraday rotation in magnetite-polymer nanocomposites," *Journal of Physics and Chemistry of Solids* **65**(5), pp. 1005–1010, 2004. (Cited on pages 30 and 31.)

[93] A. Lopez-Santiago, P. Gangopadhyay, J. Thomas, R. A. Norwood, A. Persoons, and N. Peyghambarian, "Faraday rotation in magnetite-polymethylmethacrylate core-shell nanocomposites with high optical quality," *Applied Physics Letters* **95**, p. 143302, oct 2009. (Cited on page 31.)

[94] H. Amata, F. Royer, F. Choueikani, D. Jamon, F. Parsy, J.-E. Broquin, S. Neveu, and J. Jacques Rousseau, "Hybrid magneto-optical mode converter made with a magnetic nanoparticles-doped SiO2/ZrO2 layer coated on an ion-exchanged glass waveguide," *Applied Physics Letters* **99**, p. 251108, dec 2011. (Cited on page 31.)

[95] F. Choueikani, F. Royer, D. Jamon, A. Siblini, J. J. Rousseau, S. Neveu, and J. Charara, "Magneto-optical waveguides made of cobalt ferrite nanoparticles embedded in silica/zirconia organic-inorganic matrix," *Applied Physics Letters* **94**(5), p. 051113, 2009. (Cited on pages 31 and 118.)

[96] A. Lopez-Santiago, H. R. Grant, P. Gangopadhyay, R. Voorakaranam, R. A. Norwood, and N. Peyghambarian, "Cobalt ferrite nanoparticles polymer composites based all-optical magnetometer," *Optical Materials Express* **2**(7), pp. 978–986, 2012. (Cited on pages 31, 107, and 109.)

[97] X. Zhang, J. Schoenes, and P. Wachter, "Kerr-effect and dielectric tensor elements of magnetite (Fe_3O_4) between 0.5 and 4.3 eV," *Solid State Communications* **39**(1), pp. 189–192, 1981. (Cited on page 29.)

[98] T. Tepper, F. Ilievski, C. A. Ross, T. R. Zaman, R. J. Ram, S. Y. Sung, and B. J. H. Stadler, "Magneto-optical properties of iron oxide films," *Journal of Applied Physics* **93**(10), p. 6948, 2003. (Cited on pages 29 and 118.)

[99] A. Schlegel, S. F. Alvarado, and P. Wachter, "Optical properties of magnetite (Fe 3 O 4)," *Journal of Physics C: Solid State Physics* **12**, pp. 1157–1164, mar 1979. (Cited on page 29.)

[100] T. Tepper, C. A. Ross, and G. F. Dionne, "Microstructure and optical properties of pulsed-laser-deposited iron oxide films," *Magnetics, IEEE Transactions on* **40**(3), pp. 1685–1690, 2004. (Cited on pages 29 and 118.)

[101] D. Jamon, F. Donatini, J. Monin, M. Rasa, V. Socoliuc, O. Filip, D. Bica, and V. Sofonea, "Concentration dependence of magnetisation and magneto-optical effects in a ferrofluid with double layer stabilized particles," *Journal of Magnetism and Magnetic Materials* **201**(1-3), pp. 174–177, 1999. (Cited on page 30.)

[102] R. Kekesi, F. Royer, D. Jamon, M. F. Blanc Mignon, E. Abou-Diwan, J. P. Chatelon, S. Neveu, and E. Tombacz, "3D magneto-photonic crystal made with cobalt ferrite nanoparticles silica composite structured as inverse opal," *Optical Materials Express* **3**(7), pp. 935–947, 2013. (Cited on page 30.)

[103] A. Yariv and P. Yeh, *Photonics: Optical Electronics in Modern Communications (The Oxford Series in Electrical and Computer Engineering)*, Oxford University Press, Inc., New York, NY, USA, 6th ed., 2006. (Cited on pages 32, 50, and 124.)

[104] A. W. Snyder and J. Love, *Optical waveguide theory*, Springer US, 1983. (Cited on page 35.)

[105] Z. Wang and S. Fan, "Magneto-optical defects in two-dimensional photonic crystals," *Applied Physics B* **81**(2-3), pp. 369–375, 2005. (Cited on pages 38, 76, 77, 83, and 93.)

[106] D. Jalas, A. Petrov, M. Krause, J. Hampe, and M. Eich, "Resonance splitting in gyrotropic ring resonators.," *Optics letters* **35**(20), pp. 3438–3440, 2010. (Cited on pages 40, 41, 50, and 53.)

[107] P. Pintus, F. Di Pasquale, and J. E. Bowers, "Integrated TE and TM optical circulators on ultra-low-loss silicon nitride platform.," *Optics express* **21**, pp. 5041–52, feb 2013. (Cited on pages 40, 76, and 92.)

[108] E. A. J. Marcatili, "Bends in Optical Dielectric Guides," *Bell System Technical Journal* **48**, pp. 2103–2132, sep 1969. (Cited on page 41.)

[109] M. Krause, "Finite-Difference Mode Solver for Curved Waveguides With Angled and Curved Dielectric Interfaces," *J. Lightwave Technol.* **29**(5), pp. 691–699, 2011. (Cited on page 42.)

[110] D. Huang, P. Pintus, Y. Shoji, P. Morton, T. Mizumoto, and J. E. Bowers, "Integrated broadband Ce:YIG/Si Mach-Zehnder optical isolators with over 100nm tuning range," *Optics Letters* **42**(23), pp. 4901–4904, 2017. (Cited on page 43.)

[111] S. Fan, W. Suh, and J. D. Joannopoulos, "Temporal coupled-mode theory for the Fano resonance in optical resonators," *Journal of the Optical Society of America A* **20**(3), pp. 569–572, 2003. (Cited on pages 43 and 46.)

[112] W. Suh, Z. Wang, and S. Fan, "Temporal coupled-mode theory and the presence of non-orthogonal modes in lossless multimode cavities," 2004. (Cited on pages 44 and 46.)

[113] J. D. Joannopoulos, S. G. Johnson, J. N. Winn, and R. D. Meade, *Photonic crystals: molding the flow of light*, Princeton university press, 2011. (Cited on pages 43, 45, 49, and 50.)

[114] P. T. Kristensen, J. R. de Lasson, M. Heuck, N. Gregersen, and J. Mørk, "On the Theory of Coupled Modes in Optical Cavity-Waveguide Structures," *Journal of Lightwave Technology* **35**(19), pp. 4247–4259, 2017. (Cited on page 44.)

[115] A. Yariv, "Universal relations for coupling of optical power between microresonators and dielectric waveguides," *Electronics Letters* **36**(4), pp. 321–322, 2000. (Cited on page 53.)

[116] B. E. Little, J.-P. Laine, and S. T. Chu, "Surface-roughness-induced contradirectional coupling in ring and disk resonators," *Optics Letters* **22**(1), pp. 4–6, 1997. (Cited on page 58.)

[117] Z. Zhang, M. Dainese, L. Wosinski, and M. Qiu, "Resonance-splitting and enhanced notch depth in SOI ring resonators with

mutual mode coupling," *Optics Express* **16**, p. 4621, mar 2008. (Cited on pages 59 and 61.)

[118] F. Morichetti, A. Canciamilla, and A. Melloni, "Statistics of backscattering in optical waveguides," *Optics Letters* **35**(11), pp. 1777–1779, 2010. (Cited on page 63.)

[119] A. Li, T. Van Vaerenbergh, P. De Heyn, P. Bienstman, and W. Bogaerts, "Backscattering in silicon microring resonators: a quantitative analysis," *Laser & Photonics Reviews* **10**, pp. 420–431, may 2016. (Cited on pages 63 and 64.)

[120] S. Ghosh, S. Keyvaninia, W. Van Roy, T. Mizumoto, G. Roelkens, and R. Baets, "Adhesively bonded Ce:YIG/SOI integrated optical circulator.," *Optics letters* **38**, pp. 965–7, mar 2013. (Cited on page 76.)

[121] K. Mitsuya, Y. Shoji, and T. Mizumoto, "Demonstration of a Silicon Waveguide Optical Circulator," *Photonics Technology Letters, IEEE* **25**, pp. 721–723, apr 2013. (Cited on page 76.)

[122] N. Kono, K. Kakihara, K. Saitoh, and M. Koshiba, "Nonreciprocal microresonators for the miniaturization of optical waveguide isolators," *Optics Express* **15**, p. 7737, jun 2007. (Cited on page 76.)

[123] W. Śmigaj, J. Romero-Vivas, B. Gralak, L. Magdenko, B. Dagens, and M. Vanwolleghem, "Magneto-optical circulator designed for operation in a uniform external magnetic field.," *Optics letters* **35**, pp. 568–70, feb 2010. (Cited on pages 76 and 77.)

[124] W. Śmigaj, L. Magdenko, J. Romero-Vivas, S. Guenneau, B. Dagens, B. Gralak, and M. Vanwolleghem, "Compact optical circulator based on a uniformly magnetized ring cavity," *Photonics and Nanostructures - Fundamentals and Applications* **10**, pp. 83–101, jan 2012. (Cited on pages 76, 77, 83, and 93.)

[125] P. Pintus, D. Huang, C. Zhang, Y. Shoji, T. Mizumoto, and J. E. Bowers, "Microring-Based Optical Isolator and Circulator with Integrated Electromagnet for Silicon Photonics," *Journal of Lightwave Technology* **35**(8), pp. 1429–1437, 2017. (Cited on page 89.)

[126] J. S. Foresi, P. R. Villeneuve, J. Ferrera, E. R. Thoen, G. Steinmeyer, S. Fan, J. D. Joannopoulos, L. C. Kimerling, H. I. Smith, and E. P. Ippen, "Photonic-bandgap microcavities in optical waveguides," *Nature* **390**, pp. 143–145, nov 1997. (Cited on page 93.)

[127] A. J. Stepan, "Experimental setup for magneto-optical characterization of waveguides," Master's thesis, Technische Universität Hamburg-Harburg, 2011. (Cited on pages 98 and 99.)

[128] T. Pagel, S. Gade, M. Krause, H. Renner, and E. Brinkmeyer, "Phase and group birefringence of silicon waveguides," in *IEEE International Conference on Group IV Photonics GFP*, pp. 197–199, (Cardiff), 2008. (Cited on page 98.)

[129] D. Jalas, A. Stepan, A. Y. Petrov, and M. Eich, "Experimental demonstration of magneto-optical phase shift in silicon on insulator waveguides," in *IEEE International Conference on Group IV Photonics GFP*, pp. 160–162, 2011. (Cited on page 99.)

[130] A. B. Fallahkhair, K. S. Li, and T. E. Murphy, "Vector Finite Difference Modesolver for Anisotropic Dielectric Waveguides," *Journal of Lightwave Technology* **26**(11), pp. 1423–1431, 2008. (Cited on page 100.)

[131] D. C. Meeker, "Finite Element Method Magnetics." (Cited on pages 100 and 101.)

[132] H. Piller and R. F. Potter, "Faraday Rotation Near the Band Edge of Silicon," *Physical Review Letters* **9**, pp. 203–205, sep 1962. (Cited on pages 103 and 118.)

[133] J. Noda, T. Hosaka, Y. Sasaki, and R. Ulrich, "Dispersion of Verdet constant in stress-birefringent silica fibre," *Electronics Letters* **20**(22), pp. 906–908(2), 1984. (Cited on page 103.)

[134] M. Bloemen, "Synthesis and characterization of hybrid organic-inorganic superparamagnetic nanoparticles," Master's thesis, Katholieke Universiteit Leuven, 2010. (Cited on page 105.)

[135] K. Shinagawa, "Faraday and Kerr Effects in Ferromagnets," in *Magneto-Optics*, S. Sugano and N. Kojima, eds., pp. 137–177, Springer Berlin Heidelberg, Berlin, Heidelberg, 2000. (Cited on page 105.)

[136] Y. Hou, J. Yu, and S. Gao, "Solvothermal reduction synthesis and characterization of superparamagnetic magnetite nanoparticles," *Journal of Materials Chemistry* **13**(8), pp. 1983–1987, 2003. (Cited on page 107.)

[137] C. R. Lin, Y. M. Chu, and S. C. Wang, "Magnetic properties of magnetite nanoparticles prepared by mechanochemical reaction," *Materials Letters* **60**, pp. 447–450, feb 2006.

[138] S. Aliramaji, A. Zamanian, and Z. Sohrabijam, "Characterization and Synthesis of Magnetite Nanoparticles by Innovative Sonochemical Method," *Procedia Materials Science* **11**, pp. 265–269, jan 2015. (Cited on page 107.)

[139] J. C. Schmoeckel, "Laserablation magnetooptischaktiver YIG-Schichten auf Silizium," Bachelor's thesis, Universität Augsburg, 2013. (Cited on pages 109 and 111.)

[140] L. Bi, J. Hu, L. Kimerling, and C. A. Ross, "Fabrication and characterization of As2S3/Y3Fe5O12 and Y3Fe5O12/SOI strip-loaded waveguides for integrated optical isolator applications," **7604**, pp. 760406–760410, 2010. (Cited on page 109.)

[141] W. Bogaerts, P. De Heyn, T. Van Vaerenbergh, K. De Vos, S. Kumar Selvaraja, T. Claes, P. Dumon, P. Bienstman, D. Van Thourhout, and R. Baets, "Silicon microring resonators," *Laser & Photonics Reviews* **6**, pp. 47–73, jan 2012. (Cited on page 111.)

[142] X. Y. Sun, Q. Du, T. Goto, M. C. Onbasli, D. H. Kim, N. M. Aimon, J. Hu, and C. A. Ross, "Single-Step Deposition of Cerium-Substituted Yttrium Iron Garnet for Monolithic On-Chip Optical Isolation," *ACS Photonics* **2**, pp. 856–863, jul 2015. (Cited on pages 113, 115, and 132.)

[143] D. L. Wood, "Optical Spectra of Rare-Earth Orthoferrites," *Journal of Applied Physics* **41**(13), p. 5315, 1970. (Cited on page 118.)

[144] W. J. Tabor, "Visible and Infrared Faraday Rotation and Birefringence of Single-Crystal Rare-Earth Orthoferrites," *Journal of Applied Physics* **41**(7), p. 3018, 1970. (Cited on page 118.)

[145] R. Soref and B. Bennett, "Electrooptical effects in silicon," *IEEE Journal of Quantum Electronics* **23**(1), pp. 123–129, 1987. (Cited on page 118.)

[146] G. Li, J. Yao, H. Thacker, A. Mekis, X. Zheng, I. Shubin, Y. Luo, J.-h. Lee, K. Raj, J. E. Cunningham, and A. V. Krishnamoorthy, "Ultralow-loss, high-density SOI optical waveguide routing for macrochip interconnects," *Optics Express* **20**(11), pp. 12035–12039, 2012. (Cited on page 119.)

[147] M. Cherchi, S. Ylinen, M. Harjanne, M. Kapulainen, T. Vehmas, and T. Aalto, "Low-loss spiral waveguides with ultra-small footprint on a micron scale SOI platform," in *Proceedings of SPIE*, **8990**, pp. 899005–899007, 2014. (Cited on page 119.)

[148] M. Cherchi, S. Ylinen, M. Harjanne, M. Kapulainen, and T. Aalto, "Dramatic size reduction of waveguide bends on a micron-scale silicon photonic platform," *Optics Express* **21**(15), pp. 17814–17823, 2013. (Cited on pages 122, 123, and 131.)

[149] M. Cherchi, S. Ylinen, M. Harjanne, M. Kapulainen, T. Vehmas, and T. Aalto, "The Euler bend: paving the way for high-density integration on micron-scale semiconductor platforms," in *Proceedings of SPIE*, **8990**, pp. 899004–899007, 2014. (Cited on page 131.)

[150] M. Cherchi, M. Harjanne, S. Ylinen, K. Vyrsokinos, M. Kapulainen, T. Vehmas, and T. Aalto, "Compact low-loss delay

lines on a micron-scale SOI platform," in *Group IV Photonics (GFP), 2014 IEEE 11th International Conference on*, pp. 81–82, 2014. (Cited on page 122.)

[151] S. Ghosh, S. Keyvaninia, Y. Shoji, W. Van Roy, T. Mizumoto, G. Roelkens, and R. G. Baets, "Compact Mach-Zehnder Interferometer Ce: YIG/SOI Optical Isolators," *Photonics Technology Letters, IEEE* **24**(18), pp. 1653–1656, 2012. (Cited on page 124.)

[152] S. Ghosh, S. Keyvavinia, W. Van Roy, T. Mizumoto, G. Roelkens, and R. Baets, "Ce:YIG/Silicon-on-Insulator waveguide optical isolator realized by adhesive bonding," *Optics Express* **20**(2), pp. 1839–1848, 2012. (Cited on page 124.)

[153] G. Cocorullo and I. Rendina, "Thermo-optical modulation at 1.5 μm in silicon etalon," *Electronics Letters* **28**(1), pp. 83–85, 1992. (Cited on page 126.)

[154] R. L. Espinola, M. C. Tsai, J. T. Yardley, and R. M. Osgood Jr, "Fast and low-power thermooptic switch on thin silicon-on-insulator," *Photonics Technology Letters, IEEE* **15**(10), pp. 1366–1368, 2003. (Cited on page 126.)

[155] Y. Kokubun, S. Yoneda, and H. Tanaka, "Temperature-independent narrowband optical filter at 1.3 μm wavelength by an athermal waveguide," *Electronics Letters* **32**(21), pp. 1998–2000, 1996. (Cited on page 126.)

[156] Y. Okada and Y. Tokumaru, "Precise determination of lattice parameter and thermal expansion coefficient of silicon between 300 and 1500 K," *Journal of Applied Physics* **56**, pp. 314–320, jul 1984. (Cited on page 126.)

[157] P. Hess, "Laser diagnostics of mechanical and elastic properties of silicon and carbon films," *Applied Surface Science* **106**, pp. 429–437, oct 1996. (Cited on page 126.)

[158] M. Huang, "Stress effects on the performance of optical waveguides," *International Journal of Solids and Structures* **40**, pp. 1615–1632, apr 2003. (Cited on page 126.)

[159] C. Zhang, P. Dulal, B. J. H. Stadler, and D. C. Hutchings, "Monolithically-Integrated TE-mode 1D Silicon-on-Insulator Isolators using Seedlayer-Free Garnet," *Scientific Reports* **7**(1), p. 5820, 2017. (Cited on pages 132 and 135.)

[160] T. Goto, D. H. Kim, X. Sun, M. C. Onbasli, J. M. Florez, S. P. Ong, P. Vargas, K. Ackland, P. Stamenov, N. M. Aimon, M. Inoue, H. L. Tuller, G. F. Dionne, J. M. D. Coey, and C. A. Ross,

"Magnetism and Faraday Rotation in Oxygen-Deficient Polycrystalline and Single-Crystal Iron-Substituted Strontium Titanate," *Physical Review Applied* **7**, p. 24006, feb 2017. (Cited on page 132.)

[161] Q. Du, C. Wang, Y. Zhang, Y. Zhang, T. Fakhrul, W. Zhang, C. Gonçalves, C. Blanco, K. Richardson, L. Deng, C. A. Ross, L. Bi, and J. Hu, "Monolithic On-chip Magneto-optical Isolator with 3 dB Insertion Loss and 40 dB Isolation Ratio," *ACS Photonics* **5**, pp. 5010–5016, dec 2018. (Cited on page 132.)

[162] D. L. Sounas and A. Alù, "Non-reciprocal photonics based on time modulation," *Nature Photonics* **11**(12), pp. 774–783, 2017. (Cited on page 132.)

[163] J. Kim, S. Kim, and G. Bahl, "Complete linear optical isolation at the microscale with ultralow loss," *Scientific Reports* **7**(1), p. 1647, 2017. (Cited on page 133.)

[164] D. B. Sohn, S. Kim, and G. Bahl, "GHz-Bandwidth Optical Isolation Through Acoustic Pumping of a Nanophotonic Circuit," in *2018 IEEE Photonics Conference (IPC)*, pp. 1–2, 2018.

[165] N. Dostart, Y. Ehrlichman, C. Gentry, and M. Popovic, "Energy-efficient active integrated photonic isolators using electrically driven acoustic waves," *arXiv preprint* **arXiv:1811**, oct 2018.

[166] E. A. Kittlaus, N. T. Otterstrom, P. Kharel, S. Gertler, and P. T. Rakich, "Non-reciprocal interband Brillouin modulation," *Nature Photonics* **12**(10), pp. 613–619, 2018. (Cited on page 133.)

[167] Z. Yu and S. Fan, "Optical isolation based on nonreciprocal phase shift induced by interband photonic transitions," *Applied Physics Letters* **94**, p. 171116, apr 2009. (Cited on page 133.)

[168] N. A. Estep, D. L. Sounas, and A. Alù, "Magnetless Microwave Circulators Based on Spatiotemporally Modulated Rings of Coupled Resonators," *IEEE Transactions on Microwave Theory and Techniques* **64**(2), pp. 502–518, 2016. (Cited on page 133.)

[169] N. A. Estep, D. L. Sounas, J. Soric, and A. Alù, "Magnetic-free non-reciprocity and isolation based on parametrically modulated coupled-resonator loops," *Nature Physics* **10**, p. 923, nov 2014. (Cited on page 133.)

[170] R. Fleury, D. L. Sounas, and A. Alù, "Subwavelength ultrasonic circulator based on spatiotemporal modulation," *Physical Review B* **91**, p. 174306, may 2015. (Cited on page 133.)

[171] M. Gaafar, D. Jalas, L. O'Faolain, J. Li, T. Krauss, A. Petrov, and M. Eich, "Reflection from a free carrier front via an intraband

indirect photonic transition," *Nature Communications* **9**(1), 2018. (Cited on page 133.)

[172] K. Y. Bliokh, F. J. Rodríguez-Fortuño, A. Y. Bekshaev, Y. S. Kivshar, and F. Nori, "Electric-current-induced unidirectional propagation of surface plasmon-polaritons," *Optics Letters* **43**(5), pp. 963–966, 2018. (Cited on page 133.)

[173] D. Jalas, N. Hakemi, M. Cherchi, M. Harjanne, A. Y. Petrov, and M. Eich, "Faraday rotation in silicon waveguides," in *14th International Conference on Group IV Photonics, GFP 2017*, pp. 141–142, 2017. (Cited on page 133.)

PUBLICATIONS

PATENT

- M. Cherchi, A. Petrov, D. Jalas, M. Harjanne, T. Aalto, M. Eich, "Integrated Faraday rotator," *PCT/FT2018/050595*, filing date August 22, 2018.

PUBLICATIONS ON NONRECIPROCAL PHOTONICS

- D. Jalas, A. Petrov, and M. Eich, "Optical three-port circulators made with ring resonators," *Optics Letters* **39**, pp. 1425–1428, 2014.
- D. Jalas, A. Petrov, M. Eich, W. Freude, S. Fan, Z. Yu, R. Baets, M. Popović, A. Melloni, J. D. Joannopoulos, M. Vanwolleghem, C. R. Doerr, and H. Renner, "What is – and what is not – an optical isolator," *Nature Photonics* **7**, pp. 579–582, 2013.
- S. Fan, R. Baets, A. Petrov, Z. Yu, J. D. Joannopoulos, W. Freude, A. Melloni, M. Popović, M. Vanwolleghem, D. Jalas, M. Eich, M. Krause, H. Renner, E. Brinkmeyer, C. R. Doerr, "Comment on "Nonreciprocal Light Propagation in a Silicon Photonic Circuit"," *Science*, **335**(6064), 38-38, 2012.
- D. Jalas, A. Petrov, M. Krause, J. Hampe, and M. Eich, "Resonance splitting in gyrotropic ring resonators," *Optics Letters* **35**, pp. 3438–3440, 2010.
- D. Jalas, A. Petrov, and M. Eich, "Theory of gyrotropic ring resonators with counterpropagating modes coupling," *Photonics and Nanostructures – Fundamentals and Applications* **9**(4), pp. 351–357, 2011.

CURRICULUM VITAE

EDUCATION

10/2008–09/2010	Hamburg University of Technology (TUHH), Hamburg M. Sc. in Elektrotechnik, Vertiefung Hochfrequenztechnik und Optik
10/2004–09/2008	Hamburg University of Technology (TUHH), Hamburg B. Sc. in Allgemeine Ingenieurswissenschaften, Vertiefung Elektrotechnik

WORK EXPERIENCE

since 09/2018	Dilax Intelcom GmbH, Berlin Sensor Developer
10/2010–06/2018	Hamburg University of Technology (TUHH), Hamburg Researcher

DANKSAGUNG

Die acht Jahre, in denen diese Arbeit entstanden ist, waren die erfülltesten in meinem bisherigen Leben. Die Gründe hierfür liegen natürlich nur zu einem kleinen Teil an meiner Arbeit am Institut OEM. Jedoch ist dieser Teil ein wichtiger und nicht zu vernachlässigen. Ich habe in dieser Zeit viel gelernt, sowohl über mich als auch über viele andere Dinge. Dafür möchte ich allen Beteiligten danken.

Ich möchte mich bei Prof. Dr. Manfred Eich dafür bedanken, mir die Möglichkeit gegeben zu haben, mich mit der nichtreziproken Photonik zu beschäftigen. Von seiner Art, Fragen und Probleme anzugehen, habe ich mir über die Jahre viel abgeschaut und denke, diese Dinge werden mich den Rest meines Lebens begleiten. Desweiteren möchte ich mich für die keinesfalls selbstverständliche Möglichkeit bedanken, mich in so viele andere Forschungsthemen im Institut einzubringen.

Ich möchte mich bei Dr. Alexander Petrov dafür bedanken, dass seine Tür über all die Jahre immer offen stand und man praktisch zu jeder Zeit vorbeikommen konnte, um den letzten spontanen Einfall zu diskutieren. Diese Möglichkeit vermisse ich schon jetzt. Gänzlich unermesslich waren für mich auch seine vielen Ideen, die meine Forschungsarbeit wesentlich bereichert haben.

Ich danke auch Prof. Dr. Arne Jacob, dass er sich dazu bereit erklärt hat, meine Dissertation zu begutachten. Seine Vorlesungen waren für mich die ersten in meinem Studium, die mich nicht bloß interessierten, sondern richtig begeisterten. Deswegen freut es mich, dass er nun auch das letzte Kapitel meiner akademischen Ausbildung begleitet hat.

Ich habe mich im Team OEM stets wohl gefühlt, daran hatten über die Jahre viele Kollegen einen wesentlichen Anteil. Ich bedanke mich für die schöne Zeit bei Lukas Maiwald, Matthias Graf, Manohar Chirumamilla, Gabi Birjukov, Hagen Renner, Hendrik Preuß, Guoliang Shang, Benjamin Echterhof, Iris Bucher, Stefan Schön, Michael Seiler, Etienne Blandre, Emily Shih-Ya Chen, Ali Erdem Eken, Wenjing Li, Zied Fahem, Lena Simone Fohrmann, Carolin Heintz, Sebastian Jakobs, Roman Kubrin, Slawa Lang, Clark Lee, Sean Molesky, Michel Castellanos Munoz, Toshiya Okuma, Ricardo Starbird Perez und Stefan Prorok. Ganz besonders möchte ich meinen Büronachbarn für die immer angenehme Gesellschaft danken: Jan Hampe, Pavel Dyachenko, Mahmoud Gaafar und Marvin Schulz.

Der andere große Grund, warum ich in meiner Doktorandenzeit so zufrieden war, sind meine Freunde und Familie. Stephan, danke für die vielen langen Barabende mit gemütlichen, aber auch mal hitzigen Diskussionen. Mama, Sören, Tim und Anna, danke, dass ihr immer da seid.

Zu guter letzt möchte ich bei meinem Vater danken, dass er mein Interesse an den Naturwissenschaften geweckt hat. Dieses war, ist und wird für mich immer Quell großer Freude sein und wird mich auf ewig mit ihm verbinden.